

Experimental Study of Burner Geometry Effect on the Coherent  
Structures, Flashback, and Flame Front Dynamics of Unconfined and  
Confined Partially Premixed Swirling Methane Flames

By

Mahmoud M.A. Ahmed

A Thesis submitted to the Faculty of Graduate Studies of  
The University of Manitoba  
in partial fulfillment of the requirements of the degree of

Doctor of Philosophy

Department of Mechanical Engineering  
University of Manitoba  
Winnipeg

Copyright © 2020 by Mahmoud M.A. Ahmed

## **Abstract**

The effect of burner geometry (central fuel nozzle, mixing tube length, and flame confinement) on the ensuing flowfield's coherent structures (precessing vortex core and vortex shedding) and their relationship with some combustion stability parameters, such as flashback and flame front dynamics of a swirling partially premixed methane flame, is experimentally studied. In this investigation, several measurement techniques are employed. These include particle image velocimetry (PIV), Mie scattering, laser Doppler velocimetry (LDV), Bruel & Kjaer microphone, high-speed Schlieren imaging technique, and high-speed luminescence imaging. In addition, proper orthogonal decomposition (POD) is used as a post processing technique to capture the flow-field coherent structures. In the first part of the study, the effect of central nozzle geometry on coherent structures' strength and frequency is examined inside a relatively long mixing tube. Furthermore, the relationship between the strength and frequency of coherent structures and the mean flashback region inside the mixing tube is studied. In the second part, the central nozzle geometry is modified based on the conclusions reached in the first part of the study, and its effect on the suppression of the coherent structures is investigated using a relatively short mixing length. Finally, the effect of nozzle geometries, which exhibit the highest and lowest coherent structures' amplitude, on coherent structures and acoustics modes is studied using different mixing tube lengths in the presence of a flame confinement. The results showed that the central nozzle geometry significantly affects coherent structures' strength and amplitude inside the mixing tube. Moreover, the results revealed a strong relationship between coherent structures' strength and the mean flashback region inside the mixing tube. Furthermore, the central nozzle geometry is found to significantly affect the amplitude of coherent structures for both confined and unconfined swirling partial premixed flames, and acoustics for the confined flames. All in all, it can be

concluded that passive techniques can be a viable strategy for mitigating combustion instabilities of partially premixed flames.

## **Acknowledgements**

First, I express the deepest appreciation to my supervisor, Professor Madjid Birouk for his support and guidance. His patience and persistent help in overcoming several obstacles through my research led me to get better quality knowledge.

I would like to thank my examination committee members, Professor Ömer L. Gülder (University of Toronto), and Professors Vijay Chatoorgoon and Gabriel Thomas (University of Manitoba) for their invaluable feedback and suggestions that obviously improved the quality of the thesis.

I would like to express my gratitude and appreciation to Prof. Scott Ormiston for motivating me to carry on with my hard courses. I highly appreciate the assistance of my colleagues and coworkers in the Energy & Combustion Laboratory (ECL) for their great assistance, particularly Sviatoslaw Karnaoukh, Mohammadreza Farokhi, Abdullah Al-Qaisy, Ahmad Ayache, Trevor Mazak, and Cameron Verwey for their great support and ideas.

I sincerely acknowledge the financial support provided by Natural Sciences and Engineering Research Council (NSERC) and the University of Manitoba (GETS Program).

More importantly, I am gratefully indebted to my family for accepting nothing less than excellence for me. I am thankful for my parents for persistent love and support. I thank my brothers for their spiritual help.



## Table of Contents

<b>1. Chapter 1: Introduction</b> .....	1
<b>1.1. Introduction</b> .....	1
<b>1.2. Partially premixed flames (PPFs)</b> .....	2
<b>1.3. Progress and challenges of PPFs</b> .....	4
<b>1.4. Motivations and objectives</b> .....	10
<b>1.5. Outline of the thesis</b> .....	12
<b>1.6. References</b> .....	13
<b>2. Chapter 2: Effect of fuel Nozzle Geometry and Airflow Swirl on the Coherent Structures of Partially Premixed Methane Flame under Flashback Conditions</b> .....	23
<b>2.1. Abstract</b> .....	23
<b>2.2. Introduction</b> .....	24
<b>2.3. Experimental Setup and methodology</b> .....	27
<i>2.3.1. Burner and test conditions</i> .....	27
<i>2.3.2. Particle image velocimetry (PIV)</i> .....	29
<i>2.3.3. Schlieren technique</i> .....	32
<i>2.3.4. Proper orthogonal decomposition (POD)</i> .....	33
<i>2.3.5. Time-resolved imaging and Mie scattering</i> .....	34
<i>2.3.6. Laser Doppler velocimetry (LDV)</i> .....	34
<b>2.4. Results and discussion</b> .....	35
<i>2.4.1. Mean velocity and turbulence intensity</i> .....	36
<i>2.4.2. Frequency of the coherent structures and flame appearance</i> .....	39
<i>2.4.3. POD results</i> .....	43
<i>2.4.4. Phase averaging of the coherent structures</i> .....	44

2.4.5. Error analysis .....	48
<b>2.5. Conclusions</b> .....	50
<b>2.6. References</b> .....	51
<b>3. Chapter 3: Effect of Fuel Nozzle Geometry on a Swirling Partially Premixed Methane Flame</b>	<b>57</b>
<b>3.1. Abstract</b> .....	57
<b>3.2. Introduction</b> .....	58
<b>3.3. Experimental setup</b> .....	61
3.3.1. Burner configuration and test conditions. ....	61
3.3.2. Measuring techniques .....	63
<b>3.4. Results</b> .....	70
3.4.1. Mean flow characteristics .....	70
3.4.2. POD of the velocity field.....	76
3.4.3. Flame front dynamics .....	87
<b>3.5. Discussion</b> .....	91
<b>3.6. Conclusions</b> .....	93
<b>3.6. References</b> .....	97
<b>4. Chapter 4: Burner Geometry Effect on Coherent Structures and Acoustics of a Confined Swirling Partially Premixed Methane Flame</b> .....	<b>103</b>
<b>4.1. Abstract</b> .....	103
<b>4.2. Introduction</b> .....	104
<b>4.3. Experimental Setup and Methodology</b> .....	108
4.3.1. Burner configuration .....	108
4.3.2. Laser diagnostics .....	109
4.3.3. Acoustics and flame appearance measurements .....	111

4.3.4. <i>Error analysis</i> .....	114
<b>4.4. Results and Discussion</b> .....	115
4.4.1. <i>Mean velocity field characteristics</i> .....	116
4.4.2. <i>POD of velocity field</i> .....	124
4.4.3. <i>POD of flame front positions</i> .....	131
4.4.4. <i>Acoustics measurements</i> .....	136
<b>4.5. Conclusions</b> .....	137
<b>4.6. References</b> .....	139
<b>Chapter 5: Conclusions and Recommendations for Future Work</b> .....	145
<b>5.1. Research summary</b> .....	145
<b>5.2. Recommendations for future work</b> .....	148
<b>5.3. References</b> .....	150
<b>A. Appendix A: Error Analysis and Calibration</b> .....	152
<b>A.1. Uncertainty in the mean and rms velocity</b> .....	152
<b>A.2. Calibration</b> .....	154
<b>B. Appendix B: Laser Doppler Velocimetry (LDV)</b> .....	157
<b>C. Appendix C: Microphone Calibration</b> .....	162

## List of Tables

<b>Table 2.1.</b> Details of central nozzle geometry ( $D_c$ and $D_p$ are, respectively, the central and peripheral orifice diameter) .....	30
<b>Table 2.2.</b> Experimental test conditions .....	31
<b>Table 3.1.</b> Integral length scale in the mixing tube for the different central fuel nozzle geometries. ....	73
<b>Table 3.2.</b> Energy fraction of the summation of the first two modes in the mixing tube for the different central fuel nozzle geometries.....	78
<b>Table 3.3.</b> Energy fraction of the summation of the first four modes for the isothermal flow case (first row) and reacting flow case (second row) for different central fuel nozzle geometries. ....	80
<b>Table 4.1.</b> Experimental test conditions. ....	109
<b>Table 4.2.</b> Longitudinal integral length scale ( $\Lambda_L$ ) for different central nozzles and different mixing tube lengths.....	121
<b>Table B.1.</b> The selected parameters for the processor control. ....	161

## List of Figures

<b>Fig. 1.1.</b> Triple flame structure. ....	3
<b>Fig. 2.1.</b> Schematic diagram of the burner assembly, nozzle geometries, swirl generator, PIV laser sheet arrangement, and stability map (ROI#1 is indicated by the dashed red rectangle and ROI#2 by the dashed blue rectangle).....	31
<b>Fig. 2.2.</b> The procedure of image processing; (a) dewarped raw image (brightness is high to show the difference between flame front and seeding particles), (b) raw vector map, (c) extracted flame front area, and (d) the final vector map after extracting the flame front area.....	32
<b>Fig. 2.3.</b> Schematic diagram of the top view of Schlieren setup.....	33
<b>Fig. 2.4.</b> U-matrix .....	33
<b>Fig. 2.5.</b> Mean velocity contours at $S = 1.15$ and $Re = 12745$ for all nozzles, and at $S = 0.79$ and $Re = 30385$ for N7 (the rectangle in the central region indicates the mean flashback region).....	37
<b>Fig. 2.6.</b> Contours of axial turbulence intensity at $S = 1.15$ and $Re = 12745$ for all nozzles, and at $S = 0.79$ and $Re = 30385$ for N7 in the isothermal case.....	37
<b>Fig. 2.7.</b> Axial profiles of the normalized centerline axial (a) mean velocity, and (b-c) axial turbulence intensity.....	38
<b>Fig. 2.8.</b> (a) Illustration of the location where the axial velocity radial profiles upstream of the flashed back flame are measured, (b) radial profiles of the conditional mean axial velocity for different central nozzles at $S = 1.15$ and N7 at $S = 0.79$ , (c) instantaneous velocity contours of N7 at $S = 1.15$ , and (d) the corresponding extracted area of the instantaneous flashed back flame. ....	39
<b>Fig. 2.9.</b> (a) Eight successive Schlieren images with equal time spacing during one cycle of vortex shedding, (b) coherent structures' frequency of different central nozzles, where the bars represent the frequency extracted from Schlieren images and the circular markers represent the frequency peaks from LDV PSD, and (c,d) Schlieren images of the flame of N1 at high swirl number (left) and N7 at low swirl number (right) (the red arrows points to the position of the large eddies). ....	41

**Fig. 2.10.** (a) Contours of the mean progress variable “c”, (b) normalized power spectral density of the fluctuations of the flame length of N1 inside the mixing tube, (c) normalized power spectral density of the fluctuations of the flame width of N1 inside the mixing tube, (d) the mean flame length inside the mixing tube for each central nozzle, and (e) the mean flame width slightly below the mixing tube exit for each central nozzle ..... 42

**Fig. 2.11.** (a) POD modal energy of the first four modes and (b) POD modal energy of the summation of the first four modes for different central nozzles at different swirling airflow Reynolds number and swirl number ..... 44

**Fig. 2.12.** Vorticity fields of the phase averaging of the linear superposition of the first two POD modes along with streamlines for N7 at  $S = 0.79$  and  $Re = 30385$ , and N3 and N7 at  $S = 1.15$  and  $Re = 12745$  (note that  $X/D$  values on the vertical axes are different for each case). ..... 46

**Fig. 3.1.** Schematic diagram of (a) the burner setup with swirl generator, and (b) different central nozzle geometries (all dimensions in mm and all angles in deg). ..... 63

**Fig. 3.2.** Schematic of the experimental setup of PIV measurements in the (a) axial direction inside the mixing tube, and (b) radial direction downstream of the mixing tube exit. .... 65

**Fig. 3.3.** Procedure for obtaining the normalized flow density fields. .... 67

**Fig. 3.4.** Procedure of flame edge detection where (a) binarized image, (b) filtered image, (c) edge-detected image, and (d) extracted flame image. The squares in (c) and (d) are a magnification of typical voids of seeding particles. .... 70

**Fig. 3.5.** Normalized profiles of the centerline axial (a) mean velocity and (b) turbulence intensity of the isothermal flow, and (c) turbulence intensity of the reacting flow case for different central fuel nozzle geometries inside the mixing tube, and (d) the mean axial velocity vector field for N2 and N4 inside the mixing tube. .... 72

**Fig. 3.6.** Contours of the axial turbulence intensity in the mixing tube for different central nozzle geometries. .... 73

<b>Fig. 3.7.</b> Profiles of the normalized mean axial velocity for different nozzles of the (a) isothermal and (b) reacting flow cases, the corresponding axial profiles of the normalized axial RMS velocity of the (c) isothermal and (d) reacting flow cases, and contours of the mean flowfield for N3 of the (e) isothermal and (f) reacting flow. ....	76
<b>Fig. 3.8.</b> (a) POD modal energy of the first six modes for different nozzles inside the mixing tube (dashed black line indicates the threshold modal energy), and (b) POD modal energy of the summation of the first four modes for the different central fuel nozzle geometries inside the mixing tube.....	77
<b>Fig. 3.9.</b> Vorticity fields of the phase-averaged linear superposition of the first two POD modes at different phase angles in the mixing tube for N1.....	79
<b>Fig. 3.10.</b> POD modal energy of the first four modes for the different central fuel nozzle geometries in the (a) isothermal and (b) reacting flow cases, and (c) POD modal energy of the summation of the first four modes in the case of reacting flow for the different central fuel nozzle geometries.....	80
<b>Fig. 3.11.</b> Vorticity fields of the shapes of the first two POD modes of the isothermal flow case for N1 nozzle. ....	81
<b>Fig. 3.12.</b> Vorticity fields of the shapes of the first POD mode of the reacting flow case for the different central nozzle geometries.....	82
<b>Fig. 3.13.</b> Vorticity fields of the phase-averaged linear superposition of the first two POD modes for some phase angles of the reacting flow case for N2 and N3. ....	82
<b>Fig. 3.14.</b> (a) Time-averaged field of the azimuthal velocity ( $W$ ), and (b) the vorticity contours of the shape of the first POD mode of N4 in the isothermal (first row) and reacting flow (second row) cases.....	83
<b>Fig. 3.15.</b> PSD of the axial velocity fluctuations for (a) N2 in the case of isothermal flow, and (b) N2 and N4 in reacting flow case. ....	84
<b>Fig. 3.16.</b> Radial profiles of the phase-averaged radial and axial velocity at different phase angles in the reacting flow case for N1 and N3. ....	86

<b>Fig. 3.17.</b> Contours of (a) the normalized mean density fields, and (b) the normalized RMS velocity of N2 and N4.....	87
<b>Fig. 3.18.</b> (a) Axial profiles of the normalized mean flame front position, (b) contours of the mean progress variable, $c$ , for N4 (black area in the core region represents $c > 0.99$ ), and (c) variation of the mean progress variable, $c$ , as a function of the normalized radial distance ( $r/D$ ) at $X/D = 0.9$ for N1 and N4. ....	89
<b>Fig. 3.19.</b> Axial profiles of the phase angles of the (a) right and (b) the left wing of the flame front of instantaneous flame front positions for N2, and (c) mean phase difference between the right and left wings for N1 and N4 nozzles. ....	91
<b>Fig. 4.1.</b> PIV setup configuration and the ROI, and burner configuration including the swirl generator and central nozzles.....	111
<b>Fig. 4.2.</b> Schematic representation of the acoustics measurement configuration. ....	112
<b>Fig. 4.3.</b> (a) Flame edge detection procedure, and (b) illustration of HSV color space.....	114
<b>Fig. 4.4.</b> Typical streamlines of the mean velocity field of the (a) isothermal and (b) reacting cases, and contours of the axial mean velocity of (c) isothermal and (d) reacting cases (the black solid line represents $V = 0$ ) for different central nozzle geometries and different mixing tube lengths.....	118
<b>Fig. 4.5.</b> Profiles of the centerline axial mean velocity of (a) reacting and (b) isothermal cases, the absolute normalized centerline axial rms velocity of (c) reacting and (d) isothermal cases, and (e) rms of the CRZ width of the reacting flow cases for different central nozzles at different mixing tube lengths. ....	120
<b>Fig. 4.6.</b> Contours of the axial turbulence intensity for the different central nozzle geometries and different mixing tube lengths in reacting flow cases. ....	121
<b>Fig. 4.7.</b> Contours of the axial turbulence intensity inside the mixing tube for different central nozzles and different mixing tube lengths. ....	122
<b>Fig. 4.8.</b> (a) Axial profiles of the centerline strain rate of the mean flowfields for different central nozzles and different mixing tube lengths, and (b) typical instantaneous contour of strain rate for N1S. ....	123



**Fig. 4.9.** (a) Typical large ROI and cropped ROI for an isothermal flow case with the first POD mode, POD modal energy of the summation of the first six modes for (b) isothermal and (c) reacting cases, (d) POD modal energy of the first four modes for different central nozzles and different mixing tube lengths, and (e) scatter plot of the normalized time coefficients of the first two POD modes with phase angle ( $\varphi$ ). ..... 126

**Fig. 4.10.** (a) Representation of the shapes of the first four POD modes with the corresponding modal energy fraction for N1S (red circles represents the large turbulent structures), and (b) PSD of the axial velocity fluctuations, which shows the coherent structures' frequency, for different central nozzles and different mixing tube lengths. .... 128

**Fig. 4.11.** Vorticity fields of the phase averaged linear superposition of the reconstructed first two POD modes for different central nozzles and different mixing tube lengths. .... 129

**Fig. 4.12.** Variation of the radial profiles of phase-averaged axial and radial velocity with phase angle at  $X/D = 0.45$  for N1L and N2L (red arrow represents the phase angles from  $45^\circ$  to  $180^\circ$  and blue arrow represents the phase angles from  $225^\circ$  to  $360^\circ$ ). .... 130

**Fig. 4.13.** (a) Flame luminescence images, and (b) contours of the mean progress variable,  $c$ , of the flame front positions for different central nozzles and different mixing tube lengths. .... 132

**Fig. 4.14.** (a) POD modal energy of the first four modes of flame front positions, and (b) POD modal energy of the summation of the first two modes for different central nozzles and different mixing tube lengths. .... 133

**Fig. 4.15.** PSD of time coefficients of the first POD mode for different central nozzles and different mixing tube lengths. .... 133

**Fig. 4.16.** Phase-averaged flame front positions of the reconstructed linear superposition of the first two POD modes for different central nozzles and different mixing tube lengths. .... 136

**Fig. 4.17.** PSD of the acoustic signal for different central nozzles and different mixing tube lengths. .... 137

**Fig. A.1.** Student's t-distribution showing the rejection regions and the  $t_{critical}$ . .... 153

<b>Fig. A.2.</b> Chi-square distribution showing the rejection regions with the corresponding variables for $N = 7$ as an example.....	154
<b>Fig. A.3.</b> (a) Calibration board, and calibration procedure for both (b) unconfined and (c) confined flows. ....	156
<b>Fig. B.1.</b> LDV system including (a) the multicolor beam separator, (b) probe, (c) PDM, and (d) Doppler burst correlator. ....	158
<b>Fig. B.2.</b> The measurement volume with the formed fringes. ....	159
<b>Fig. B.3.</b> The photo detector module with the main components. ....	159
<b>Fig. B.4.</b> The optical parameters used in the present configuration.....	160
<b>Fig. B.5.</b> Typical LDV signal and filtering processes.....	161
<b>Fig. C.1.</b> Schematic of the internal structure of the sound calibrator type 4230 [1].....	162
<b>Fig. C.2.</b> Images of the microphone (first row) and the sound level calibrator (second row). ....	163

## List of Abbreviations

### Nomenclature

$A$	orifice cross-sectional area (mm <sup>2</sup> )
$A_c$	cross-sectional area of the central orifice (mm <sup>2</sup> )
$a_{i1}$	time coefficient of the first POD mode for snapshot ( $i$ )
$a_{i2}$	time coefficient of the second POD mode for snapshot ( $i$ )
$A_p$	cross-sectional area of a single peripheral hole (mm <sup>2</sup> )
$B$	bias error
$B_j$	bias error resulted from a source $j$
$C$	particle density distribution
$C_h$	homogeneous particle density distribution
$C_i$	percentage of the confidence interval
$c$	mean progress variable
$D$	inner diameter of the mixing tube (mm)
$d_o$	orifice diameter (mm)
$d_p$	seeding particle diameter (m)
$D_c$	diameter of the central orifice (mm)
$D_{cc}$	dark current of camera
$D_e$	equivalent diameter (mm)
$d_f$	fringe spacing (μm)
$D_o$	outer diameter of the mixing tube (mm)
$d_o$	diameter of each orifice in multi-orifice nozzles (mm)

$D_p$	diameter of a single peripheral orifice (mm)
$e$	total error
$e_{df}$	uncertainty of the fringe spacing
$e_{fD}$	uncertainty of the Doppler frequency
$ev$	uncertainty in instantaneous velocity in laser Doppler velocimetry
$f_1$	frequency of the first longitudinal mode (Hz)
$f_D$	Doppler frequency (Hz)
$f_{PVC}$	frequency of the precessing vortex core (PVC) (Hz)
$I$	intensity of the acquired instantaneous image in reacting flow case
$I_h$	intensity of the acquired homogeneous particle density image in cold flow
$I_l$	local light sheet intensity
$I_o$	intensity of the background image
$k$	specific heats ratio
$L$	mixing length
$L$	length of the confinement tube (m)
$l$	orifice length (mm)
$M$	total number of velocity vectors in each acquired PIV image
$N$	number of data samples
$n$	number of orifices or number of peripheral orifices
$n_{ref}$	refractive index
$N_{source}$	number of sources contributing to the bias error
$P$	precision error
$R$	gas constant (kJ/kg.K)

$R_q$	factor for reflections due to the use of quartz tube
$r$ or $r$	radial position (mm)
$Re_D$	Reynolds number based on the inner diameter of the mixing tube
$S$	strain rate
$S_{CL}$	centerline strain rate of the mean field
$S$	swirl number
$s$	axial position inside the mixing tube (mm)
$Sk$	Stokes number
$T$	temperature (K)
$t$	t values in the student's t-distribution
$t_{critical}$	critical t value in the student's t-distribution
$t_{cycle}$	time duration of one cycle of vortex shedding
$U$	radial velocity (m/s)
$\vec{u}$	reconstructed velocity field of the first two POD modes
$u_o$	velocity scale (m/s)
$V$	axial velocity (m/s)
$\bar{V}$	axial mean velocity (m/s)
$V_{CL}$	centerline axial mean velocity (m/s)
$V_j$	mean bulk flow velocity (m/s)
$V_{RMS}$	centerline axial rms velocity (m/s)
$v'$	root mean square (rms) of the axial velocity fluctuations (m/s)
$W$	azimuthal velocity (m/s)
$X$	axial position (mm)

$X^*_j$	Hilbert transform complex function
$x'_j$	flame front position fluctuation at certain axial position and certain frame
$X_m$	95% confidence interval for the mean velocity
$x_{mean}$	mean flame front positions
$X_{rms}$	95% confidence interval for the rms velocity
$x_{RMS}$	RMS of the flame front positions

### **Greek symbol**

$\alpha$	vane(s) angle of the swirl generator (°)
$\alpha_C$	significance level
$\beta_p$	angle of the peripheral orifices (°)
$\Delta\theta^{\circ}_{mean}$	mean phase difference between the left and right wings of the flame front (°)
$\delta$	flame brush thickness (mm)
$\varepsilon$	RMS error in estimating PIV velocity data (m/s)
$\theta^{\circ}$	phase angle of the flame front position (°)
$\theta^{\circ}_{right}$	phase angles of the right wing of the flame front (°)
$\theta^{\circ}_{left}$	phase angles of the left wing of the flame front (°)
$\kappa$	angle between two beams in the laser Doppler velocimetry (rad)
$\Lambda_L$	integral length scale (mm)
$\lambda_i$	POD modal energy of mode i
$\lambda_{th}$	threshold modal energy (m <sup>2</sup> /s <sup>2</sup> )
$\lambda_w$	wavelength of the laser (nm)

$\mu_F$	dynamic viscosity of the fluid (kg/m·s)
$\nu$	kinematic viscosity (m <sup>2</sup> /s)
$\rho$	fluid density (kg/m <sup>3</sup> )
$\rho_h$	homogeneous fluid density (kg/m <sup>3</sup> )
$\rho_P$	particle density (Kg/m <sup>3</sup> )
$\Sigma$	summation
$\tau_F$	integral time scale (s)
$\tau_P$	particle response time (s)
$\vec{\phi}$	POD mode shape
$\phi$	mixture/global equivalence ratio
$\varphi$	phase angle (°)
$\chi_{p1}^2$	chi-square distribution based on $p_1$ value
$\chi_{p2}^2$	chi-square distribution based on $p_2$ value
$\Omega$	normalized fluid density
$\omega$	vorticity (1/s)

### Acronym

BVK	Benard von Karman
CCD	charged coupled device
CFCN	concentric flow conical nozzle
CRZ	central recirculation zone
FOV	field of view

FTF	flame transfer function
HCCI	homogeneous charge compression ignition
HSV	hue, saturation, value color space
IMF	imaging model fit
IRZ	inner recirculation zone
ISL	inner shear layer
LED	light emitting diode
LDV	laser Doppler velocimetry
NO <sub>x</sub>	nitrogen oxides
ORZ	outer recirculation zone
OSL	outer shear layer
PDM	photo detector module
PIM	porous inert media
PIV	particle image velocimetry
PLIF	planar laser-induced fluorescence
POD	proper orthogonal decomposition
P.P.	partial premixing
PPCI	partially premixed compression ignition
PPFs	partially premixed flames
PSD	power spectral density (a.u.)
PVC	precessing vortex core
QLS	quantitative light sheet
RMS	root mean square



RGB	red, green, blue color space
ROI	region of interest in the image
RSS	root-sum-square
SNR	signal-to-noise ratio
TARS	triple annular research swirler

## **Declaration of the Academic Achievement**

The outline of this thesis follows “sandwich format” whose guidelines are appointed by the Faculty of Graduate Studies (FGS), University of Manitoba. It merges three individual papers prepared for publication in peer-reviewed journals. Chapter 1 contains an introduction about the problem statement and the thesis contributions; Chapters 2 to 4 are manuscripts containing an abstract, introduction, methods, results and discussion; Chapter 5 provides the conclusions of the work and recommendations for future research directions. Further information on the error analysis, laser Doppler velocimetry, and microphone calibration is presented in Appendices A, B, and C, respectively.

Chapters 2 and 3 are papers which have already been published, and Chapter 4 has been submitted for publication in a peer-reviewed journal and is still in the review process. The contribution of M.M.A. Ahmed consisted mainly of designing the experimental test rig, conducting the experiments, analyzing the data, plotting the figures, and writing manuscripts for conference presentations and journal publications. My supervisor (Professor Madjid Birouk) supervised the research and provided continuous feedback during the design of the test rig, data analysis, and manuscripts preparation/write-up.

## Copyright Notice

1. With permission from Elsevier:

M.M.A. Ahmed, M. Birouk, Effect of fuel Nozzle Geometry and Airflow Swirl on the Coherent Structures of Partially Premixed Methane Flame under Flashback Conditions, *Experimental Thermal and Fluid Science* 99 (2018) 304-314.

2. With permission from ASME:

M.M.A. Ahmed, M. Birouk, Effect of the Fuel Nozzle Geometry on a Swirling Partially Premixed Methane Flame, *Journal of Engineering for Gas Turbines and Power* 142 (3)(2020) 031009  
<https://doi.org/10.1115/1.4045477>.

3. With permission from Elsevier:

M.M.A. Ahmed, M. Birouk, Burner Geometry Effect on Coherent Structures and Acoustics of a Confined Swirling Partially Premixed Methane Flame, *Experimental Thermal and Fluid Science* 105 (2019) 85-99.

# Chapter 1: Introduction

## 1.1. Introduction

Fossil fuels were the main energy source for decades and still are the major source nowadays. However, the sources of fossil fuels are limited and they are the most important contributors of greenhouse gases and environmental pollution. To overcome this issue as well as to cope with the increase in energy demand/consumption, several technologies have been developed to harness energy from renewable sources such as wind, solar, nuclear and hydrodynamic energy. However, these renewable sources of energy still cannot completely substitute for all fossil fuels applications. For example, the vast majority of engineering power systems in industrial and transportation sectors still rely on fossil fuels. In order to utilize these renewable and conventional energy sources efficiently and environmentally friendly, novel combustion strategies should be developed. Enhancing combustion efficiency significantly decreases pollutant emissions. Flame stability, combustion efficiency, and pollutant emissions can all be dependent on fuel burning/combustion mode. For example, the relatively low temperature premixed combustion mode can result in a significant reduction in  $\text{NO}_x$  emissions. On the other hand, non-premixed combustion mode is more prone to the formation of soot emissions. However, turbulent combustion, in general, is accompanied by flow instabilities that can arise under certain combustion modes/conditions.

Combustion can be classified into three categories; premixed, non-premixed (diffusion) and partially premixed. In premixed combustion, the fuel and air are completely mixed upstream of the reaction zone, while in non-premixed combustion, the fuel and air are found in either sides of the reaction zone. On the other hand, partially premixed combustion consists of inhomogeneous

combustible mixture since the fuel and air are not well mixed upstream of the reaction zone. It is well established that lean premixed combustion produces low  $\text{NO}_x$  emissions since flame temperature is low. However, this type of burning/flame is practically challenging due to safety considerations with regard to blowout, combustion instabilities, autoignition, and flashback [1]. Consequently, flame stability and pollutant emissions reduction should be considered when designing burners or combustion systems. Despite the fact that partially premixed flames can enhance flame stability and reduce pollutant emissions, most of published research focused on premixed and non-premixed flames. Therefore, further research is needed on developing methods to improve the stability of partially premixed flames.

## **1.2. Partially premixed flames (PPFs)**

PPFs are another alternative for premixed and diffusion flames. PPFs are used in numerous engineering combustion systems including gas turbines, industrial furnaces, domestic burners, internal combustion direct injection stratified charge engines, and partially premixed compression ignition (PPCI). Partially premixed flames (PPFs) consist of rich and lean pockets along the stoichiometric mixture fraction line. In fact, partly partially premixed combustion mode often co-exists with the diffusion mode such as flame kernels in diesel engine lifted diffusion flames. For instance, complete premixing in a premixed flame cannot always be achieved and, hence, some flame zones experience partially premixed burning. Moreover, in non-premixed flame, the fuel is most likely prone to be slightly mixed with air upstream of the reaction zone. In addition, partially premixed flames can evolve when non-premixed flames experience local quenching [2]. Also, lifted non-premixed flames experience partially premixed combustible mixture upstream of the flame zone [3]. The structure of PPFs is different than those of premixed and diffusion flames.

That is, PPFs consists of a leading edge that contains rich and lean premixed flame fronts followed by non-premixed flame [4]. That is, triple flame configuration is found to play a key role in the stabilization of partially premixed flames [5]. The presence of these reaction zones (Fig. 1.1) can sustain chemical reactions and, hence, enhance flame stability.

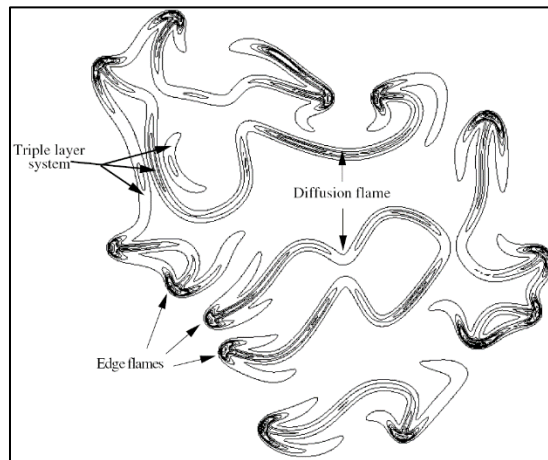


**Fig. 1.1.** Triple flame structure.

PPFs combine the advantage of diffusion flames (i.e., high flame stability) and that of premixed flames (i.e., low NO<sub>x</sub> and soot emissions). As previously mentioned, the presence of multiple reaction zones within these flames results in improved emission characteristics [6] and improved stability [7] compared to diffusion and premixed flames. It was found that if fuel-air mixture undergoes moderate partial premixing, it can result in enhancement of flame stability better than its premixed counterpart [4]. However, in contrast to non-premixed and premixed flames, describing PPFs requires more than a single conserved scalar which adds further complexity for PPFs modelling [8]. Operating combustion under lean fuel condition (e.g., PPFs) is an effective strategy to reduce NO<sub>x</sub> emissions. However, lean premixed flames are prone to instabilities such as flashback. For example, flames operating in this mode (leaner conditions) are

very sensitive to combustion oscillations. Moreover, inhomogeneity and unmixedness in PPFs can lead to thermoacoustic instabilities [9].

### **1.3. Progress and challenges of PPFs**

A variety of different methods reported in the literature were tested to improve the stability of PPFs, such as using a concentric flow conical nozzle (CFCN) burner [7, 8, 10-15], a concentric tube burner [16-18], a porous burner [19], a coflow [15, 20-21], a swirl generator [22-26], a bluff body [27-30], a counterflow [31-34], a slot burner [35, 36], and a pilot flame [37, 38]. The use of CFCN enhances flame stability by inducing flame expansion [10] and the formation of a reversal flow near the conical nozzle wall [7]. The use of a conical nozzle prevents quenching at the tip of flame by the cold ambient air. This is due to the fact that the entrained ambient air into the conical nozzle becomes hotter in the vicinity of a conical wall [14]. The cone angle was found one of the main parameters that affects mixture composition at the flame triple point and, hence, flame stability [11]. The mixing field in that configuration, which controls flame stability, is significantly affected by the mixing length and air-to-fuel velocities ratio [12]. Concentric tube burners are similar to CFCN without a conical nozzle downstream of the mixing tube exit, and flame stability and lift-off height are significantly affected by the partial premixing level [17]. Also, while kernel propagation speed of PPFs is significantly affected by fuel type at low Reynolds number; it is greatly affected by turbulence at high Reynolds number. Porous burners are rarely used with PPFs. However, employing a coflow results in improved flame stability within a range of optimum partial premixing level as compared to flames without a coflow [15]. In some burner configurations, a coflow leads to the formation of vortical structures downstream of the conical nozzle tip, which helps anchoring the flame at this location.

Swirl has recently been used with PPFs since it enhances turbulence intensity and mass and heat transfer, which, in turn, improves combustion and thermal efficiencies. Moreover, swirl anchors the flame aerodynamically without being in contact with any part of the burner. It was found that improvement of NO<sub>x</sub> emissions index and CO emissions of swirling PPFs can be achieved at an optimum partial premixing level [23]. Moreover, by investigating the reaction zone structures and mixing characteristics of swirling PPFs, it was found that PPFs can exhibit the characteristics of non-premixed flame more than those of premixed flame [39]. In order to overcome flame blowout in combustion applications such as aerospace propulsion engines, a bluff body has been used to stabilize the flame at high velocities. Slot burners were found to improve PPFs stability under a certain partial premixing level and a coflowing air velocity [36]. Meares and Masri [37] modified a jet piloted burner to enable the use of PPFs. They reported that, compared to the original piloted burner that does not operate with PPFs, varying the level of mixture inhomogeneity can alter local extinction behavior and improve flame stability.

The different studies reviewed above demonstrated that the level of inhomogeneity is a key parameter for the stabilization of PPFs. However, the aforementioned methods still have some shortcomings/drawbacks. For instance, in contrast to non-swirling flames, swirl tends to increase flashback propensity since turbulent flame speed becomes important [40]. Also, when using a bluff body in the flow direction, vortex shedding, as a coherent structure, becomes the main driver of combustion instabilities [41]. Combustion instability is found to be one of the main causes of flame flashback since the interaction between acoustic modes and heat release fluctuations can cause periodic flashback. Flashback can also cause overheating of the burner and could induce damage to the entire unit/engine [42]. Moreover, it was reported that flashback can increase pollutant emissions [43] for premixed flames.



Combustion instabilities can cause severe engine failure when the sound level become excessive [44]. Combustion instabilities are characterized by high amplitude of acoustic pressure oscillations within a combustion chamber which is driven by heat release rate fluctuations [45]. Additionally, heat release has a significant and proportional effect on acoustic oscillations particularly when pressure oscillations are in phase with heat release. However, if they are not in phase, heat release can reduce acoustic oscillations. This phenomenon is explained by Rayleigh criterion [46]. It should be noted that oscillations of both the equivalence ratio and flame surface area can directly cause heat release rate fluctuations [47] while pressure oscillations are induced by flow dynamics and the resonance of combustion chamber [48]. In addition, interactions between pressure oscillations and combustion dynamics can be more easily triggered under premixed or partially premixed flame conditions [49].

Acoustic modes significantly affect the flow field in some aspects. It was found that the main mechanism of sound generation is related to air entrainment into the reaction zone, where the classical combustion noise theory of perfectly premixed flames can still apply for PPFs [50]. That is, acoustic waves have the ability to modify the appearance of coherent structures within a combustor since they change the self-excited flow helical structures (PVC) to axisymmetric force coherent structures without involving external excitation [51]. Pressure oscillations can be generated by acoustic waves that cause oscillations in the equivalence ratio, which consequently induce heat release rate oscillations. It was found that, for PPFs, pressure fluctuations depend on the pressure of a combustor [52]. Furthermore, low-frequency instabilities can be reduced by increasing the turbulence intensity of unburned mixture, however, these instabilities increase  $\text{NO}_x$  emissions index [52]. Consequently, it is important to damp acoustic waves and suppress the equivalence ratio oscillations.

Combustion instabilities can be suppressed by either passive or active techniques [48]. Active techniques employed for the suppression of combustion instabilities is out of the scope of the present study, and therefore, the focus will be put on passive techniques. In fact, both techniques rely on preventing the coupling between heat release and acoustics. Passive techniques include the use of acoustic dampers [53], applying fuel staging and pilot flame [54], interrupting fuel-air ratio oscillations via wave cancellation concept [55], changing the fuel nozzle and burner geometry [56], and the use of baffles [57]. However, the use of passive techniques for suppressing combustion instabilities is quite costly and does not always work over an extended range of operating conditions. This problem can be severe if instabilities lie in the low frequencies range since passive techniques do not effectively mitigate combustion instabilities within that range. Employing short mixing lengths in PPFs was found as an alternative to premixed flames in order to mitigate combustion instabilities in some burner configurations [26]. However, short mixing can lead to an increase in  $\text{NO}_x$  emissions [26].

Understanding the nature of combustion instabilities is challenging since it is three-dimensional in nature and also time-dependent. For instance, the complex interaction between fluctuations of heat release, velocity, and pressure can produce combustion oscillations. Coherent structures (vortex shedding and precessing vortex core) can be a major source of periodic heat release [58]. The precessing vortex core (PVC), which is a helical instability, is formed in the flow when exceeding a critical swirl number. That is, the coupling between heat release oscillations and pressure fluctuations can be determined by the time delay between the formation of the coherent structure and energy release by combustion [59]. It is found that the coupling between combustion chamber acoustics, coherent structures, and heat release can lead to combustion instabilities [60]. Vortex shedding and PVC can modulate fuel-air mixing and cause fluctuations in fuel-air ratio. It

was found that upstream propagation (flashback) of a premixed flame tip is associated to the flame tip eccentricity, which is a direct result of PVC along the centerline at the burner exit [61]. In addition, vortex shedding is found to reappear prior to flame blowout [62] and can cause local extinction [63]. PVC most likely occurs on the central recirculation zone (CRZ) boundaries when, for example, a swirl number exceeds 0.6 [64]. The amplitude of PVC is proportional to swirl number [64], and can alter the shape of the central recirculation zone (CRZ) from an axisymmetric form to an asymmetric helical form [51]. Moreover, PVC can reappear after being suppressed under certain conditions, indicating that PVC can be suppressed under a limited range of operating conditions. However, changing the operating conditions can lead to a change in flame appearance/behaviour/dynamics [65], and this change was found responsible for suppression or excitation of PVC [66]. In other words, coherent structures have a significant influence on the flow field and flame dynamics.

Several published studies investigated the effect of coherent structures on the flow field of PPFs. Studying coherent structures and their effects on flame dynamics is important to mitigate thermoacoustic instabilities in a combustor. PVC was found responsible for enhancing fuel-air mixing downstream of the dump plane of a burner [67]. However, PVC can also induce combustion instabilities such as thermoacoustic instabilities [67]. Moreover, higher amplitude of PVC can increase volumetric discharge oscillations [68]. It was found that PVC depends on burner geometry, method of fuel injection, Reynolds number and swirl number [67]. In many cases, PVC behavior in reacting flows was found different than in isothermal flows, where PVC is often suppressed in reacting flow conditions [64]. PVC was found to contribute to flame stabilization and cause periodic changes in unburned gas composition [69]. It was reported that the location of the reaction zone was found to follow the path of PVC in the flow field, and there is a matching

between the location of auto-ignition and the center of PVC [70]. Moreover, it was reported that flame kernel, which is coupled to PVC, cannot always be attributed to auto-ignition in partially premixed flames [71]. Even small vortical structures were found to contribute to the destruction and formation of flame reaction zones [72]. In addition to enhancing mixing, PVC can also contribute to flame surface enlargement as a result of flame roll-up in a partially premixed flame regime [73]. The interaction between PVC and flame surface was found to significantly affect the location of heat release rate fluctuations [74]. Stöhr et al. [75] reported a newly observed large-scale OH structure in the crosswise direction, rather than the typical one associated with PVC, called spiral form. This spiral form was found to correlate well with the high rate of global heat release.

In contrast to isothermal flows, PVC can be suppressed in reacting flows due to higher viscosity and volume dilatation. However, combustor flow regimes do not always lead to PVC suppression. This is because suppression of PVC in reacting flows depends on many parameters, such as flame front radial location, the equivalence ratio, burner geometry, and the mode of fuel injection. Also, for premixed flames, PVC can alter the dynamics of flame roll-up within the outer shear layer by altering the receptivity of the shear layer to the acoustic waves. As previously mentioned, PVC can reappear after being suppressed in combustor flows at very low equivalence ratios. It was also found that the rate of fuel axial injection can lead to a change in the vortex breakdown shape, where a strong axial injection can convert the vortex breakdown from the bubble form to cone vortex breakdown form [76]. The occurrence of the cone type of vortex breakdown was found most likely responsible for PVC suppression [77]. Due to the complexity of the interaction between large scale coherent motions by PVC, chemical reaction and turbulence,

PVC mechanism is still not well understood. Additionally, the three-dimensional and time-dependence nature of PVC adds further difficulties to the understanding of its behavior.

The aforementioned discussion reveals why combustion instabilities are complex phenomena since they depend on the coupling between multi-physics and multi-scale parameters. Moreover, the different behaviors of coherent structures which significantly depend on the operating conditions (equivalence ratio, Reynolds number, or inlet temperature of air) and fuel composition (oxygen or hydrogen addition) make it difficult for coherent structures suppression over an extended range of operating conditions, especially when employing passive techniques. This complexity can be further increased when operating under PPFs regimes and varying partial premixing.

#### **1.4. Motivations and objectives**

Based on the above literature review, various passive methods were used to improve PPFs stability, such as swirl [24], coflow [15], CFCN burner [10], concentric tube burner [16], piloted burner [37], and bluff-body [27]. All the aforementioned techniques led to a different stabilization mechanism of PPFs as compared to those of premixed and diffusion flames (e.g., [10]). Swirling PPFs are essential for several combustion systems such as gas turbines. Nonetheless, swirl can intensify coherent structures such as vortex shedding and PVC in the absence or presence of bluff-body. Coherent structures can generate combustion instabilities which result in flashback. The effect of coherent structures on the flow and mixing fields is evident (e.g., [67]). Altering the geometry of a burner was found to be an important strategy for suppressing coherent structures and hence improving combustion stabilities [64]. The effect of burner geometry on flame stability and flow dynamics is reported in several studies [3, 70] for diffusion flames and [10, 37, 69] for

PPFs. For instance, using a concentric central recessed tube inside an outer mixing tube, where premixed fuel-air is discharged from the outer one and pure fuel from the central one, was found to eliminate coherent structures by varying the inhomogeneity level of the mixture [72]. It was revealed that the behavior of coherent structures (vortex shedding) downstream of a bluff-body and the blowout mechanism change significantly when the bluff-body has a slit [82]. It was also found that varying fuel nozzle geometry significantly affects turbulence intensity, decay, spread rate, mixing and entrainment of the flowfield of a diffusion flame [79]. However, varying nozzle geometry has not been yet tested for PPFs. Controlled mixing leads to enhanced flame stability and lower CO and NO<sub>x</sub> emissions. That is, an excess of mixing with cold air can lead to lower flame temperature and, hence, lower NO<sub>x</sub> emissions, but higher CO emissions [83]. Altering fuel injector/nozzle can smoothen rapid mixing that raises flame temperature, which results in a reduction in CO and NO<sub>x</sub> emissions [83]. Galley et al. [67] reported that when injecting the fuel axially from a central tube which is concentric with a mixing tube, mixing is not sufficient within a short distances. They, therefore, suggested the use of multi swirl generators due to their ability of inducing better mixing. However, improving mixing upstream of a flame can lead to an upstream flame propagation and hence flashback. Therefore, optimizing the mixing process is necessary for controlling downstream mixing while eliminating upstream flame propagation.

As discussed above, coherent structures can be detrimental to flame stability under certain combustion conditions. More importantly, axial fuel injection can be an alternative for coherent structures' suppression as a passive technique. Fuel nozzle geometry and axial fuel injection are expected to alter the unmixedness inside a concentric mixing tube. To the author's best knowledge, this strategy has not been yet studied in the case of PPFs. Thus, the objectives of this thesis are as follows:

- 1- Investigate the effect of burner geometry (fuel nozzle geometry and swirl number) on coherent structures (PVC and vortex shedding) inside and outside a relatively long mixing tube. The study aims to investigate the relationship between the upstream flame propagation (flashback) and coherent structures' strength and frequency of an unconfined swirling partially premixed methane flame.
- 2- Investigate the effect of burner geometry on PVC suppression, flame front dynamics, and acoustics using a relatively short mixing length of an unconfined swirling partially premixed methane flame. Additionally, other factors that contribute to promoting or suppressing PVC are also investigated.
- 3- Investigate the effect of coherent structures' strength and frequency, flame front dynamics, and acoustics of a confined swirling partially premixed methane flame.

The overall goal of the present study is to develop a passive technique (via altering burner geometry) which allows controlling coherent structures' amplitude and flashback propensity of PPFs. Specifically, the aim of the first and second investigations is to develop optimum geometries of nozzles for injecting fuel rich mixtures under a variety of test/operating conditions that mitigate flashback and coherent structures of unconfined PPFs used in, for example, industrial burners. The third investigation aims to develop an optimum burner configuration that mitigate coherent structures and acoustic oscillations of confined PPFs in systems such as gas turbine combustors.

### **1.5. Outline of the thesis**

The thesis consists of five chapters. The following chapter to this introduction reports an experimental investigation on the main parameters that controls flashback and coherent structures inside the mixing tube of a swirling unconfined partially premixed methane flame. In this study, the test conditions consisted of varying mainly the central nozzle through which a rich fuel-air

mixture is injected (where seven different central nozzle geometries were tested), and the swirl strength of the surrounding co-airflow (two swirl numbers were tested). Both, the co-airflow and rich mixture were discharged into a relatively long mixing tube which kept unchanged in this study. The main outcome of this study is to obtain the optimum nozzle geometry that promotes a reduction in the flashback propensity and/or the amplitude of coherent structures. Thereafter, the effect of the optimum nozzle geometry on PVC suppression, flame front dynamics, and acoustics of a swirling unconfined partially premixed methane flame is investigated in chapter 3. In this study, only four different central nozzle geometries, a relatively short mixing tube, and a single swirl strength were tested. Note that all measurements in this study are carried out under fixed operating conditions (i.e., similar global equivalence ratio, Reynolds number, and fuel and flow rates). In chapter 4, two of the four different central nozzles tested in chapter 3 are used along with two different mixing tube lengths to investigate their effect on coherent structures, flame front positions, and acoustics of a confined swirling partially premixed methane flame. The operation conditions (i.e., similar global equivalence ratio, Reynolds number, and fuel and flow rates) and swirl number are kept constant in this study. Finally, chapter five summarizes the major findings of this thesis and outlines some recommendations for future work. Additional details are provided in several appendices at the end of the thesis.

## **1.6. References**

- [1] T. Providakis, L. Zimmer, P. Scouflaire, and S. Ducruix, “Characterization of the coherent structures in swirling flames stabilized in a two-staged multi-injection burner : Influence of the staging factor,” *Comptes Rendus Mec.*, vol. 341, pp. 4–14, 2013.
- [2] V. Favier and L. Vervisch, “Edge flames and partially premixed combustion in diffusion



- flame quenching,” *Combust. Flame*, vol. 125, no. 1–2, pp. 788–803, 2001.
- [3] M. Saediamiri, M. Birouk, and J. a. Kozinski, “On the stability of a turbulent non-premixed biogas flame: Effect of low swirl strength,” *Combust. Flame*, vol. 161, pp. 1326–1336, 2014.
- [4] E. Baudoin *et al.*, “Effect of partial premixing on stabilization and local extinction of turbulent methane/air flames,” *Flow, Turbul. Combust.*, vol. 90, no. 2, pp. 269–284, 2013.
- [5] N. Peters, *Turbulent Combustion*. Cambridge: Cambridge University Press, 2000.
- [6] H. Xue and S. K. Aggarwal, “NO<sub>x</sub> emissions in n-heptane/air partially premixed flames,” *Combust. Flame*, vol. 132, pp. 723–741, 2003.
- [7] M. S. Mansour, A. M. Elbaz, and M. S. Samy, “The stabilization mechanism of highly stabilized partially premixed flames in a concentric flow conical nozzle burner,” *Exp. Therm. Fluid Sci.*, vol. 43, pp. 55–62, 2012.
- [8] M. S. Mansour, “A study of turbulent partially premixed flames based on simultaneous imaging of velocity field and OH radical,” *Combust. Sci. Technol.*, vol. 174, pp. 47–78, 2002.
- [9] S. Y. Lee, S. Seo, J. C. Broda, S. Pal, and R. J. Santoro, “An experimental estimation of mean reaction rate and flame structure during combustion instability in a lean premixed gas turbine combustor,” *Proc. Combust. Inst.*, vol. 28, no. 1, pp. 775–782, 2000.
- [10] M. S. Mansour, “A Concentric Flow Conical Nozzle Burner for Highly Stabilized Partially Premixed Flames,” *Combust. Sci. Technol.*, vol. 152, pp. 115–145, 2000.
- [11] A. M. Elbaz, “Early structure of LPG partially premixed conically stabilized flames,” *Exp. Therm. Fluid Sci.*, vol. 44, pp. 583–591, 2013.
- [12] M. S. Mansour *et al.*, “Effect of the mixing fields on the stability and structure of turbulent

- partially premixed flames in a concentric flow conical nozzle burner,” *Combust. Flame*, vol. 175, pp. 180–200, 2017.
- [13] B. Li *et al.*, “Experimental and numerical study of a conical turbulent partially premixed flame,” *Proc. Combust. Inst.*, vol. 32, pp. 1811–1818, 2009.
- [14] B. Yan *et al.*, “Structures and stabilization of low calorific value gas turbulent partially premixed flames in a conical burner,” *Exp. Therm. Fluid Sci.*, vol. 34, pp. 412–419, 2010.
- [15] A. M. Elbaz, M. F. Zayed, M. Samy, W. L. Roberts, and M. S. Mansour, “The flow field structure of highly stabilized partially premixed flames in a concentric flow conical nozzle burner with coflow,” *Exp. Therm. Fluid Sci.*, vol. 73, pp. 2–9, 2016.
- [16] M. S. Mansour, “The flow field structure at the base of lifted turbulent partially premixed jet flames,” *Exp. Therm. Fluid Sci.*, vol. 28, pp. 771–779, 2004.
- [17] T.-W. Lee, M. Fenton, and R. Shankland, “Effects of Variable Partial Premixing on Turbulent Jet Flame Structure,” *Combust. Flame*, vol. 109, pp. 536–548, 1997.
- [18] M. S. Mansour, A. M. Elbaz, and M. F. Zayed, “Flame Kernel Generation and Propagation in Turbulent Partially Premixed Hydrocarbon Jet,” *Combust. Sci. Technol.*, vol. 186, pp. 698–711, 2014.
- [19] A. A. Mohamad, M. Z. Abdullah, M. A. Mujeebu, and M. Z. A. Bakar, “The Development and Performance Analysis of Partially Premixed LPG Porous Medium Combustor,” *Energy Sources, Part A Recover. Util. Environ. Eff.*, vol. 33, pp. 1260–1270, 2011.
- [20] A. Lock, S. K. Aggarwal, and I. K. Puri, “Effect of fuel type on the extinction of fuel and air stream diluted partially premixed flames,” *Proc. Combust. Inst.*, vol. 32, pp. 2583–2590, 2009.
- [21] I. A. Mulla and S. R. Chakravarthy, “Propagation velocity and flame stretch measurements

- in co-flowing partially premixed flames with widely varying premixedness,” *Combust. Flame*, vol. 160, no. 8, pp. 1345–1356, 2013.
- [22] T. S. Cheng, C.-Y. Wu, Y.-H. Li, and Y.-C. Chao, “Chemiluminescence measurements of local equivalence ratio in a partially premixed flame,” *Combust. Sci. Technol.*, vol. 178, pp. 1821–1841, 2015.
- [23] T. S. Cheng, Y.-C. CHAO, D.-C. Wu, H.-W. Hsu, and T. Yuan, “Effects of Partial Premixing on Pollutant Emissions in Swirling Methane Jet Flames,” *Combust. Flame*, vol. 125, pp. 865–878, 2001.
- [24] A. E. Bayley, Y. Hardalupas, and A. M. K. P. Taylor, “Local curvature measurements of a lean, partially premixed swirl-stabilised flame,” *Exp. Fluids*, vol. 52, pp. 963–983, 2012.
- [25] K. P. Vanoverberghe, E. V. Ven den Bulck, M. J. Tummers, and W. A. Hubner, “Multiflame Patterns in Swirl-Driven Partially Premixed Natural Gas Combustor,” *J. Eng. Gas Turbines Power*, vol. 125, pp. 40–45, 2003.
- [26] S. Joo, J. Yoon, J. . Kim, M. Lee, and Y. Yoon, “NO<sub>x</sub> emissions characteristics of the partially premixed combustion of H<sub>2</sub>/CO/CH<sub>4</sub> syngas using artificial neural networks,” *Appl. Therm. Eng.*, vol. 80, pp. 436–444, 2015.
- [27] C. Karagiannaki *et al.*, “A comparison of the characteristics of disk stabilized lean propane flames operated under premixed or stratified inlet mixture conditions,” *Exp. Therm. Fluid Sci.*, vol. 59, pp. 264–274, 2014.
- [28] C. Xiouris and P. Koutmos, “An experimental investigation of the interaction of swirl flow with partially premixed disk stabilized propane flames,” *Exp. Therm. Fluid Sci.*, vol. 35, pp. 1055–1066, 2011.
- [29] V. R. Katta *et al.*, “Experimental and computational study on partially premixed flames in

- a centerbody burner,” *Combust. Flame*, vol. 158, pp. 511–524, 2011.
- [30] S. G. Tuttle *et al.*, “Lean blowoff behavior of asymmetrically-fueled bluff body-stabilized flames,” *Combust. Flame*, vol. 160, pp. 1677–1692, 2013.
- [31] P. Berta, S. K. Aggarwal, and I. K. Puri, “An experimental and numerical investigation of n-heptane/air counterflow partially premixed flames and emission of NO<sub>x</sub> and PAH species,” *Combust. Flame*, vol. 145, pp. 740–764, 2006.
- [32] T. Wada, M. Mizomoto, T. Yokomori, and N. Peters, “Extinction of methane/air counterflow partially premixed flames,” *Proc. Combust. Inst.*, vol. 32, pp. 1075–1082, 2009.
- [33] S. Naha and S. K. Aggarwal, “Fuel effects on NO<sub>x</sub> emissions in partially premixed flames,” *Combust. Flame*, vol. 139, pp. 90–105, 2004.
- [34] F. Carbone, F. Cattaneo, and A. Gomez, “Structure of incipiently sooting partially premixed ethylene counterflow flames,” *Combust. Flame*, vol. 162, no. 11, pp. 4138–4148, 2015.
- [35] I. A. Mulla and S. R. Chakravarthy, “Flame speed and tangential strain measurements in widely stratified partially premixed flames interacting with grid turbulence,” *Combust. Flame*, vol. 161, pp. 2406–2418, 2014.
- [36] M. S. Mansour *et al.*, “A concentric flow slot burner for stabilizing turbulent partially premixed inhomogeneous flames of gaseous fuels,” *Exp. Therm. Fluid Sci.*, vol. 91, pp. 214–229, 2018.
- [37] S. Meares and A. R. Masri, “A modified piloted burner for stabilizing turbulent flames of inhomogeneous mixtures,” *Combust. Flame*, vol. 161, no. 2, pp. 484–495, 2014.
- [38] R. S. Barlow, S. Meares, G. Magnotti, H. Cutcher, and A. R. Masri, “Local extinction and near-field structure in piloted turbulent CH<sub>4</sub> / air jet flames with inhomogeneous inlets,”

- Combust. Flame*, vol. 162, no. 10, pp. 3516–3540, 2015.
- [39] W. Meier, X. R. Duan, and P. Weigand, “Reaction zone structures and mixing characteristics of partially premixed swirling CH<sub>4</sub>/air flames in a gas turbine model combustor,” *Proc. Combust. Inst.*, vol. 30, pp. 835–842, 2005.
- [40] J. Fritz, M. Kröner, and T. Sattelmayer, “Flashback in a Swirl Burner With Cylindrical Premixing Zone,” *J. Eng. Gas Turbines Power*, vol. 126, no. 2, p. 276, 2004.
- [41] C. Fureby, “A computational study of combustion instabilities due to vortex shedding,” *Proc. Combust. Inst.*, vol. 28, no. 1, pp. 783–791, 2000.
- [42] N. Syred, M. Abdulsada, A. Griffiths, T. O’Doherty, and P. Bowen, “The effect of hydrogen containing fuel blends upon flashback in swirl burners,” *Appl. Energy*, vol. 89, no. 1, pp. 106–110, 2012.
- [43] B. Dam, G. Corona, M. Hayder, and A. Choudhuri, “Effects of syngas composition on combustion induced vortex breakdown (CIVB) flashback in a swirl stabilized combustor,” *Fuel*, vol. 90, no. 11, pp. 3274–3284, 2011.
- [44] P. G. M. Hoeijmakers, “PhD thesis,” Eindhoven university of technology, 2014.
- [45] M. Kröner, J. Fritz, and T. Sattelmayer, “Flashback Limits for Combustion,” *J. Eng. Gas Turbines Power*, vol. 125, no. 3, pp. 693–700, 2003.
- [46] L. Rayleigh, “The explanation of certain acoustical phenomena,” *Nature*, vol. 18, pp. 319–321, 1878.
- [47] T. Schuller, D. Durox, and S. Candel, “Dynamics of and noise radiated by a perturbed impinging premixed jet flame,” *Combust. Flame*, vol. 128, no. 1, pp. 88–110, 2002.
- [48] Y. Huang and V. Yang, “Dynamics and stability of lean-premixed swirl-stabilized combustion,” *Prog. Energy Combust. Sci.*, vol. 35, pp. 293–364, 2009.

- [49] A. Renaud, S. Ducruix, P. Scoufflaire, and L. Zimmer, "Flame shape transition in a swirl stabilised liquid fueled burner," *Proc. Combust. Inst.*, vol. 35, pp. 3365–3372, 2015.
- [50] P. Duchaine, L. Zimmer, and T. Schuller, "Experimental investigation of mechanisms of sound production by partially premixed flames," *Proc. Combust. Inst.*, vol. 32, pp. 1027–1034, 2009.
- [51] S. Terhaar, "PhD thesis," Technische Universität Berlin, 2015.
- [52] J. Kim, G. Choi, and D. Kim, "Effects of operating pressure on flame oscillation and emission characteristics in a partially premixed swirl combustor," *Exp. Therm. Fluid Sci.*, vol. 35, pp. 165–171, 2011.
- [53] J. Lepers, B. Prade, G. Pollarolo, W. Krebs, P. Flohr, and A. Ferrante, "Investigation of thermoacoustic stability limits of an annular gas turbine combustor test-rig with and without Helmholtz-resonators," *ASME Pap. 2005-GT-68246*, 2005.
- [54] R. C. Steele, L. H. Cowell, S. M. Cannon, and C. E. Smith, "Passive control of combustion instability in lean-premixed combustors," *J. Eng. Gas Turbines Power*, vol. 122, pp. 412–419, 2000.
- [55] T. Scarinci and J. L. Halpin, "Passive control of combustion instability in a low emissions aero-derivative gas turbine," *ASME Pap. 2004-GT-53767*.
- [56] C. O. Paschereit and E. Gutmark, "The effectiveness of passive combustion control methods," *ASME Pap. 2004-GT-53587*.
- [57] D. You, D. D. Ku, and V. Yang, "Acoustic Waves in Baffled Combustion Chamber with Radial and Circumferential Blades," *J. Propuls. Power*, vol. 29, no. 6, pp. 1453–1467, 2013.
- [58] K. C. Schadow and E. Gutmark, "Combustion instability related to vortex shedding in dump combustors and their passive control," *Prog. Energy Combust. Sci.*, vol. 18, pp. 117–132,

- 1991.
- [59] K. R. Mcmanus, T. Poinsot, and S. M. Candel, “A review of active control of combustion instabilities,” *Prog. Energy Combust. Sci.*, vol. 19, no. 1, pp. 1–29, 1993.
- [60] B. Tulsyan, K. Balasubramanian, and R. I. Sujith, “Revisiting a Model for Combustion Instability Involving Vortex Shedding,” *Combust. Sci. Technol.*, vol. 181, no. 3, pp. 457–482, 2009.
- [61] A. Schönborn, P. Sayad, and J. Klingmann, “Influence of precessing vortex core on flame flashback in swirling hydrogen flames,” *Int. J. Hydrogen Energy*, vol. 39, pp. 20233–20241, 2014.
- [62] J. R. Hertzberg, I. G. Shepherd, and L. Talbot, “Vortex shedding behind rod stabilized flames,” *Combust. Flame*, vol. 86, pp. 1–11, 1991.
- [63] S. Chaudhuri, S. Kostka, S. G. Tuttle, M. W. Renfro, and B. M. Cetegen, “Blowoff mechanism of two dimensional bluff-body stabilized turbulent premixed flames in a prototypical combustor,” *Combust. Flame*, vol. 158, no. 7, pp. 1358–1371, 2011.
- [64] N. Syred, “A review of oscillation mechanisms and the role of the precessing vortex core (PVC) in swirl combustion systems,” *Prog. Energy Combust. Sci.*, vol. 32, no. 2, pp. 93–161, 2006.
- [65] S. Terhaar, B. Cosic, C. O. Paschereit, and K. Oberleithner, “Suppression and excitation of the precessing vortex core by acoustic velocity fluctuations : An experimental and analytical study,” *Combust. Flame*, vol. 172, pp. 234–251, 2016.
- [66] S. Terhaar, K. Oberleithner, and C. O. Paschereit, “Impact of steam dilution on the flame shape and coherent structures in swirl-stabilized combustors,” *Combust. Sci. Technol.*, vol. 186, pp. 889–911, 2014.

- [67] D. Galley, S. Ducruix, F. Lacas, and D. Veynante, “Mixing and stabilization study of a partially premixed swirling flame using laser induced fluorescence,” *Combust. Flame*, vol. 158, no. 1, pp. 155–171, 2011.
- [68] R. Sadanandan, M. Stöhr, and W. Meier, “Flowfield-flame structure interactions in an oscillating swirl flame : An investigation using phase resolved and simultaneous OH-PLIF and stereoscopic PIV measurements,” *Combust. Explos. Shock Waves*, vol. 45, pp. 518–529, 2009.
- [69] M. Stöhr, C. M. Arndt, and W. Meier, “Transient effects of fuel–air mixing in a partially-premixed turbulent swirl flame,” *Proc. Combust. Inst.*, vol. 35, pp. 3327–3335, 2015.
- [70] I. Boxx, M. Stöhr, C. Carter, and W. Meier, “Temporally resolved planar measurements of transient phenomena in a partially pre-mixed swirl flame in a gas turbine model combustor,” *Combust. Flame*, vol. 157, pp. 1510–1525, 2010.
- [71] I. Boxx, C. D. Carter, M. Stöhr, and W. Meier, “Study of the mechanisms for flame stabilization in gas turbine model combustors using kHz laser diagnostics,” *Exp. Fluids*, vol. 54, pp. 1–17, 2013.
- [72] R. Sadanandan, M. Stöhr, and W. Meier, “Simultaneous OH-PLIF and PIV measurements in a gas turbine model combustor,” *Appl. Phys. B*, vol. 90, pp. 609–618, 2008.
- [73] M. Stöhr, R. Sadanandan, and W. Meier, “Phase-resolved characterization of vortex-flame interaction in a turbulent swirl flame,” *Exp. Fluids*, vol. 51, pp. 1153–1167, 2011.
- [74] A. M. Steinberg, I. Boxx, M. Stöhr, C. D. Carter, and W. Meier, “Flow-flame interactions causing acoustically coupled heat release fluctuations in a thermo-acoustically unstable gas turbine model combustor,” *Combust. Flame*, vol. 157, pp. 2250–2266, 2010.
- [75] M. Stöhr, R. Sadanandan, and W. Meier, “Experimental study of unsteady flame structures



- of an oscillating swirl flame in a gas turbine model combustor,” *Proc. Combust. Inst.*, vol. 32, pp. 2925–2932, 2009.
- [76] P. Billant, J.-M. Chomaz, and P. Huerre, “Experimental study of vortex breakdown in swirling jets,” *J. Fluid Mech.*, vol. 376, pp. 183–219, 2016.
- [77] S. Terhaar, T. G. Reichel, C. Schrodinger, L. Rukes, K. Oberleithner, and C. O. Paschereit, “Vortex Breakdown Types and Global Modes in Swirling Combustor Flows with Axial Injection,” *J. Propuls. power*, vol. 31, no. 1, pp. 219–229, 2015.
- [78] C. O. Iyogun and M. Birouk, “Effect of Fuel Nozzle Geometry on the Stability of a Turbulent Jet Methane Flame,” *Combust. Sci. Technol.*, vol. 180, no. 12, pp. 2186–2209, 2008.
- [79] C. O. Iyogun, M. Birouk, and J. a. Kozinski, “Experimental investigation of the effect of fuel nozzle geometry on the stability of a swirling non-premixed methane flame,” *Fuel*, vol. 90, no. 4, pp. 1416–1423, 2011.
- [80] V.-Z. Marco Osvaldo, S. Nicholas, V.-M. Agustín, and D. la R.-U. Daniel, “Flashback Avoidance in Swirling Flow Burners,” *Ing. Investig. y Tecnol.*, vol. 15, no. 4, pp. 603–614, 2014.
- [81] T. G. Reichel, S. Terhaar, and O. Paschereit, “Increasing Flashback Resistance in Lean Premixed Swirl-Stabilized Hydrogen Combustion by Axial Air Injection,” *J. Eng. Gas Turbines Power*, vol. 137, no. 7, pp. 71503–71509, Jul. 2015.
- [82] X. Liu, H. Zheng, J. Yang, and Y. Li, “LES-PDF modeling of blowout analysis in slit bluff-body stabilized flames,” *Int. J. Spray Combust. Dyn.*, vol. 7, no. 2, pp. 131–150, 2015.
- [83] T. S. Cheng *et al.*, “Effects of fuel-air mixing on flame structures and NO<sub>x</sub> emissions in swirling methane jet flames,” *Proc. Combust. Inst.*, vol. 27, no. 1, pp. 1229–1237, 1998.

## **Chapter 2: Effect of fuel Nozzle Geometry and Airflow Swirl on the Coherent Structures of Partially Premixed Methane Flame under Flashback Conditions**

### **2.1. Abstract**

The effect of fuel nozzle geometry and swirling airflow on the flashback and its relationship with the coherent structures of partially premixed methane flame is investigated experimentally. Particle image velocimetry (PIV) and laser Doppler velocimetry (LDV) are used to document flow characteristics, and Schlieren imaging technique is used to study flame appearance and vortex shedding frequency downstream of the burner exit. Proper orthogonal decomposition (POD) technique is applied to capture the coherent structures, along with phase averaging of the linear superposition of the first four POD modes. Seven different fuel nozzle geometries and two swirl number ( $S = 0.79$  and  $1.15$ ) are tested. The nozzles are categorized into three groups, with each has similar equivalent diameter; namely, a symmetric nozzle (used as a reference), nozzles with polygonal orifices (group A), and angled multi-orifice nozzles (group B). The results of the flow field inside the mixing tube show that the strength of coherent structures and flashback propensity increase with the swirling airflow Reynolds number, swirl number, nozzle bluff body area, and the number of the peripheral angled orifices of the fuel (central) nozzle. On the other hand, the results of flame appearance outside of the mixing tube indicate that methane flame experiences symmetric vortex shedding at high swirl number and low Reynolds number, while it experiences PVC near blowout conditions at low swirl number and high Reynolds number. Furthermore, the frequency of coherent structures is found to depend on the swirling airflow Reynolds number, swirl number, and fuel nozzle geometry. Additionally, the flashback's mean

region inside the mixing tube is found directly proportional to the strength and frequency of the coherent structures.

## **2.2. Introduction**

Partially premixed flames (PPFs) were used in several combustion applications such as internal combustion engines, gas turbines and industrial burners. For instance, the presence of lean and rich pockets along the stoichiometric mixture fraction line in a triple flame were reported to improve the PPFs stability compared to their counterparts' non-premixed and premixed flames [1-3]. Moreover, it was reported that emissions characteristics of PPFs can be comparable to those of premixed flames [4]. However, these flames require stabilization mechanisms, such as concentric flow conical nozzles (CFCN) [1-3], coflows [1], or pilot flames [5]. Other stabilization mechanisms, such as swirl and bluff body, were also adopted. Swirl was recently used with PPFs [6] since it enhances mass and heat transfer which in turn improves combustion and thermal efficiency [7]. However, the use of swirl may increase flashback propensity due to increased flame speed [8]. Furthermore, swirling flames are more prone to combustion instabilities as a result of the coupling between precessing vortex core (PVC) or vortex shedding and heat release [9]. Bluff body was used to stabilize flames at high flow velocities [10]. However, when using a bluff body in the direction of a flow, vortex shedding as coherent structures becomes the main driver of combustion instabilities. Furthermore, PPFs burners with a very short mixing length were used as an alternative to lean premixed flame to avoid combustion instabilities [11]. However, decreasing the mixing length may result in an increase in gas emissions [11]. Other studies reported that the optimum emissions characteristics and flame stability can be achieved using a longer mixing

length [3, 4]. However, the induced inhomogeneity and unmixedness of PPFs can generate thermoacoustic instabilities when using longer mixing lengths [12].

Flashback, as a consequence of combustion instabilities, can occur due to the interaction between acoustic modes and heat release fluctuations. Flashback can cause severe damage and overheating to burners and combustion chamber parts. In addition, flashback increases pollutant emissions [13] where a possible coupling may occur between acoustics and flashback [14]. Combustion instabilities are considered as a complex phenomenon since they are three-dimensional and time-dependent in nature. It was found that hydrodynamic instabilities, equivalence ratio fluctuations, flame surface variations, and oscillatory fuel atomization and vaporization are the main driving mechanisms of combustion instabilities [15].

Coherent structures, such as vortex shedding and PVC due to hydrodynamic instabilities, can be considered as a source of periodic heat release [15, 16]. Vortex shedding can cause wrinkling which can significantly contribute to flame surface variation [15] and, hence, cause heat release fluctuations. Heat release fluctuations are considered as a major source of acoustics motion in a combustion chamber [15]. Acoustic modes can modulate fuel/air mass flow rate leading to equivalence ratio fluctuations and consequently cause combustion instabilities [15]. Coherent structures and their influence on flame blowout and flashback have recently been the subject of several studies (e.g., [17]). It was found that the coupling between combustion chamber acoustics, coherent structures and heat release can cause combustion instabilities. Several studies investigated flame stability and blowoff mechanism of axisymmetric bluff body burners [18-21]. Unlike the 2D slender bluff body which shows BVK street, axisymmetric bluff body exhibits helical or symmetric modes of vortex shedding. Conversion from symmetric to helical mode was

found to occur at high Reynolds number [22]. Furthermore, depending on the flow conditions, the same burner configuration can exhibit either vortex shedding or PVC.

Controlled mixing should enhance flame stability and lower  $\text{NO}_x$  emissions. Combustor and burner geometries play a key role in the stability of combustion since it significantly affect flame structure and acoustics [15, 23]. Injecting the fuel through a central orifice of a bluff body was adopted in several studies with the aim to enhance mixing in the wake region [18, 24]. Implementing a recession for an axisymmetric bluff body inside a confinement with an optimum inner diameter was found to significantly enhance flame stability [18]. For instance, using a concentric central recessed tube inside an outer tube to discharge premixed fuel-air was found to eliminate coherent structures by promoting inhomogeneity of the mixture [17, 25]. For example, Galley et al. [26] reported that, when injecting fuel axially from a central recessed tube, mixing was not sufficient over short distances. However, improving the mixing upstream of a flame may lead to upstream flame propagation [26]. Despite the importance of using central axial fuel injection to mitigate coherent structures and avoid flashback, increasing the momentum of the axial injection beyond a certain limit can increase the flashback propensity by enhancing macroscopic mixing [27]. In addition, central fuel injection may promote the flashback through wall boundary layer mechanism. Despite the fact that flashback propensity can be increased due to the presence of PVC or vortex shedding [28, 29], only a few published studies investigated the relationship between flashback and flow coherent structures.

Motivated by the aforementioned literature review, the present study aims to investigate the effects of the geometry of fuel orifice through an axisymmetric bluff body and swirling airflow strength on the upstream propagation of methane PPFs. The objective is to provide a passive technique for controlling the flashback by altering the coherent structures behavior inside the

mixing tube. To achieve the objective of this study, turbulent flow field upstream of the flame under flashback conditions is examined.

## **2.3. Experimental Setup and methodology**

### *2.3.1. Burner and test conditions*

The burner consists mainly of an interchangeable central nozzle and a co-axial annulus with a swirl generator, both discharging into a mixing tube, as schematically shown in Fig. 1. Two swirl generators with different vanes angle ( $50^\circ$  and  $60^\circ$ ) which correspond to a swirl number of 0.79 and 1.15, respectively, are tested. The swirl number is calculated based on the vanes angle (e.g., [26]). The mixing tube is made from fused silica with a length of 117 mm, which provides a mixing length of 111 mm, which is the distance between the tip of the central nozzle and the mixing tube exit. The mixing tube inner and outer diameters are 24 and 28 mm, respectively. It was found that further increase in the inner diameter of the mixing tube causes flame attachment to the central nozzle since the effect of the mixing tube's wall becomes weak. On the other hand, decreasing the inner diameter of the mixing tube was found to significantly reduce flame stability by increasing the mean bulk velocity at the same equivalence ratio. Seven central (fuel) nozzles with the same outer diameter ( $d_o = 12$  mm) and categorized into two groups and one reference nozzle are used. Table 2.1 provides a summary of these nozzles. A single-orifice nozzle (N1) is used as a reference. Group A includes a square nozzle (N2), an equilateral nozzle (N3), and a rectangular nozzle (N4) with aspect ratio of 2:1. The equivalent diameter of group A nozzles is assumed to be constant since it varies within  $\pm 5\%$ . Group B includes a four-orifice nozzle (N5), a six-orifice nozzle (N6), and a seven-orifice nozzle (N7). Their peripheral orifices are inclined by an angle  $\beta_p$  with respect to the centerline of the mixing tube. It should be mentioned that the bluff

solid area (solid area without orifices) of group B is higher than that of group A, with N1 has the highest. This allows to also study the effect of the central nozzle's bluff solid area. The equivalent diameter is determined as  $D_e = \sqrt{4A/\pi}$  where  $D_e$  is the diameter of a circle having a cross-sectional area, A, equivalent/similar to that of a non-circular orifice (rectangle, triangle or square) or a multi-orifice nozzle. Note that for a multi-orifice nozzle (group B),  $A = A_c + nA_p$ , where  $A_c$  is the area of the central orifice,  $A_p$  is the area of a single peripheral orifice, and n is the number of the peripheral orifices. The swirling airflow emerges from the annulus, which is a cylinder surrounding the central nozzle. The flow discharging from the central nozzle is a premixed air/methane and its mixing with swirling airflow starts right at the exit of the central nozzle. The central nozzle flowrate is kept constant (22 LPM and 4.6 LPM for air and 17.4 LPM for fuel) at both swirl numbers, and the swirling airflow rate at low and high swirl numbers are 535 and 215 LPM, respectively. These flow rates are selected such that the flame is maintained upstream of the mixing tube exit (in flashback conditions) but still not attached to the central nozzle. The equivalence ratio at low and high swirl number are 0.30 and 0.75, respectively. At low swirl number, the flame does not experience flashback before blowout, except with N7, and thus nozzles N1 through N6 are excluded from the experiments at this swirl number. Reynolds number ( $Re_D = DV_j/\nu$ ) is calculated based on the inner diameter of mixing tube (D) and the bulk flow mean velocity ( $V_j$ ), where  $\nu$  is the kinematic viscosity of the air-methane mixture. The inlet axial turbulence intensity is 0.31 and 0.3 at low and high Reynolds numbers, respectively. Test conditions are given in Table 2.2.





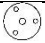
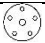

### 2.3.2. Particle image velocimetry (PIV)

Particle Image Velocimetry (PIV) was used to document the flow field inside the mixing tube. A schematic diagram of PIV arrangement is shown in Fig. 2.1. It consisted of a Nd:Yag laser with a maximum pulse energy of 135 mJ at 10 Hz, a double-frame FlowSence EO 4M CCD camera with a full resolution of  $2048 \times 2048$  pixel<sup>2</sup>, and DynamicStudio software. The physical size of the CCD sensor was  $15.2 \times 15.2$  mm<sup>2</sup>, and the f-number of the lens was adjusted at f/2.8 to limit the depth of field. A 45° protected silver 2-inch square mirror with an air cooling fan was placed 1 m above the quartz tube in order to project 1 mm thickness laser sheet through the quartz tube's centreline. The premixed flow from the central nozzle was seeded with incense particles with an average diameter of approximately 1 μm. Seeding only the flow from the central nozzle was found adequate since the measurements' field of view was located farther away from the central nozzle. This distance allowed both the central and swirling airflow to mix inside the mixing tube prior to reaching the PIV measurement region (ROI). Note that incense particles disappeared in the flame zone, and consequently an in-house developed Matlab code was used to remove velocity vectors in the flame zone from the velocity vector fields, as shown in Fig. 2.2. This makes it possible to qualitatively trace flame propagation into the mixing tube and examine the flashback's mean region. The flashback's mean region inside the mixing tube was determined by calculating the flashback's mean length inside the mixing tube and the flashback's mean width near the mixing tube exit. An in-house developed Matlab code was used to enhance the contrast between the flame zone and the seeding particles zone in order to extract the flame region from the image. The resultant extracted instantaneous flame images were then converted into binary images from which flame region was determined. Despite the fact that TiO<sub>2</sub> and olive oil seeding particles have the advantage of high thermal stability in a flame and close to its front, respectively, [30][31], they



were tested but not used here due to their accumulation onto the quartz tube wall and hence block optical access for flow visualization and PIV measurements. The maximum particles image size was found to be 3 pixels. A total of 1500 image pairs were captured for each test case, which were processed using an interrogation area of  $32 \times 32$  pixel<sup>2</sup> with 50% overlap, and spurious vectors were minimized using range validation. The instantaneous velocity vectors were then time-averaged and smoothed using  $3 \times 3$  vector moving average filter. A field of view (FOV) of  $21 \times 64$  mm<sup>2</sup> was selected to avoid laser reflection at the tip of the mixing tube and near-wall striations. This resulted in a pixel resolution of approximately 32  $\mu$ m. Dewarping image processing was needed since the physical position of seeding particles was shifted on the CCD as a result of the optical distortion due to the cylindrical shape of the quartz (mixing) tube. A calibration board was positioned at the laser sheet plane to create an imaging model fit (IMF) which was used for image dewarping in DynamicStudio software. Two regions of interest (ROI) were adopted; ROI#1 for N2 through N7 at high swirl number and ROI#2 for N7 at low swirl number and for N1 (Fig. 2.1). This is because of a longer flash back of flames of N7 at low swirl number and N1 which extend beyond ROI#1.

**Table 2.1.** Details of central nozzle geometry ( $D_c$  and  $D_p$  are, respectively, the central and peripheral orifice diameter)

Nozzle number	Nozzle geometry	$D_e$ (mm)	$D_c$ (mm)	$D_p$ (mm)	Aspect ratio	$\beta_p$ (°)
N1		2.1	2.1	-	-	-
N2		4.56	-	-	1:1	-
N3		4.46	-	-	-	-
N4		4.71	-	-	2:1	-
N5		3.75	2.87	1.4	-	30
N6		3.75	1.99	1.42	-	15
N7		3.75	1.42	1.42	-	15

**Table 2.2.** Experimental test conditions

No. of cases	Nozzle	Swirl number	Swirling airflow rate (LPM)	Central flow rate (LPM)	Global equivalence ratio ( $\phi$ )	Bulk flow mean velocity (m/s)	Reynolds number ( $Re_D$ )
1	N7	0.79	535	22	0.3	20.5	30385
7	N1 : N7	1.15	215		0.75	8.68	12745

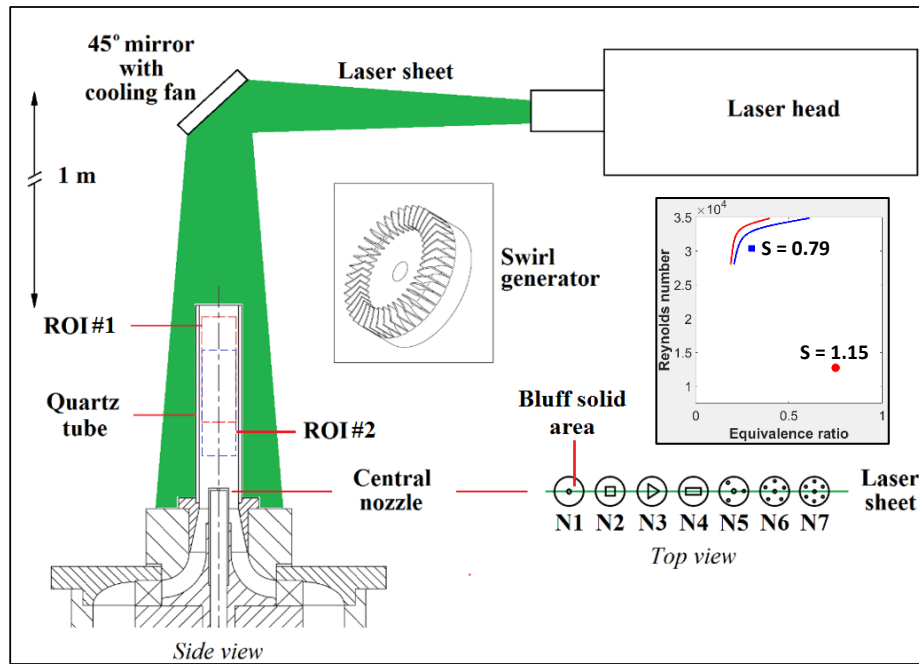


**Fig. 2.1.** Schematic diagram of the burner assembly, nozzle geometries, swirl generator, PIV laser sheet arrangement, and stability map (ROI#1 is indicated by the dashed red rectangle and ROI#2 by the dashed blue rectangle).

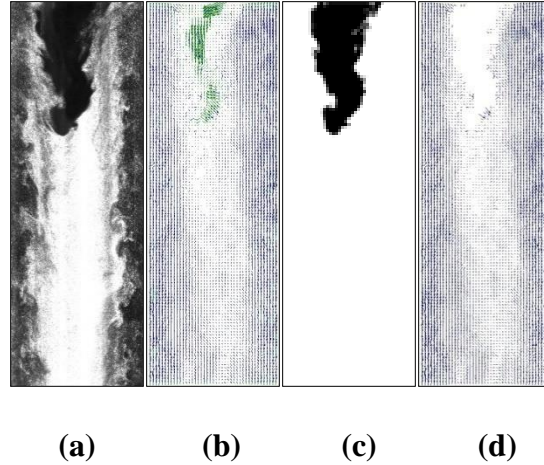


**Fig. 2.2.** The procedure of image processing; (a) dewarped raw image (brightness is high to show the difference between flame front and seeding particles), (b) raw vector map, (c) extracted flame front area, and (d) the final vector map after extracting the flame front area.

### 2.3.3. Schlieren technique

Schlieren imaging technique was used to capture time-resolved flame images at each test case (Fig. 2.3). The obtained images were used to determine the frequency of vortex shedding by observing the development of the large toroidal vortex shedding in the consecutive high-speed images. A z-type Schlieren setup was adopted which consisted of two identical parabolic concave mirrors, each has a focal length of 45" and a diameter of 4.5". A light source (LED) was aligned with the focal point of the concave mirror while a knife edge was placed at the focal point of the other mirror to enhance the sharpness of the flame edges. More details of the setup were reported elsewhere [32]. A total of 1200 images were captured for each test case using a Nikon 1 v2 high-speed camera having a resolution of 320×120 at 1200 Hz. The field of view was 132.5×94.5 mm<sup>2</sup>. Post processing of the captured images was performed to enhance the sharpness of the flame edge using an in-house developed Matlab code. The intensity of images was adjusted to increase the contrast, and then sharpened using unsharp filter to subtract the blurr from the original image with a strength of 1.2 and a standard deviation of the Gaussian lowpass filter of 3.

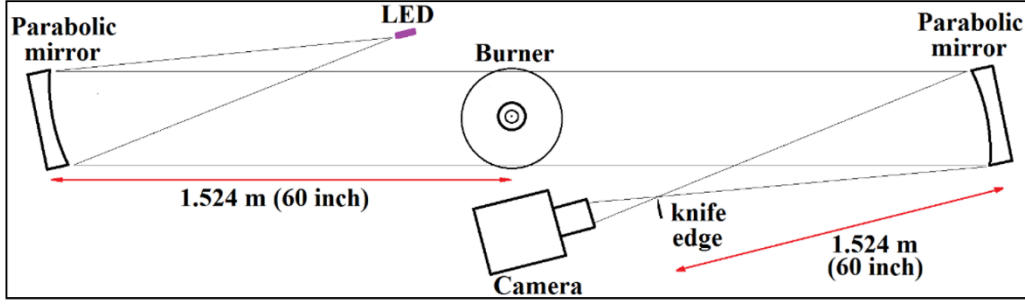


**Fig. 2.3.** Schematic diagram of the top view of Schlieren setup.

#### 2.3.4. Proper orthogonal decomposition (POD)

POD was used to capture the coherent structures inside the mixing tube using an in-house developed Matlab code. POD is considered as a powerful analysis tool for characterizing the flow coherent structures. The major advantage of POD is related to its linear procedure which consists of simple mathematical operations. Detailed procedure of the decomposition of the velocity fields is reported in Stöhr et al. [33]. The axial and radial components of the velocity fluctuations are obtained for each point and snapshot  $i$ . The calculated velocity fluctuations are arranged in a U-matrix with a size of  $M \times N$  such that each column represents snapshot  $i$  while each row represents the spatial variation (Fig. 2.4).

$$U = \begin{bmatrix} u_{11} & u_{12} & \vdots & u_{1N} \\ \vdots & \vdots & \vdots & \vdots \\ u_{M1} & u_{M2} & \vdots & u_{MN} \\ \hline v_{11} & v_{12} & \vdots & v_{1N} \\ \vdots & \vdots & \vdots & \vdots \\ v_{M1} & v_{M2} & \vdots & v_{MN} \end{bmatrix}$$

**Fig. 2.4.** U-matrix

The symmetric  $N \times N$  correlation of the U matrix is calculated from which the eigenvalues and eigenvectors of the correlation matrix are determined. The eigenvectors are sorted descending according to their mode energy (i.e., eigenvalues). The projection of each snapshot onto the POD

modes generates the flow field of each mode. The resultant POD flow fields of the linear superposition of the first mode pair are phase-averaged at each phase angle using the following relations [33]:

$$\varphi_i = \frac{1}{i} \ln \frac{a_{i1} + ia_{i2}}{\sqrt{a_{i1}^2 + a_{i2}^2}} \quad \text{and} \quad \vec{u}(\varphi) = \sqrt{2\lambda_1} \cos \varphi \vec{\phi}_1 + \sqrt{2\lambda_2} \sin \varphi \vec{\phi}_2$$

where  $\varphi_i$  is the phase angle at snapshot  $i$ ,  $a_{i1}$  and  $a_{i2}$  are the POD time coefficients of mode 1 and 2 at snapshot  $i$ , respectively.  $\lambda_1$  and  $\lambda_2$  are the mode energies of modes 1 and 2, respectively, and  $\vec{\phi}_1$  and  $\vec{\phi}_2$  are the flow fields of modes 1 and 2, respectively.

### 2.3.5. Time-resolved imaging and Mie scattering

Time-resolved imaging inside the mixing tube can provide insight into the flashback dynamics. A total of 1200 images were captured using a Nikon 1 v2 high-speed camera, equipped with Nikon AF-S VR Micro-Nikkor 105mm f/2.8G objective, with a resolution of 640×240 pixel<sup>2</sup> at 400 Hz within a field of view of 48×18.5 mm<sup>2</sup>. This results in a pixel resolution of 0.078 mm. The ISO is adjusted at 3200. An in-house developed Matlab code was used to convert images to grayscale frames after enhancing the contrast of the blue component layer of the flame instantaneous image and combining it with the red and green components' layers. The instantaneous grayscale flame image is binarized (i.e., converted to 0 and 1 image). A binarization threshold of 25% of the bright region was employed. The mean of the instantaneous binarized flame images is used to determine the mean progress variable ( $c$ ).

### 2.3.6. Laser Doppler velocimetry (LDV)

In order to determine the PSD of the velocity fluctuations, single sample LDV measurements were conducted. A Coherent Innova 70c-5 Ar-ion 5 W was used to emit a pair of

514.5 nm laser beams (green) which were frequency shifted by 40 MHz using a Bragg cell. The flow field was seeded using TiO<sub>2</sub> particles of approximately 1 μm diameter, which allowed to trace fluctuation frequencies of up to 2.4 kHz. The emitted laser beams were transmitted and received via a TSI TR 60 fiberoptic equipped with TLN06-350 lens of a focal length of 363 mm. The optics configuration formed a focal volume of approximately 1.25 mm in length and 90 μm in diameter. The received scattered light signal from the seeding particles was transmitted to a photo detector module (TSI PDM 1000) which is equipped with a calibration diode for phase delay correction. For deriving the signal phase and frequency, a Doppler burst correlator (TSI FSA 4000) is directly connected to the PDM. A 150 μm slit aperture was used in front of the photomultipliers. The product of the signal frequency times the corresponding fringe spacing (3.74 μm) was used to determine the seeding particles velocity within the focal volume. A total of 500,000 velocity data was found adequate to achieve the convergence of the autocorrelation function. An equidistant resampling procedure is performed on the raw velocity data to calculate the flow velocity at an equal time interval using the nearest neighbor interpolation function using an in-house developed Matlab code. The velocity data was resampled at a frequency of up to 9.6 kHz which corresponds to 4,000,000 velocity data.

## **2.4. Results and discussion**

Since studying turbulent flow field upstream of flame flashback is important for understanding flashback mechanism, the centerline axial mean velocity and its corresponding centerline axial turbulence intensity inside the mixing tube are measured. The flashback's mean width and length inside the mixing tube are also reported to highlight the effect of the mean velocity and turbulence intensity on flashback. To confirm the coupling between flame flashback

and vortex shedding, flame appearance and vortex shedding frequency are determined downstream of the mixing tube exit. Furthermore, the POD flow fields are used to assess the upstream behavior of the vortex shedding and its relationship with flashback. In addition, phase averaging of POD modes is performed to help understand the effect of coherent structures and their transition at different phase angles on periodic flashback.

#### *2.4.1. Mean velocity and turbulence intensity*

The results of the mean flow field show the presence of a central region of low velocity which is expected to promote upstream flame propagation (see Fig. 2.5). The presence of a higher velocity region near the mixing tube's wall makes it unlikely for the wall boundary layer flashback (WBLF) to occur. The contours of the axial turbulence intensity at  $S = 1.15$  and  $Re = 12745$  for all nozzles, and at  $S = 0.79$  and  $Re = 30385$  for N7 of the isothermal flow within the flashback region are plotted in Fig. 2.6. These results show that group A nozzles are expected to exhibit less mixing; whereas N1 and N7 at high swirl number and N7 at low swirl number show high turbulence intensity and consequently greater mixing. Note that higher turbulence intensity in the central region create suitable conditions for high flashback propensity. Knowledge of the centerline turbulence intensity inside the mixing tube is important since periodic flame propagation occurs along the centerline, and combustion instabilities are influenced by the turbulence intensity of the incoming flow [12]. As mentioned earlier, ROI#2 was used to capture the upstream flow field for longer flames into the mixing tube, which is the case with N7 at low swirl number and N1. The measured axial  $V_{rms}$  of the velocity fluctuations was normalized by the mean jet velocity,  $V_j$ , at the mixing tube's exit for each flow condition (8.68 m/s and 20.5 m/s which correspond to  $Re = 12745$  and 30385, respectively).

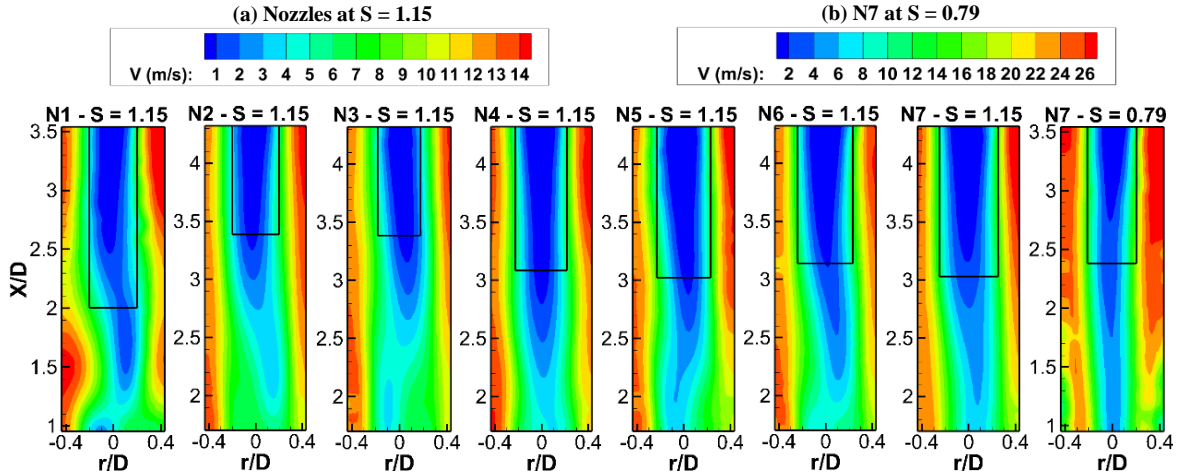


**Fig. 2.5.** Mean velocity contours at  $S = 1.15$  and  $Re = 12745$  for all nozzles, and at  $S = 0.79$  and  $Re = 30385$  for N7 (the rectangle in the central region indicates the mean flashback region).

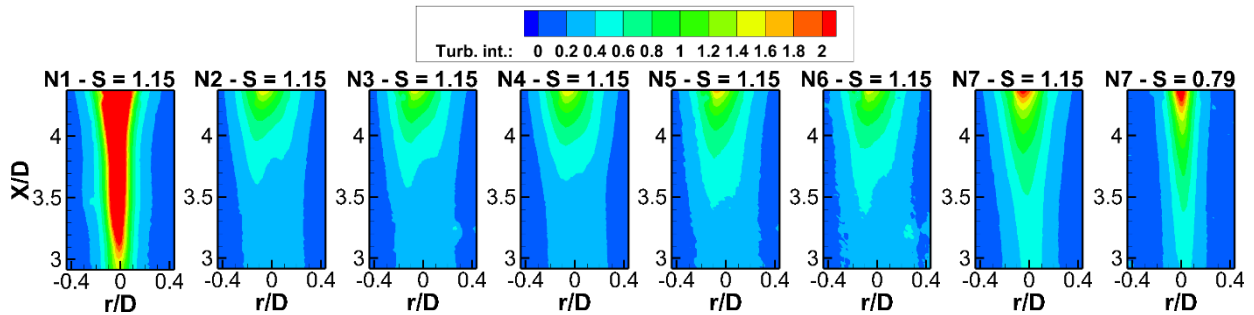


**Fig. 2.6.** Contours of axial turbulence intensity at  $S = 1.15$  and  $Re = 12745$  for all nozzles, and at  $S = 0.79$  and  $Re = 30385$  for N7 in the isothermal case.

The results in Fig. 2.7a reveal that, at high swirl number, the highest centerline velocity,  $V_{CL}$ , is achieved with N2 then N3. It can be observed that the normalized mean centerline axial velocity decreases with increasing  $X/D$ , indicating a significant velocity decay upstream of the flame region. The exception is N7 at low swirl number which exhibits a nearly constant profile indicating a negligible effect of the central nozzle flow on the centerline mean velocity due to the dominance of the swirling airflow momentum on the flow field at  $Re = 30385$ . The results in Figs. 2.7b-c show that N1 exhibits the highest centerline turbulence intensity upstream of the flame region, whereas N7 at low swirl number, N2, N3, and N4 show the lowest. Multi-orifice nozzles exhibit higher axial centerline turbulence intensity than those of group A nozzles.



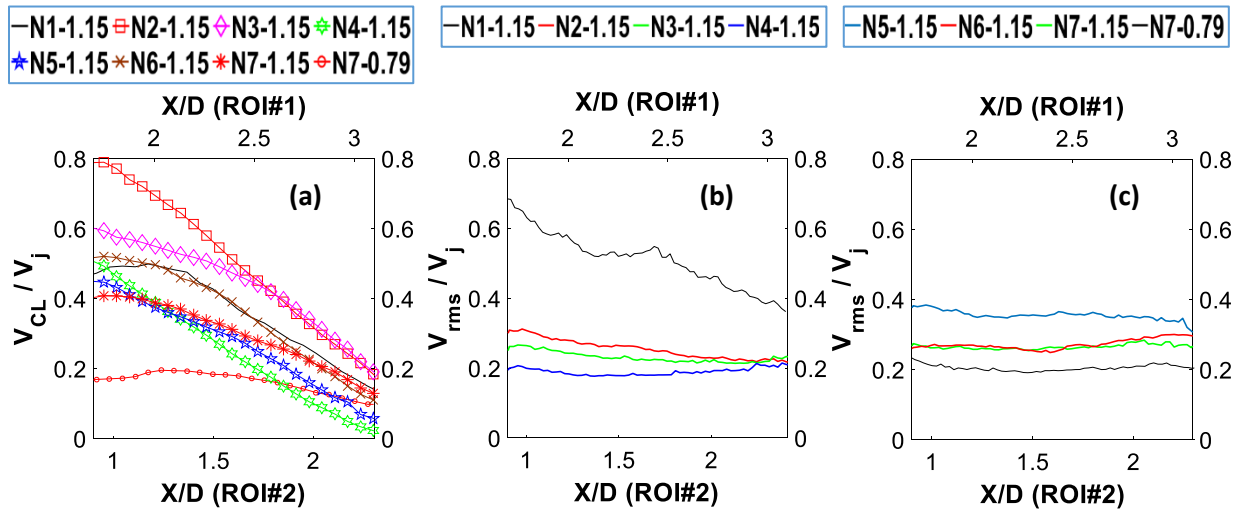


**Fig. 2.7.** Axial profiles of the normalized centerline axial (a) mean velocity, and (b-c) axial turbulence intensity.

Heeger et al. [34] reported that the flashed back flame tip was preceded by a negative axial mean velocity for boundary layer type flashback. However, no negative velocity region upstream of the flashback's mean region is observed in Figs. 2.5 and 2.7a. The instantaneous radial profiles of the axial velocity are extracted just upstream of the flame brush as indicated in Fig. 2.8a. The instantaneous radial profiles are time-averaged in order to obtain the conditional mean axial velocity profile. These profiles show the presence of a negative axial mean velocity just upstream of the flashed back flame front for all central nozzles at the high swirl number. There is no evidence of the presence of a negative axial mean velocity with N7 at low swirl number (see Fig. 2.8b). This is attributed to the fact that the flame may experience upstream convection-type propagation without being preceded by a negative axial velocity [34]. Also, the flashed back flame tip could rotate or does not always coincide with the 2D laser sheet plane [31], and consequently the absence of a negative velocity zone.

An example of the presence of a negative velocity upstream of the flashed back flame is shown in Figs. 2.8c,d. Further discussion on the flame appearance inside the mixing tube is reported in the

next section. Based on this result, group A should have less flashback propensity owing to its high centerline axial velocity (for N2 and N3) and low centerline axial turbulence intensity (for N2, N3, and N4). In addition, increasing the number of peripheral orifices of the central nozzle weakens the effect on the centerline flow momentum and, hence, increase the flashback propensity.

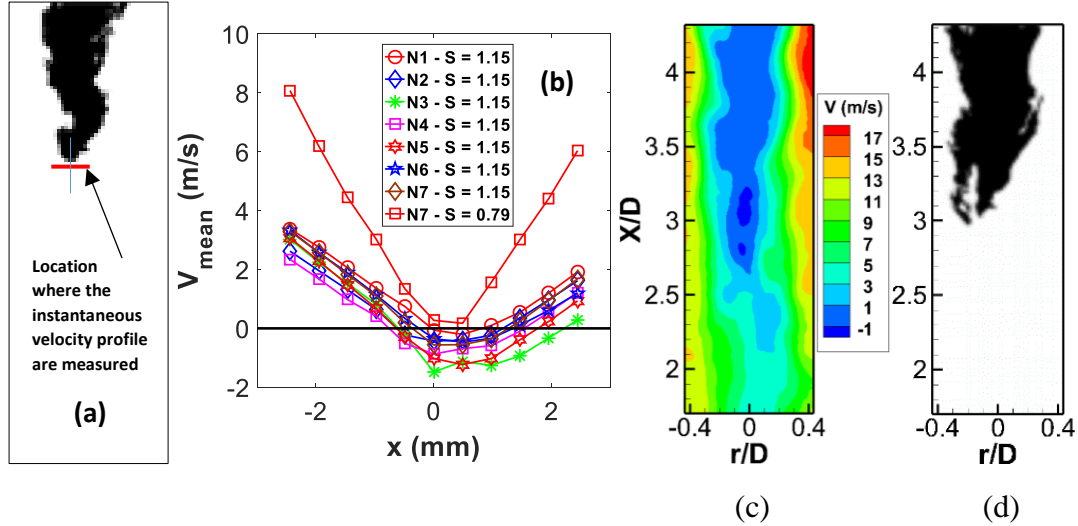


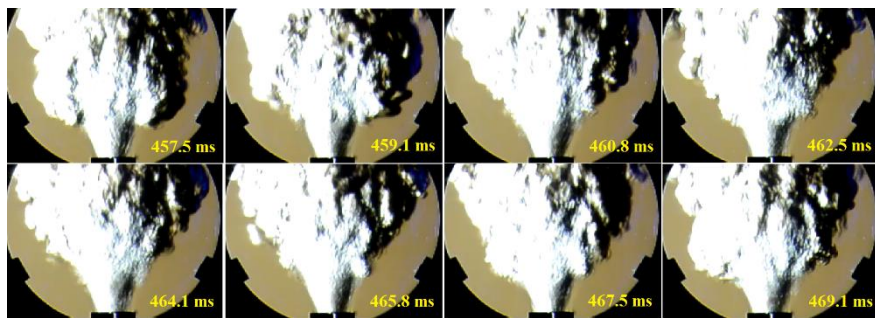
**Fig. 2.8.** (a) Illustration of the location where the axial velocity radial profiles upstream of the flashed back flame are measured, (b) radial profiles of the conditional mean axial velocity for different central nozzles at  $S = 1.15$  and N7 at  $S = 0.79$ , (c) instantaneous velocity contours of N7 at  $S = 1.15$ , and (d) the corresponding extracted area of the instantaneous flashed back flame.

#### 2.4.2. Frequency of the coherent structures and flame appearance

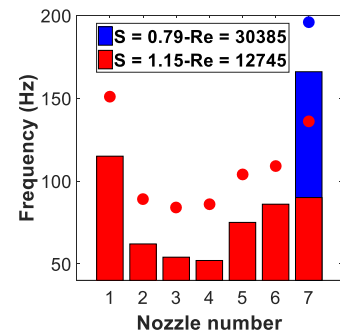
Schlieren imaging technique was used to determine the coherent structures' frequency and provide information on flame appearance downstream of the mixing tube exit. The frequency of vortex shedding is determined by calculating the arithmetic average of ten consecutive frequencies of the coherent structures for each test case (as  $\sum_1^{10}(1/t_{cycle})/10$ , where  $t_{cycle}$  is the time duration of one cycle). The onset of a cycle of the coherent structures is associated with the presence of two large eddies (upper and lower) on each side of the flame (see Fig 2.9a,  $t = 457.5$  ms). These results

were confirmed by the frequency values obtained from the PSD of the velocity fluctuations measured by the LDV (see Fig. 2.9b).

The present results show that group A exhibits lower vortex shedding frequencies than those of group B, as shown in Fig. 2.9b. In addition, N1 exhibits the highest frequency at high swirl number suggesting a significant effect of the nozzle's bluff solid area on vortex shedding strength. The highest frequency is achieved with N7 at low swirl number. It is observed that, for all flames at high swirl number, the generated vortex shedding is symmetric (see Fig. 2.9c) and independent of the nozzle geometry, while the coherent structures are asymmetric for N7 at low swirl number (see Fig. 2.9d). POD analysis downstream of the mixing tube exit is performed in the next section to investigate whether these asymmetric coherent structures are helical vortex shedding or PVC. Although acoustic modes were not experimentally measured, different noise levels were sensed with different nozzle geometry and swirl number. The tendency of vortex shedding to be symmetric is higher when acoustic instabilities occur [35]. This may explain why noise level was higher at high swirl number.



(a)



(b)

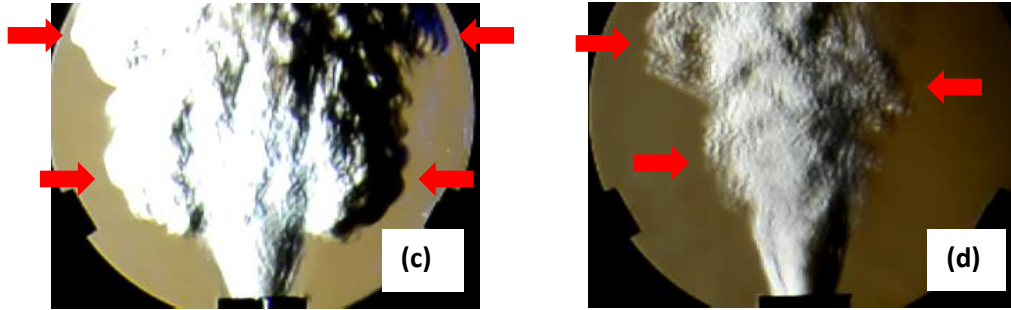


**Fig. 2.9.** (a) Eight successive Schlieren images with equal time spacing during one cycle of vortex shedding, (b) coherent structures' frequency of different central nozzles, where the bars represent the frequency extracted from Schlieren images and the circular markers represent the frequency peaks from LDV PSD, and (c,d) Schlieren images of the flame of N1 at high swirl number (left) and N7 at low swirl number (right) (the red arrows points to the position of the large eddies).

Time-resolved imaging is performed to shed light on the flashback dynamics inside the mixing tube. Figure 2.10a depicts the contours of the mean progress variable (c) for different cases. It can be observed that group A nozzles show smaller flashback length and width inside the mixing tube, particularly for N2 and N3. N1 exhibits the largest flame region inside the mixing tube followed by N7 at low swirl number. The wider flames of N1 and group B nozzles can be attributed to the higher turbulence intensity (see Figs. 2.7b,c) which causes flame brush widening [36]. The results reveal that the flashback region oscillates with time which indicates that it is periodic for all nozzles. To confirm the periodicity of flashback, the power spectral densities of the width and length fluctuations of the flashed back flame are determined (e.g., N1, Figs. 2.10b,c). The results show that, for example, N1 flame's width and length fluctuate at a well-defined frequency (26.95 Hz), which confirms that the flashback is periodic. The flashback's mean region is estimated by calculating the flashback's mean length inside the mixing tube and flame mean width near the mixing tube exit (at  $X/D = 4.3$ ). The extracted flame areas from Mie scattering images (Fig. 2.2c) for each instantaneous velocity vectors map were used to determine the flashed back flame's mean region; that is, the mean width and length at each test case. Note that the instantaneous flashback

length is estimated as the distance between the mixing tube's exit plane and the farthest upstream edge of the dark region in Fig. 2.2c; and the instantaneous flashback's width is determined as the distance between the lateral/radial boundaries/edges of the dark region at the mixing tube exit.

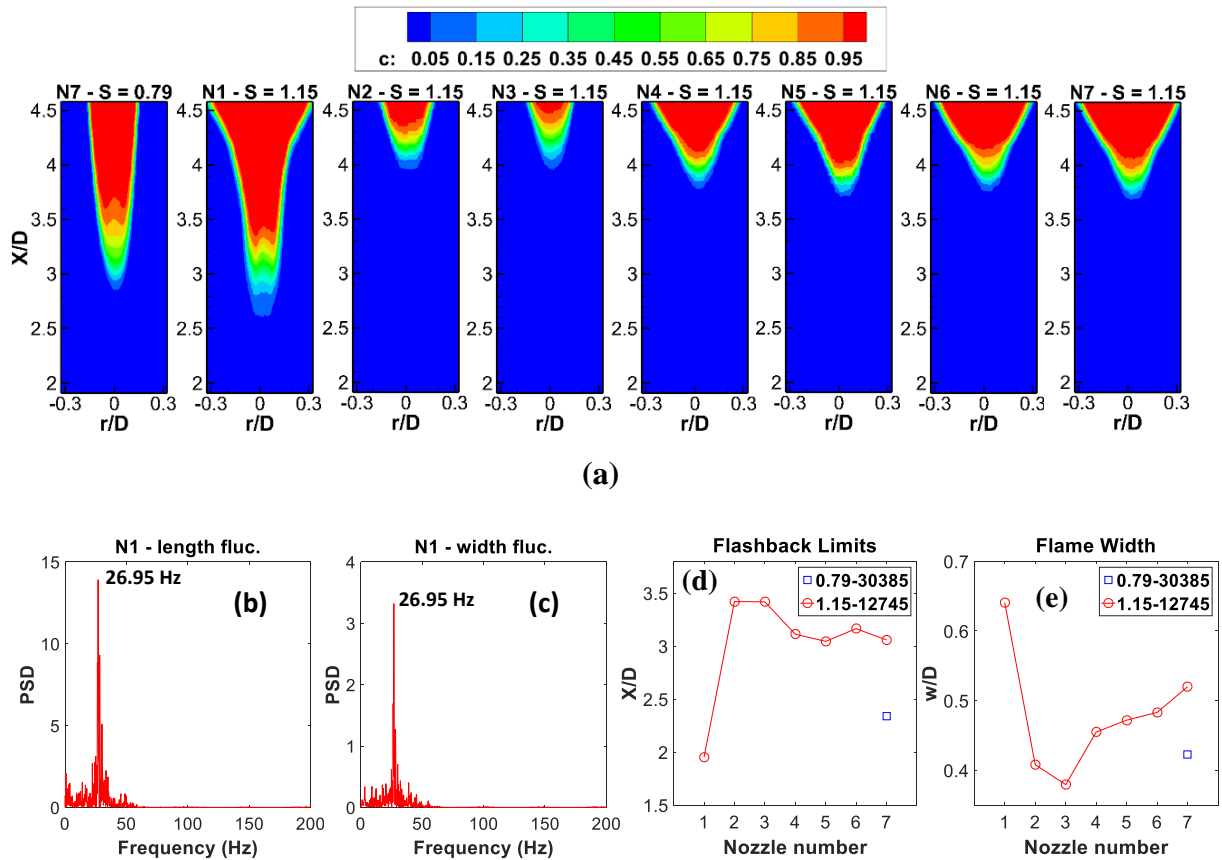


**Fig. 2.10.** (a) Contours of the mean progress variable “c”, (b) normalized power spectral density of the fluctuations of the flame length of N1 inside the mixing tube, (c) normalized power spectral density of the fluctuations of the flame width of N1 inside the mixing tube, (d) the mean flame length inside the mixing tube for each central nozzle, and (e) the mean flame width slightly below the mixing tube exit for each central nozzle

Flashback's mean region extracted from Mie scattering follows the same trend of those extracted from the mean progress variable contours (see Figs. 2.10d,e). The larger the bluff solid area is, the greater the recirculation zones created downstream of the bluff body, which enhances mixing between the central flow and swirling airflow and, consequently increases flashback

propensity. These results indicate that swirling airflow's Reynolds number, nozzle bluff body area, number of peripheral orifices (group B) and their shape (group A) play a key role on vortex shedding frequency and hence flashback propensity. Moreover, the coherent structures' frequency significantly affects the flashback length inside the mixing tube, and the centerline turbulence intensity at high swirl number (see Figs. 2.7b,c).

#### 2.4.3. *POD results*

POD was applied to the instantaneous velocity fields to capture coherent structures in order to provide information on the energy and behavior of vortex shedding. POD analysis was performed on the velocity vectors just upstream of the maximum instantaneous flashback region (based on Mie scattering) for a constant area ( $710 \times 800 \text{ pixel}^2$ ). This procedure is done for two reasons; first, it helps to understand the behavior of the coherent structures just upstream of the flashback region; and second, is that capturing a smaller region can result in an increase in modal energy fraction of the first modes [33]. POD analysis of velocity vector fields at different test cases is presented in Fig. 2.11. The contribution of the first two modes to the total modes energy ( $\lambda_{1,2} / E_{\text{tot}}$ ) ranges from 16% to 37% depending on the nozzle geometry and swirl number. It is observed that the energy of the summation of the first four modes of group A is lower than that of group B; while it is the highest for N1 and N7 at low swirl number (see Fig. 2.11). In other words, the swirling airflow rate, nozzle bluff solid area and the angled peripheral multi orifices all contribute to increasing the energy of coherent structures. The findings of POD modal energy reveal the existence of a strong correlation between the energy of coherent structures and flashback length inside the mixing tube. That is, nozzles (N7 at low swirl number, and N1 and N7 at high swirl number), which show high modal energy (see Fig. 2.11b), are found to experience larger size of

flashed back flames inside the mixing tube (see Figs. 2.10a,d,e). That is, an increase in the coherent structures' energy inside the mixing tube is found to be responsible for increasing the flashback propensity. Furthermore, POD analysis downstream of the mixing tube exit demonstrated the dominance of the PVC in the first two POD modes for only N7 at low swirl number; whereas all cases at high swirl number show the dominance of the symmetric vortex shedding (not shown here). The suppression of the PVC and the dominance of the symmetric vortex shedding can be attributed to the flow conditions [37], and mainly to the equivalence ratio [38]. For instance, PVC is associated with high flame tip eccentricity, which can explain the absence of the negative velocity in Fig. 2.8b and show good agreement with the results reported in [31].

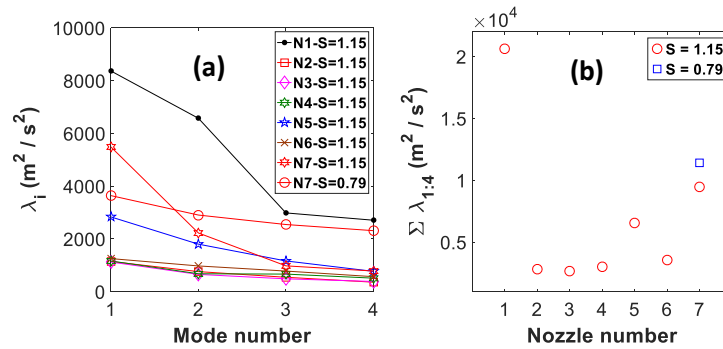


**Fig. 2.11.** (a) POD modal energy of the first four modes and (b) POD modal energy of the summation of the first four modes for different central nozzles at different swirling airflow Reynolds number and swirl number

#### 2.4.4. Phase averaging of the coherent structures

The evolution and transition of vortical structures are presented and discussed in this section to provide insight into the vortices behavior upstream of the flame region and help understand the mechanism of periodic flashback. For the purpose of phase averaging, the POD time coefficients are calculated and used to determine the phase angle ( $\varphi$ ) for each snapshot  $i$ . The

linear superposition of the first two modes was calculated and their averages were obtained for eight phases ( $45^\circ$ ,  $90^\circ$ ,  $135^\circ$ ,  $180^\circ$ ,  $225^\circ$ ,  $270^\circ$ ,  $315^\circ$ ,  $360^\circ$ ).

Analysis of the results in Fig. 2.12 reveals that flashback's mean region is always preceded by strong vortical structures. These vortical structures are associated with the reversal flow which can restrict the axial flow and facilitate upstream flame propagation. These vortices can be convected periodically in the downstream direction (vortex shedding) towards the flame region. The central nozzle geometry has an affect whether the vortical structures are sustained or suppressed. The coherent structures for N7 at low swirl number appear to be asymmetric which confirms the aforementioned findings using Schlieren imaging (see Fig. 2.12, N7 -  $S = 0.79$ ,  $\phi = 90^\circ$  and  $135^\circ$ ). It can be observed that N7 at high swirl number exhibits the largest primary shed vortex upstream of the flashback's mean region (see Fig. 2.12, N7 -  $S = 1.15$ ,  $\phi = 90^\circ$ ). This can explain the large flame area inside the mixing tube as stated in [39]. However, group A exhibits the smallest vorticity magnitude upstream of the mean flashback region (see Fig. 2.12, N3 as an example). In addition, compared to group A nozzles, the vortical structures of group B nozzles are larger in magnitude, while they are the largest in magnitude for N1 and N7 at high and low swirl numbers, respectively. Vortical structures with a large magnitude can accelerate the fuel-air mixing and hence create conditions suitable for the onset of flashback.



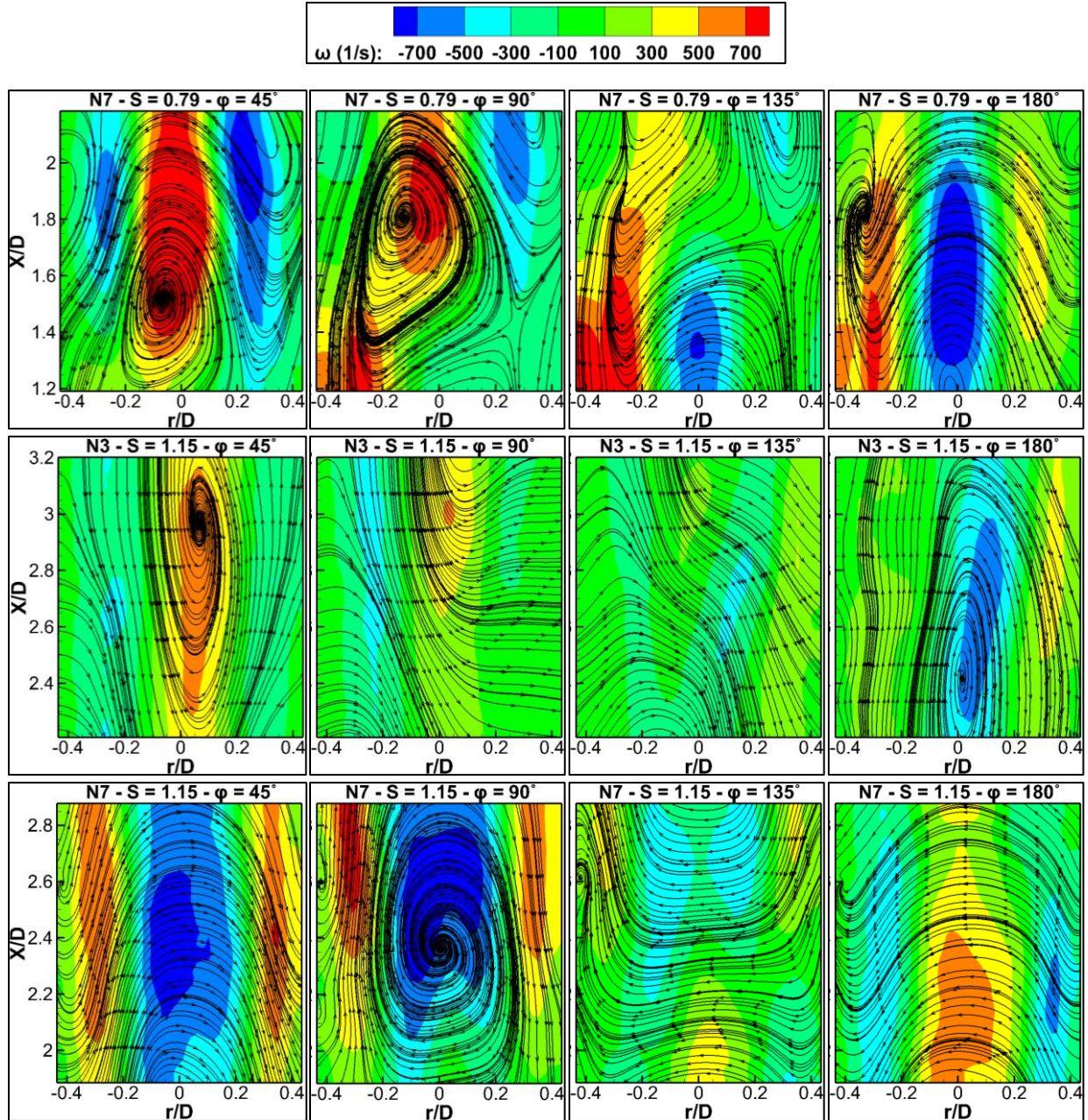


**Fig. 2.12.** Vorticity fields of the phase averaging of the linear superposition of the first two POD modes along with streamlines for N7 at  $S = 0.79$  and  $Re = 30385$ , and N3 and N7 at  $S = 1.15$  and  $Re = 12745$  (note that  $X/D$  values on the vertical axes are different for each case).

These findings highlight the coupling between coherent structures and flashback propensity and the parameters that affect them. The equivalence ratio and Reynolds number determine the dominant coherent structures (i.e., PVC or vortex shedding) in the flow. Once the

vortex shedding is dominant, the flashback propensity (flashback's mean region) becomes depend on the vortex shedding strength and frequency. This is indicated by comparing the results in Fig. 2.9b and Figs. 2.10a,d,e with those in Fig. 2.11. The nozzle bluff solid area, which is the largest for N1, increases the vortex shedding strength and hence the flashback propensity. Nonetheless, the significance of the effect of bluff solid area on flashback propensity is less when the vortex shedding is suppressed or not well-established (at  $S = 0.79$ ). In this case, the effect of the central axial flow momentum becomes more significant than that of the bluff solid area, as weaker momentum (similar to that of N7) promotes the formation of coherent structures and increases the flashback propensity. Under this condition, the dominant coherent structures convert into PVC which results in high flame tip eccentricity (observed in the instantaneous high-speed flame images). The phase averaging upstream of the flashback's mean region proves that flashback is controlled by the PVC, despite the absence of the negative velocity upstream of the flashback's mean region (see Fig. 2.8b). It can be concluded that regardless of the swirl number and swirling airflow Reynolds number, increasing the coherent structures' strength and frequency increase the flashback propensity. However, nozzle geometry can play a key role in preventing flashback, which is apparent at low swirl number where there is no flashback prior to blowout with all central nozzles except for N7. Therefore, the optimum central nozzle geometry that weakens flashback propensity should have a small bluff solid area, such as tapered nozzles, to mitigate the vortex shedding and facilitate relatively high centerline axial momentum. Asymmetric multi-orifice tapered nozzle may have the ability to promote sufficient mixing inside the mixing tube that is required for downstream flame stability.

#### 2.4.5. Error analysis

For PIV measurements, the main sources of uncertainty are the truncation, measurement, and precision errors. To reduce the truncation error, the time separation between each image pair was selected to allow particles' displacement of a distance equivalent to 1/4 of the interrogation area. This can be achieved by choosing a time separation of 10  $\mu\text{s}$  between each image pair. Increasing the particle image density was found to minimize the measurement uncertainty by increasing the correlation peaks. Optimum seeding particles' density of higher than 12 particles per interrogation area was employed. The maximum uncertainty due to truncation and measurement errors was estimated to be  $\pm 1\%$ . High accuracy sub-pixel interpolation was used instead of the Gaussian sub-pixel interpolation to minimize the effect of the peak-locking. As a result, the estimated displacement error was reduced to  $\pm 6\%$ . The estimated error in the interpolation and uncertainty due to image processing calculations was found less than  $\pm 1\%$ . The thermophoretic force significantly affects the velocity estimation near the flame inside the mixing tube. That is, it was found that the velocity change due thermophoretic force is proportional to  $\sqrt{T}dT/dx$ , where  $T$  is the temperature and  $x$  is the distance normal to the flame front [40]. However, due to the inability to measure temperature inside the mixing tube in the present study, determining velocity change due to thermophoretic force was not possible. Nevertheless, unlike other seeding particles such as olive oil drops which evaporate at  $\sim 650$  K, incense particles, which were used in the present study, disappeared at lower temperatures than  $\sim 650$  K and allowed collecting the velocity vectors only in the low temperature non-reacting regions. To guarantee less velocity error due to thermophoretic force, all velocity fields or profiles were considered starting only from 2 mm below the most upstream point of Mie scattering image that has no seeding particles. The velocity data uncertainty was estimated using  $e = \sqrt{B^2 + tP^2}$ , where  $B$  is the bias

error,  $t$  is  $t_{critical}$  in the student's t-distribution ( $t = 1.96$ ), and  $P$  is the precision error. The maximum estimated uncertainty for the velocity data was found around  $\pm 0.3$  m/s.

For LDV measurements, the maximum estimated uncertainty of the velocity was around  $\pm 0.25$  m/s. It should be noted that the time resolution of the resampled velocity data was  $\sim 0.114$  ms and the lowest integral time scale was 0.65 ms. This resulted in an error in estimating the integral time scale of about  $\pm 6\%$ . The relative uncertainty of the instantaneous velocity was estimated using

$$e_V/V = \sqrt{(e_{f_D}/f_D)^2 + (e_{d_f}/d_f)^2},$$

where  $d_f$  is the fringe spacing,  $f_D$  is the Doppler frequency,  $e_{d_f}$  is the uncertainty of the fringe spacing, and  $e_{f_D}$  is the uncertainty of the Doppler frequency.

The resultant uncertainty in the instantaneous velocity measurements was approximately  $\pm 0.005$ .

The uncertainty of flame front positions (based on Mie scattering) depends on several parameters such as the axial distance ( $X/D$ ), binarization threshold, noise removal filter, image resolution, and laser sheet thickness. A binarization threshold of 25% of the unburned region and the use of a median filter provided the optimum conditions for a better detection of the flame front position. The maximum uncertainty in flame front position was estimated to be around  $\pm 0.35$  mm. The uncertainty of the length and width of the flame inside the mixing tube based on Mie scattering and time-resolved imaging were calculated using  $e = \sqrt{B^2 + tP^2}$ , where  $t = 1.963$ . The maximum uncertainty of the flame length inside the mixing tube was estimated to be  $\pm 1.24$  mm and  $\pm 1.43$  mm based on the time-resolved and Mie scattering imaging, respectively; whereas the maximum uncertainty of the flame width was estimated to be  $\pm 0.68$  mm and  $\pm 0.71$  mm based on time-resolved and Mie scattering imaging, respectively.

## 2.5. Conclusions

The flow field in a mixing tube under flame flashback conditions was documented using PIV in order to investigate the effect of central nozzle geometry and swirling airflow strength on coherent structures and their relationship with flashback propensity. In addition, Schlieren imaging technique was used to determine the frequency of vortex shedding and flame appearance downstream of the mixing tube. Time-resolved imaging was used to investigate the dynamics of flashed back flames while Mie scattering was used to determine the flashback's mean region in the mixing tube. The results showed that coherent structures play an important role in causing and strengthening periodic flashback. The formation of vortex shedding was promoted at high equivalence ratio and high swirl number; whereas PVC was formed at high Reynolds number and low equivalence ratio. The presence of the coherent structures was found responsible for increasing the flashback propensity regardless of the swirling airflow momentum (Reynolds number) and central nozzle geometry. At low swirl number, the flashback can still occur at low centerline axial momentum from the central nozzle, since the conditions for PVC suppression (such as the presence of strong axial momentum) were not achieved. Increase in the bluff solid area (such as for N1) enhances the strength of vortex shedding and, consequently the flashback's mean region inside the mixing tube. Furthermore, decreasing the bluff solid area (as for group A) reduces the coherent structures strength and, hence, decreases the flashback propensity, particularly for N3. On the other hand, reducing the flow momentum of the central nozzle (such as with group B nozzles) increases the coherent structures energy and, therefore, increases the flashback propensity. The higher the frequency of vortex shedding is, the larger flashback's mean region inside the mixing tube as observed in the mean progress variable contours. It was found that the number of nozzle's peripheral orifices, nozzle's bluff solid area, and the centerline axial turbulence intensity

significantly affect the vortex shedding frequency. For group B nozzles, the frequency increases with the number of orifices. Both high turbulence intensity and large bluff solid area exhibited by N1 and group B nozzles were found to increase the vortex shedding frequency. Optimizing the mixing (via controlling unmixedness) inside the mixing tube is necessary to control the flashback propensity. However, using a central nozzle with no bluff solid area would result in inadequate mixing inside the mixing tube [26] and consequently flame blowout. Swirl promotes flashback propensity by increasing the upstream mixing. However, at low swirl number, only N7 experiences flashback. On the other hand, at high swirl number, flashback propensity depends also on the central nozzle geometry. Therefore, swirl is not the only main parameter. Consequently, in order to weaken the coherent structures' strength and hence flashback propensity, an optimum central nozzle geometry that provides smaller bluff solid area and relatively high central flow momentum should be used. This type of nozzle should resist to the formation of PVC and vortex shedding.

## 2.6. References

- [1] A. M. Elbaz, M. F. Zayed, M. Samy, W. L. Roberts, and M. S. Mansour, "The flow field structure of highly stabilized partially premixed flames in a concentric flow conical nozzle burner with coflow," *Exp. Therm. Fluid Sci.*, vol. 73, pp. 2–9, 2016.
- [2] H. G. Im and J. H. Chen, "Structure and propagation of triple flames in partially premixed hydrogen-air mixtures," *Combust. Flame*, vol. 119, no. 4, pp. 436–454, 1999.
- [3] M. S. Mansour, A. M. Elbaz, and M. Samy, "The stabilization mechanism of highly stabilized partially premixed flames in a concentric flow conical nozzle burner," *Exp. Therm. Fluid Sci.*, vol. 43, pp. 55–62, 2012.
- [4] H. Xue and S. K. Aggarwal, "NO<sub>x</sub> emissions in n-heptane/air partially premixed flames,"

- Combust. Flame*, vol. 132, pp. 723–741, 2003.
- [5] S. Meares and A. R. Masri, “A modified piloted burner for stabilizing turbulent flames of inhomogeneous mixtures,” *Combust. Flame*, vol. 161, no. 2, pp. 484–495, 2014.
- [6] T. S. Cheng, Y. C. Chao, D. C. Wu, H. W. Hsu, and T. Yuan, “Effects of partial premixing on pollutant emissions in swirling methane jet flames,” *Combust. Flame*, vol. 125, no. 1–2, pp. 865–878, 2001.
- [7] H. S. Zhen, C. W. Leung, and C. S. Cheung, “A comparison of the thermal, emission and heat transfer characteristics of swirl-stabilized premixed and inverse diffusion flames,” *Energy Convers. Manag.*, vol. 52, no. 2, pp. 1263–1271, 2011.
- [8] J. Fritz, M. Kröner, and T. Sattelmayer, “Flashback in a Swirl Burner With Cylindrical Premixing Zone,” *J. Eng. Gas Turbines Power*, vol. 126, no. 2, p. 276, 2004.
- [9] S. Candel, “Combustion dynamics and control: progress and challenges,” *Proc. Combust. Inst.*, vol. 29, pp. 1–28, 2002.
- [10] C. Xiouris and P. Koutmos, “An experimental investigation of the interaction of swirl flow with partially premixed disk stabilized propane flames,” *Exp. Therm. Fluid Sci.*, vol. 35, no. 6, pp. 1055–1066, 2011.
- [11] S. Joo, J. Yoon, J. Kim, M. Lee, and Y. Yoon, “NO<sub>x</sub> emissions characteristics of the partially premixed combustion of H<sub>2</sub>/CO/CH<sub>4</sub> syngas using artificial neural networks,” *Appl. Therm. Eng.*, vol. 80, pp. 436–444, 2015.
- [12] S. Y. Lee, S. Seo, J. C. Broda, S. Pal, and R. J. Santoro, “An experimental estimation of mean reaction rate and flame structure during combustion instability in a lean premixed gas turbine combustor,” *Proc. Combust. Inst.*, vol. 28, no. 1, pp. 775–782, 2000.
- [13] B. Dam, G. Corona, M. Hayder, and A. Choudhuri, “Effects of syngas composition on

- combustion induced vortex breakdown (CIVB) flashback in a swirl stabilized combustor,” *Fuel*, vol. 90, no. 11, pp. 3274–3284, 2011.
- [14] O. Tuncer, S. Acharya, and J. H. Uhm, “Dynamics, NO<sub>x</sub> and flashback characteristics of confined premixed hydrogen-enriched methane flames,” *Int. J. Hydrogen Energy*, vol. 34, no. 1, pp. 496–506, 2009.
- [15] Y. Huang and V. Yang, “Dynamics and stability of lean-premixed swirl-stabilized combustion,” *Prog. Energy Combust. Sci.*, vol. 35, no. 4, pp. 293–364, 2009.
- [16] K. C. Schadow and E. Gutmark, “Combustion instability related to vortex shedding in dump combustors and their passive control,” *Prog. Energy Combust. Sci.*, vol. 18, pp. 117–132, 1991.
- [17] V.-Z. Marco Osvaldo, S. Nicholas, V.-M. Agustín, and D. la R.-U. Daniel, “Flashback Avoidance in Swirling Flow Burners,” *Ing. Investig. y Tecnol.*, vol. 15, no. 4, pp. 603–614, 2014.
- [18] R. W. Schefer, M. Namazian, J. Kelly, and M. Perrin, “Effect of confinement on bluff-body burner recirculation zone characteristics and flame stability,” *Combust. Sci. Technol.*, vol. 120, no. 1–6, pp. 185–211, 1996.
- [19] J. R. Dawson, R. L. Gordon, J. Kariuki, E. Mastorakos, A. R. Masri, and M. Juddoo, “Visualization of blow-off events in bluff-body stabilized turbulent premixed flames,” *Proc. Combust. Inst.*, vol. 33, no. 1, pp. 1559–1566, 2011.
- [20] S. Chaudhuri, S. Kostka, M. W. Renfro, and B. M. Cetegen, “Blowoff dynamics of bluff body stabilized turbulent premixed flames,” *Combust. Flame*, vol. 157, no. 4, pp. 790–802, 2010.
- [21] S. Chaudhuri and B. M. Cetegen, “Blowoff characteristics of bluff-body stabilized conical



- premixed flames in a duct with upstream spatial mixture gradients and velocity oscillations,” *Combust. Sci. Technol.*, vol. 181, no. 4, pp. 555–569, 2009.
- [22] G. Rigas, L. Esclapez, and L. Magri, “Symmetry breaking in a 3D bluff-body wake,” *Cent. Turbul. Res. Proc. Summer Progr. 2016*, pp. 1–10, Mar. 2017.
- [23] R. C. Steele, L. H. Cowell, S. M. Cannon, and C. E. Smith, “Passive control of combustion instability in lean premixed combustor,” *J. Eng. Gas Turbines Power*, vol. 122, no. 3, pp. 1–8, 2000.
- [24] B. B. Dally, A. R. Masri, R. S. Barlow, and G. J. Fiechtner, “Instantaneous and mean compositional structure of bluff-body stabilized nonpremixed flames,” *Combust. Flame*, vol. 114, no. 1–2, pp. 119–148, 1998.
- [25] T. G. Reichel, S. Terhaar, and O. Paschereit, “Increasing Flashback Resistance in Lean Premixed Swirl-Stabilized Hydrogen Combustion by Axial Air Injection,” *J. Eng. Gas Turbines Power*, vol. 137, no. 7, pp. 71503–71509, Jul. 2015.
- [26] D. Galley, S. Ducruix, F. Lacas, and D. Veynante, “Mixing and stabilization study of a partially premixed swirling flame using laser induced fluorescence,” *Combust. Flame*, vol. 158, no. 1, pp. 155–171, 2011.
- [27] C. Mayer, J. Sangl, T. Sattelmayer, T. Lachaux, and S. Bernero, “Study on the operational window of a swirl stabilized syngas burner under atmospheric and high pressure conditions,” *J. Eng. Gas Turbines Power*, vol. 134, pp. 1–11, 2012.
- [28] A. Schönborn, P. Sayad, and J. Klingmann, “Influence of precessing vortex core on flame flashback in swirling hydrogen flames,” *Int. J. Hydrogen Energy*, vol. 39, pp. 20233–20241, 2014.
- [29] S. K. Dhanuka, J. E. Temme, J. F. Driscoll, and H. C. Mongia, “Vortex-shedding and mixing

- layer effects on periodic flashback in a lean premixed prevaporized gas turbine combustor,” *Proc. Combust. Inst.*, vol. 32, pp. 2901–2908, 2009.
- [30] S. Kheirkhah, Ö. L. Gülder, G. Maurice, F. Halter, and I. Gökalp, “On periodic behavior of weakly turbulent premixed flame corrugations,” *Combust. Flame*, vol. 168, pp. 147–165, 2016.
- [31] D. Ebi and N. T. Clemens, “Experimental investigation of upstream flame propagation during boundary layer flashback of swirl flames,” *Combust. Flame*, vol. 168, pp. 39–52, 2016.
- [32] C. A. G. Casanova, “Experimental Measurement of Laminar Flame Speed of a Novel Liquid Biofuel 1,3 Dimethoxyoctane,” University of Manitoba, 2015.
- [33] M. Stöhr, R. Sadanandan, and W. Meier, “Phase-resolved characterization of vortex-flame interaction in a turbulent swirl flame,” *Exp. Fluids*, vol. 51, no. 4, pp. 1153–1167, 2011.
- [34] C. Heeger, R. L. Gordon, M. J. Tummers, T. Sattelmayer, and A. Dreizler, “Experimental analysis of flashback in lean premixed swirling flames: Upstream flame propagation,” *Exp. Fluids*, vol. 49, no. 4, pp. 853–863, 2010.
- [35] S. Kostka, A. C. Lynch, B. C. Huelskamp, B. V. Kiel, J. R. Gord, and S. Roy, “Characterization of flame-shedding behavior behind a bluff-body using proper orthogonal decomposition,” *Combust. Flame*, vol. 159, pp. 2872–2882, 2012.
- [36] A. Nauert, P. Petersson, M. Linne, and A. Dreizler, “Experimental analysis of flashback in lean premixed swirling flames: Conditions close to flashback,” *Exp. Fluids*, vol. 43, no. 1, pp. 89–100, 2007.
- [37] A. M. Steinberg, C. M. Arndt, and W. Meier, “Parametric study of vortex structures and their dynamics in swirl-stabilized combustion,” *Proc. Combust. Inst.*, vol. 34, pp. 3117–

3125, 2013.

- [38] N. Syred, “A review of oscillation mechanisms and the role of the precessing vortex core (PVC) in swirl combustion systems,” *Prog. Energy Combust. Sci.*, vol. 32, no. 2, pp. 93–161, 2006.
- [39] T.-W. Lee and D. A. Santavicca, “Flame Front Geometry and Stretch During Interactions of Premixed Flames with Vortices,” *Combust. Sci. Technol.*, vol. 90, no. 1–4, pp. 211–229, 1993.
- [40] S. Kheirkhah, “Experimental study of turbulent premixed combustion in V-shaped flames,” PhD thesis, University of Toronto, 2016.

# **Chapter 3: Effect of Fuel Nozzle Geometry on a Swirling Partially Premixed Methane Flame**

## **3.1. Abstract**

This paper presents an experimental study of the effect of fuel nozzle geometry on swirling partially premixed methane flames; where the focus is put on the ensuing flowfield and its role on coherent structures' suppression. The burner consists of a central interchangeable fuel nozzle surrounded by a swirling co-airflow where both discharge into a short mixing tube. The nozzle geometry is classified into two groups; namely single- and multi-orifice nozzles. The swirling motion of the co-airflow is produced using a radial-type swirl generator with a swirl number of 1.15. The flowfield characteristics and coherent structures are documented using particle image velocimetry (PIV). Flame front dynamics are captured using Mie scattering technique. Quantitative laser sheet (QLS) is used to qualitatively shed light on the mixing characteristics downstream of the mixing tube exit, and laser Doppler velocimetry (LDV) is used to extract the coherent structures' peak frequency from the power spectra. The results revealed that the fuel nozzle geometry significantly affects the mean flowfield, mean and RMS of the flame front location, flame front asymmetry, and coherent structures' amplitude. Higher spread rate and faster decay caused by single-orifice nozzles inside the mixing tube result in divergent flames with higher degree of flame front asymmetry downstream of the mixing tube exit. On the other hand, multi-orifice nozzles mitigate coherent structures, enhance mixing, and hence, promote the most appropriate conditions for coherent structures' suppression.

### 3.2. Introduction

Partially premixed flames (PPFs) are extensively used in several practical applications such as industrial burners/furnaces, gas turbine combustors, direct injection internal combustion engines, and domestic combustion devices owing to their improved stability compared to those of non-premixed and premixed flames [1]. Unlike premixed and non-premixed flames, which are characterized by a dominant reaction zone [2], PPFs are characterized by multiple reaction zones. The presence of these reaction zones allows thermochemical and fluid dynamic interaction between the different reaction zones, which help to sustain chemical reactions and hence improve flame stability [1,2]. Premixed flames produce lower  $\text{NO}_x$  emissions than non-premixed, however, they have high propensity for static and dynamic instabilities [3].

Although PPFs have comparable emissions to lean premixed flames, they are still prone to combustion instabilities [4]. The unmixedness and inhomogeneity in PPFs provoke thermoacoustic instabilities [4]. In order to improve flame stability, swirling combustion is used in numerous practical combustion devices such as internal combustion engines, gas turbine combustors and industrial burners. Swirl forms a large adverse pressure gradient, which results in the formation of vortex breakdown that aerodynamically anchors the flame and improves its stability. In addition, swirl enhances fuel-air mixing, increases residence time, and consequently improves combustion and thermal efficiency [5,6]. At high swirl number (roughly for  $S > 0.6$ ), swirling flowfield is characterized by the formation of a central recirculation zone (CRZ). Under certain flow conditions, the occurrence of precessing vortex core (PVC) may manifest, particularly when the CRZ becomes unstable where the PVC rotates around the CRZ boundaries (see Fig. 1.2 in [3]). PVC contributes to the enhancement of mixing which in turn improves thermal/combustion efficiency. However, PVC increases thermoacoustic oscillations amplitude [7], modulate air-fuel

mixing rate and hence alter combustion process [8], and induce integral heat release fluctuations [9]. Even with PVC suppression, swirl still produces flames which are unstable and prone to instabilities [3]. It was reported that premixing fuel with air may restore PVC after its suppression [3].

PVC is a time-dependent and three-dimensional, which makes it difficult to understand. The frequency of PVC is found to be dependent on burner configuration, flow rate, mode of fuel entry (axial, radial and tangential) and swirl number. Note that axial fuel entry consists of injecting the fuel parallel to the axis of a burner/combustor; whereas tangential fuel entry consists of injecting the fuel in the azimuthal direction which causes a rotation around the axis of a burner/combustor. PVC has a significant effect on flame evolution, and the behavior of PVC in isothermal flow is different than that in reacting flow [3, 8, 10, 11]. The amplitude of PVC is higher in isothermal flow case than that in reacting flow, while its frequency is higher in reacting flow case. The causes of PVC suppression in reacting flow are related to volume dilatation and higher viscosity. Several passive methods for PVC suppression were proposed in the literature. For instance, it was reported that PVC is suppressed when a multi-annular swirl burner is used [12]. The mode of fuel entry, axial or tangential, can significantly influence PVC suppression [3]. Equivalence ratio plays an important role in PVC suppression, where equivalence ratios ranging between 0.5 - 0.75 were found to suppress it [3]. Moreover, the location of flame front determines whether PVC is excited or suppressed; where, for example, PVC is excited when flame front moves into the outer high velocity region [3]. Incomplete fuel-air mixing results in equivalence ratio fluctuations, which is one of the causes of combustion instabilities. In addition, incomplete mixing limits flame stable operating conditions and increases  $\text{NO}_x$  emissions [13]. On the other hand, while improved fuel-air mixing is achieved using long mixing lengths [8], it causes

combustion instability such as flashback and auto-ignition. Galley et al. [7] employed axial fuel injection and suggested the use of a co-swirl or counter-swirl arrangement or a multi-point fuel injection to enhance mixing within a certain mixing length [8]. Despite that, the presence of PVC itself was found to enhance mixing downstream of the mixing tube exit [7]. Although reducing the mixing length is useful to mitigate combustion instabilities in some burner configurations [14],  $\text{NO}_x$  emissions remain an issue.

Kalt et al. [15] found that discharging fuel jet centrally significantly alters flame stability. Similarly, our previous work [16] showed that a change in the central fuel nozzle geometry alters coherent structures and flashback behavior inside the mixing tube. That is, changing the number of orifices in axisymmetric bluff body nozzle and their arrangement significantly influence the coherent structures' amplitude and flashback inside a relatively long mixing tube. However, central fuel nozzles with large bluff solid area while using a relatively long mixing tube are found to induce flashback and increase the propensity for the vortex shedding occurrence. Employing strong axial air injection from a central concentric nozzle was found responsible for converting the vortex breakdown from bubble to cone type and, hence, suppressing PVC [17]. Furthermore, fuel nozzle geometry affects some features of turbulent flowfield; such as entrainment, spreading rate, and decay rate [18,19].

The literature reviewed above indicated that the control of the mixing level control inside a mixing tube is a key parameter for both combustion instabilities and flashback propensity of PPFs. For instance, using a relatively short mixing tube to reduce flashback propensity adversely affects the mixing and consequently combustion stability. On the other hand, long mixing tubes improve mixing but at the same time promote flashback. To overcome this issue, some strategies have been reported in the literature. For example, the use of multiple swirl generators was found

to enhance mixing, promote PVC suppression and consequently improve flame stability [8, 12]. Also, a recent study [16] by the present authors employed a different strategy which involved the use of a variety of fuel nozzle geometries, where their effects on coherent structures (PVC and vortex shedding) have been examined under PPFs flashback conditions using a long mixing tube. The present study continues to use this strategy of altering the geometry of fuel nozzle geometries with aim to improve the mixedness inside the mixing tube, while at the same time uses a relatively short mixing tube to avoid flashback. In particular, the present paper uses a relatively short mixing tube to experimentally examine the effect of different geometries of the central fuel nozzle on the ensuing flowfield characteristics, coherent structures' suppression and their impact on a swirling partially premixed methane flame.

### **3.3. Experimental setup**

#### *3.3.1. Burner configuration and test conditions.*

The burner, schematically shown in Fig. 3.1, consists of an interchangeable central nozzle surrounded by an annulus through which swirling airflow discharges into a short mixing tube, which has an inner diameter ( $D$ ) of 24 mm. The swirl generator (Fig. 3.1a) has a vane angle ( $\alpha$ ) of  $60^\circ$  which corresponds to a swirl number ( $S$ ) of 1.15. Rich premixed methane-air mixture is injected through the central nozzle which then mixes with the swirling air downstream of the central nozzle into the mixing tube. The purpose of injecting rich premixed mixture from the central nozzle rather than pure methane, in the present configuration, is to eliminate flame propagation into the mixing tube. The mixing length ( $L_m$ ), which is defined here as the distance between the tip of the central nozzle and the mixing tube exit, is 35.2 mm, and  $L_m/D$  represents the degree of partial premixing [20]. The mixture is considered as premixed when using long mixing



length ( $L_m$ ), non premixed when using  $L_m = 0$ . In the present study, a  $L_m/D \approx 1.5$  is employed. The four central nozzles used in this study are tapered-type and have a similar equivalent diameter ( $D_e$ ) of 3 mm and an orifice length to orifice diameter ratio ( $l/d_o$ ) of 5.5, where  $l$  is the depth of the orifice and  $d_o$  is the diameter of a single orifice, as shown in Fig. 3.1b. The central nozzles are categorized into two groups, namely; single-orifice nozzles (N1 and N2) and multi-orifice nozzles (N3 and N4). The main differences between these nozzles are the bluff solid area (solid area of the nozzle tip) and the number of orifices. For example, nozzle 1 (N1) has a smaller bluff solid area than that of N2, N3 and N4. N3 and N4 have, respectively, three and four radially equally distributed orifices, while having the same bluff solid area. Our earlier study [16] showed that both, multi- or single-orifice, nozzles with relatively large bluff solid area along with a long mixing tube exhibited the highest flashback propensity. Consequently, the objective from using here tapered nozzles is to decrease the bluff solid area and hence minimize instabilities resulting from the presence of a relatively large bluff body in the direction of the flow, especially when using a short mixing length. The central nozzle flow rate is kept constant at 30 LPM (30 LPM air for isothermal flow, and 20 LPM fuel and 10 LPM air for reacting flow tests). The swirling airflow rate is kept constant at 320 LPM. The mean bulk flow velocity calculated at this flow rate is 12.89 m/s which corresponds to Reynolds number ( $Re_D$  based on the inner diameter of the mixing tube,  $D$ ) of  $19 \times 10^3$ . The momentum flux ratio, which is the ratio between the flow momentum from the central nozzle to that of the swirling airflow, is 0.27. The flow rates of the swirling air and central nozzle produce a mixture with an equivalence ratio of 0.58 and a power of 11.75 kW. This equivalence ratio was chosen such that it lies within the range at which PVC suppression is expected (i.e., 0.5 – 0.75). Three flow meters are used to deliver the fuel and air; Brooks SLA5853 for swirling airflow, and two Matheson FM-1050 flow meters for the central air and fuel mixture.

The uncertainty in the equivalence ratio is estimated to be  $\pm\sqrt{3}$  based on the root-sum-square (RSS) of the accuracy of the flow meters ( $\pm 1\%$  each). In order to capture the flowfield inside the mixing tube, a 2-mm thickness fused silica quartz is used to facilitate optical access.

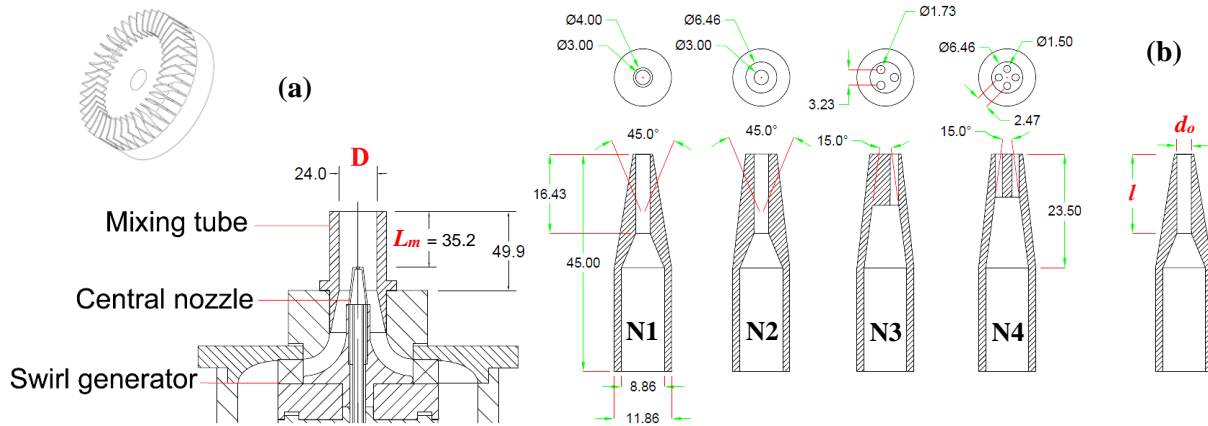


**Fig. 3.1.** Schematic diagram of (a) the burner setup with swirl generator, and (b) different central nozzle geometries (all dimensions in mm and all angles in deg).

### 3.3.2. Measuring techniques

#### 3.3.2.1. Particle image velocimetry (PIV)

It was used to document the flowfield and the dominant coherent structures of isothermal flows inside the mixing tube, as well as isothermal and reacting flows downstream of the mixing tube exit. A laser sheet thickness of 1 mm was emitted from a Nd:Yag laser of a maximum pulse energy of 135 mJ and a repetition rate of 10 Hz. The image pairs were captured using a double-frame FlowSense EO 4M CCD camera with a resolution of  $2048 \times 2048$  pixel<sup>2</sup>. For isothermal flow measurements downstream of the mixing tube, the swirling air was seeded with incense particles (with a mean size of approximately 1  $\mu\text{m}$ ). For reacting flow measurements,  $\text{TiO}_2$  seeding particles were injected into the swirling air stream due to their durability at high temperature. Approximately 1000 pairs of images were captured for both isothermal and reacting flow cases.

The field of view (FOV) was  $83 \times 83 \text{ mm}^2$  which corresponds to a resolution of  $0.0405 \text{ mm/pixel}$ . The maximum particle image size was found to be 3 pixels. Proper orthogonal decomposition (POD) analysis was used to detect coherent structures from using the original raw images, and afterward the raw images were cropped into  $622 \times 998 \text{ pixel}^2$  ( $25.2 \times 40.4 \text{ mm}^2$ ) which is the area/zone where coherent structures are dominant. This procedure was found very useful for eliminating random fluctuations [21]. For measurements inside the mixing tube, the field of view was  $425 \times 944 \text{ pixel}^2$  ( $21.5 \times 49 \text{ mm}^2$ ) which corresponds to a resolution of  $0.052 \text{ mm/pixel}$ . A protected silver 2-inch square mirror was positioned at  $45^\circ$  in order to reflect the laser sheet at a vertical direction into the quartz mixing tube (see Fig. 3.2a). It should be noted that the presence of curved wall necessitated performing an image dewarping following the procedure reported in [16]. For PIV measurements in the horizontal/radial plane, the laser sheet was placed parallel to the plane of the mixing tube exit at an upstream axial distance of 24 mm, with the camera aimed onto a  $45^\circ$  mirror in order to capture the flowfield images, as depicted in Fig. 3.2b. An interrogation area of  $32 \times 32 \text{ pixel}^2$  with an overlap of 50% with a median filter and range validation were used to process the captured images. A detailed description of error analysis was reported in [16]. The different sources of errors that affect the instantaneous velocity include displacement systematic error, truncation and measurement errors, interpolation error, and image processing uncertainty, which were found to be less than  $0.01 \text{ pixel}$ ,  $\pm 1\%$ ,  $\pm 1\%$ , and  $\pm 1\%$ , respectively. The estimated total uncertainty in the mean velocity was found  $\pm 0.4 \text{ m/s}$ , and the uncertainty in the RMS, which was estimated based on the Chi-square distribution, was found within  $\pm 4\%$ .

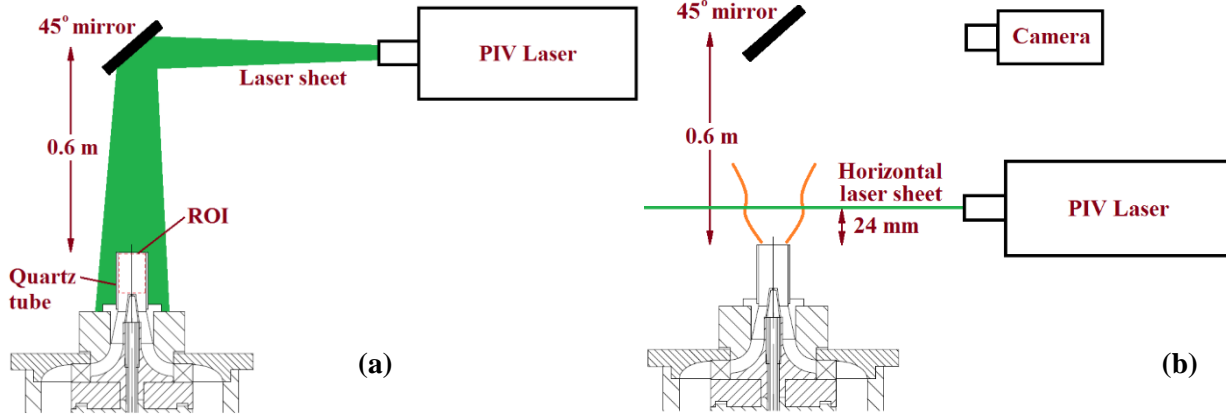


**Fig. 3.2.** Schematic of the experimental setup of PIV measurements in the (a) axial direction inside the mixing tube, and (b) radial direction downstream of the mixing tube exit.

### 3.3.2.2. Quantitative light sheet

This technique is used for normalized density field measurements as a representative for the mixing field. The major advantage of using QLS is its simplicity compared to other techniques such as Rayleigh scattering which requires signal filtering. Moreover, QLS can be conducted using PIV setup allowing simultaneous measurement of the velocity field and normalized density field. It should be highlighted that this technique is relative since reference value is needed to obtain an absolute value. Consequently, the results obtained from this technique are only used for comparison between the different test cases. A total of 1000 single-frame images were acquired for this investigation. Using this technique, the reacting flow is seeded with  $\text{TiO}_2$  where the particle density distribution ( $C$ ) is assumed proportional to the fluid density ( $\rho$ ). The procedure, which is well documented in the literature [22–25], is briefly described here. The image intensity ( $I$ ) depends on factors such as particles density distribution ( $C$ ), local light sheet intensity ( $I_l$ ), reflections ( $R_q$ ) from the quartz tube (if used), dark current of the camera ( $D_{cc}$ ), a factor ( $V_a$ ) for different viewing angles in the laser sheet plane, probe volume, scattering cross-section, solid

angle, camera quantum efficiency, and transmissivity of the optical system. The acquired image intensity is described as:

$$I(x, y) = C(x, y)I_l(x, y)V_a(x, y) + R_q(x, y) + D_{cc}(x, y) \quad (1)$$

Each instantaneous image in the reacting flow case is corrected for the dark current by subtracting an image without seeding particles. Furthermore, for correcting the factor resulting from the different viewing angles and local light sheet intensity, an image with homogeneous particles density distribution is used. The intensity of the image of the dark current correction is described as

$$I_o(x, y) = R_q(x, y) + D_{cc}(x, y) \quad (2)$$

and the estimated intensity of the homogeneous particles density image is given as

$$I_h(x, y) = C_h I_l(x, y) V_a(x, y) + R_q(x, y) + D_{cc}(x, y) \quad (3)$$

Figures 3.3a,b and c show images that represent  $I(x, y)$ ,  $I_o(x, y)$ , and  $I_h(x, y)$ , respectively. The normalized intensity of the images is correlated to the normalized particle density distribution and normalized flow density (see Fig. 3.3e) as follows:

$$\text{mean} \left( \frac{I(x,y) - I_o}{I_h(x,y) - I_o} \right) = \text{mean} \left( \frac{C(x,y)}{C_h} \right) = \text{mean} \left( \frac{\rho(x,y)}{\rho_h} \right) = \Omega \quad (4)$$

It should be noted that the effect of multi-scattering and background illumination resulting from the scattered light off the seeding particles are assumed negligible [23]-[24]. Furthermore, it is assumed that the particle density is not affected by the velocity field and that the scattering cross section is not altered within the laser sheet plane. The use of TiO<sub>2</sub> of a diameter of 1 μm guarantees that the particles' size distribution is not affected by the high temperature owing to the fact that the melting temperature of TiO<sub>2</sub> is higher than the adiabatic flame temperature. Note that the estimated Stokes number ranges between 0.007 and 0.009 which is much smaller than the threshold limit (i.e.,  $Sk \approx 0.1$ ), and hence the seeding particles are assumed to follow faithfully

the flow [26]. The measurement error pertaining to the QLS technique was found to be approximately 5% based on the method of Voigt et al. [27] and Roehle et al. [28]. The maximum statistical error of the mean intensity measurements is estimated to be  $\pm 3\%$  based on the t-student distribution and the RMS of the intensity.

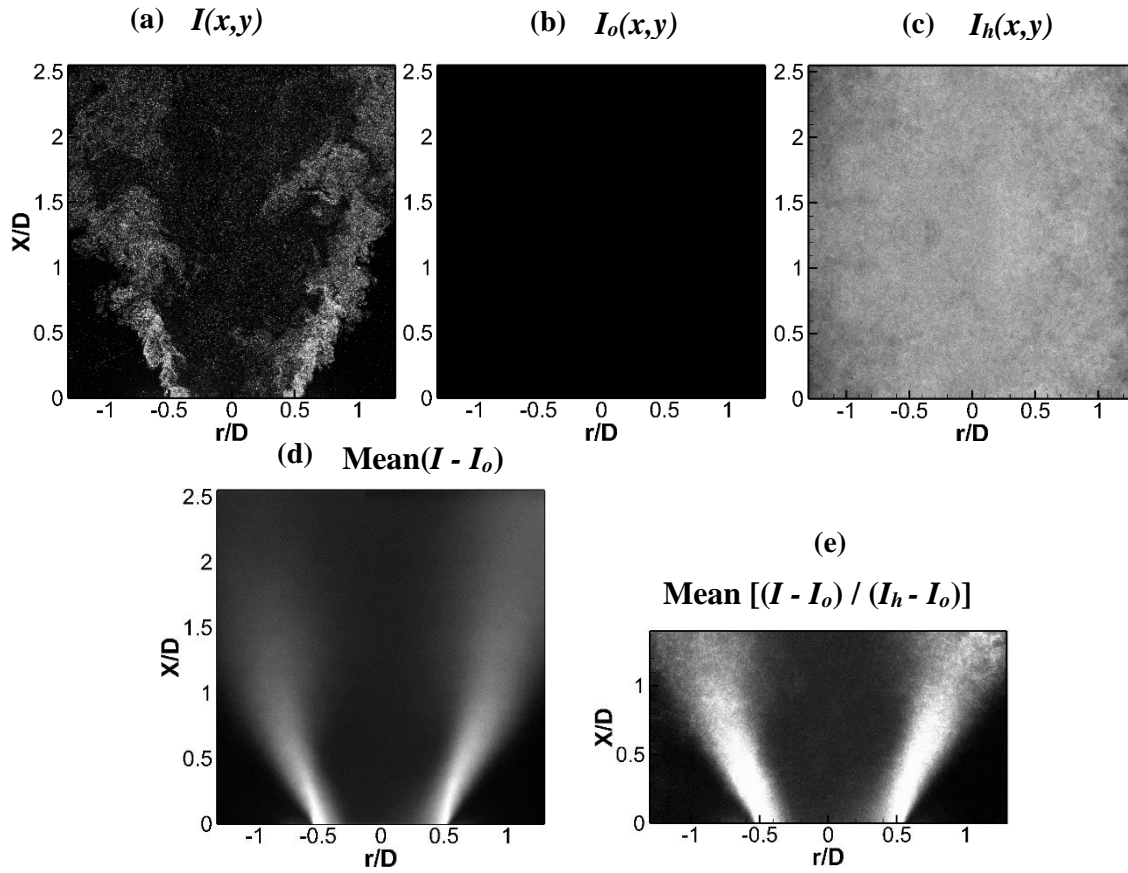


**Fig. 3.3.** Procedure for obtaining the normalized flow density fields.

### 3.3.2.3. Laser Doppler velocimetry (LDV)

Since the repetition rate of the PIV used in the present study does not exceed 10 Hz, a 2D TSI laser Doppler velocimetry (LDV) was used to capture the time-resolved dynamics of coherent structures. Specifically, LDV was used to determine the power spectra of the axial velocity fluctuations at a single location where measurements were conducted at a normalized radial

distance  $r/D = 0.6$  and a normalized axial distance  $X/D = 1$  in order to capture the PVC frequency. The LDV setup consists of a 5 W Coherent Innova 70c Ar-ion laser, a fiber light FBL-3 multicolor beam separator, a TSI TR 260 fiberoptic equipped with TLN06-350 lens, a PDM 1000 photo detector module, and a FSA 4000 Doppler burst correlator. More details are given in [16].  $\text{TiO}_2$  of 1  $\mu\text{m}$  mean diameter was used as seeding particles. A total of 150,000 data at a sampling rate of approximately 12 kHz were acquired. Hampel filter was applied on the raw data to remove the outliers while Savitzky-Golay filter of 3<sup>rd</sup> order and segment length of 9 was applied to smooth the raw data. The normalized (relative) uncertainty of the measurements of the instantaneous velocity was found  $\pm 0.005$ , and the total error in the LDV velocity was less than 0.2 m/s.

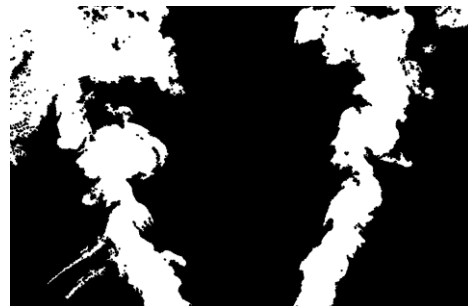
#### 3.3.2.4. *Mie scattering technique*

This technique was used in numerous studies to capture flame front position of swirling [29] and V-shaped flames [30] and has the advantage of being simple since the same PIV system can be used. Olive oil seeding particles of a mean diameter of 1  $\mu\text{m}$  were used to detect the local flame surface based on the assumption that combustion occurs in a relatively thin layer [30, 31]. The olive oil particles can be visualized in the reactants regions while they disappear in the products region since they evaporate at approximately 650 K [32]. Although turbulent flames are three-dimensional in nature, the results of two-dimensional measurements are assumed adequate [29]. The laser sheet thickness was adjusted as  $350 \pm 50 \mu\text{m}$ , and the FOV was  $62 \times 62 \text{ mm}^2$  which results in a resolution of 30  $\mu\text{m}/\text{pixel}$ . A total of 1000 single-frame images were captured at 10 Hz. The procedure of image processing is shown in Fig. 3.4 (detailed procedure can be found elsewhere [31]). The histogram of the raw images was adjusted to enhance the contrast of images. The contrast-enhanced images were then binarized based on a threshold of 25% of the mean unburned

intensity. This threshold was selected based on a proper capture of the flame front as compared to the higher and lower threshold values over all the range of images. The generated noise due to the binarization process was removed using a median filter of a window size of  $3 \times 3$ . The edges of the flame were detected using a Sobel operator. Finally, the flame region (indicated by the white zone in Fig. 3.4d) was extracted from the image and further calculations of the mean and RMS flame front positions and mean progress variable (c) were carried out. Differentiating between seeding particles' voids due to ambient air entrainment (e.g., pocket referred to by the magnified zone on the left side of Fig.3.4c) and flame pockets (e.g., pockets referred to by the arrows in Fig.3.4c,d) in the reactants zone (since both of them result in regions with no seeding particles) was performed based on the criteria of voids' size and its vicinity to the flame. Image resolution, binarization threshold, noise removal filter, laser sheet thickness, and edge detection operator were found to contribute to the uncertainty in the estimation of flame front position [16]. The maximum uncertainty from image resolution was  $\pm 0.1$  mm. The maximum uncertainty from image processing (including the binarization threshold filter size, and edge detection operator type) was found to be less than  $\pm 2\%$ . The bias error in the estimation of flame front positions due to the laser sheet thickness is less than  $\pm 1\%$ . The total error of flame front positions was found to be within  $\pm 5\%$  based on the student's t-distribution and maximum RMS.



(a)



(b)



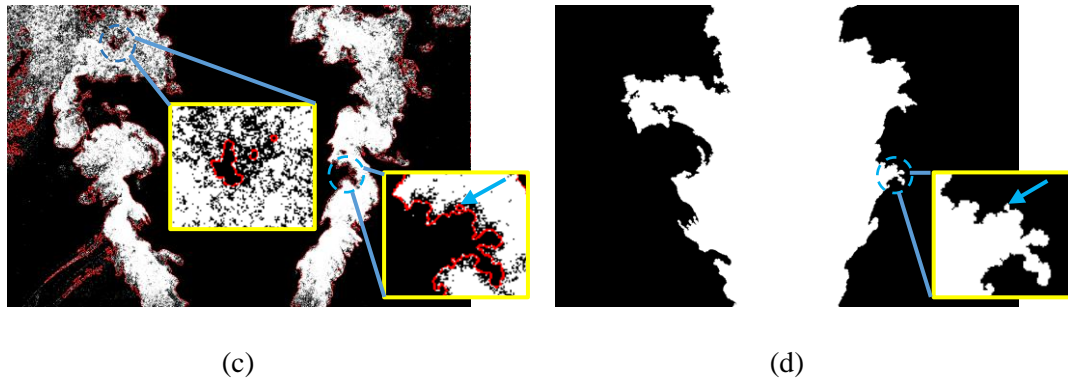


**Fig. 3.4.** Procedure of flame edge detection where (a) binarized image, (b) filtered image, (c) edge-detected image, and (d) extracted flame image. The squares in (c) and (d) are a magnification of typical voids of seeding particles.

### 3.4. Results

This section is divided into three subsections. In the first subsection, the mean flowfields, centerline axial mean velocity, and centerline total turbulence intensity are presented for different central nozzles and both isothermal (inside and downstream of the mixing tube exit) and reacting flows (only downstream of the mixing tube exit). The second subsection presents the effect of the central nozzle geometry on coherent structures for both isothermal (inside and downstream of the mixing tube exit) and reacting flow cases (downstream of the mixing tube exit). Finally, the third subsection focuses on the effect of nozzle geometry on flame front dynamics.

#### 3.4.1. Mean flow characteristics

##### 3.4.1.1. Inside the mixing tube

Measurements in the mixing tube are conducted to capture the upstream (i.e., upstream of the flame) mean flow characteristics and coherent structures for different central fuel nozzle geometries. Profiles of the normalized centerline axial mean velocity and the corresponding axial turbulence intensity inside the mixing tube for the isothermal flow case are presented in Fig. 3.5a,b

(note that, for the velocity profiles in this figure and also in Fig. 3.7, the frequency of the experimental data is reduced to make the comparison legible). The centerline axial mean velocity ( $V_{CL}$ ) is normalized by the mean bulk flow velocity ( $V_j$  at the mixing tube exit), and the axial distance along the mixing tube ( $s$ ) is normalized by the mixing tube inner diameter ( $D$ ), where  $s$  varies from 0 to  $L_m$  ( $L_m$  is the mixing length). The normalized centerline axial turbulence intensity is calculated by dividing the centerline RMS of the axial velocity fluctuations ( $v'$ ) by the corresponding local centerline axial mean velocity. The results in Fig. 3.5a show that, for  $s/D = 0.5$ , single-orifice nozzles (N1 and N2) exhibit a higher normalized mean axial velocity along the centerline compared to multi-orifice nozzles (N3 and N4). However, farther downstream at  $s/D > 0.85$ , the trend is reversed where those of multi-orifice nozzles exhibit a tendency of plateau that has higher normalized mean axial velocity than single-orifice nozzles. This implies that single-orifice nozzles promote faster decay rate along the centerline than multi-orifice nozzles (Fig. 3.5d), which is an indication of their capability of enhancing the mixing in the central region ( $\sim -0.2 < r/D < 0.2$ ) [19] as discussed later. Moreover, jet flow issuing from N2 decays faster than that of N1, as a result of its higher bluff solid area. The profiles of the centerline axial turbulence intensity in Fig. 3.5b show a significant increase with single-orifice nozzles compared to multi-orifice nozzles. The higher turbulence intensity of single-orifice nozzles is attributed to the higher shear between the central flow and the swirling airflow which results in a higher decay rate. The results reveal that the upstream flowfield inside the mixing tube of the isothermal flow shows a similarity with that of the reacting flow since this flow region is less affected by heat release. This can be observed by the isothermal flow in Fig. 3.5b with the reacting flow in Fig. 3.5c. Similar finding was found in [33], where some results near the burner exit of isothermal flow were used to represent the reacting flow [34].

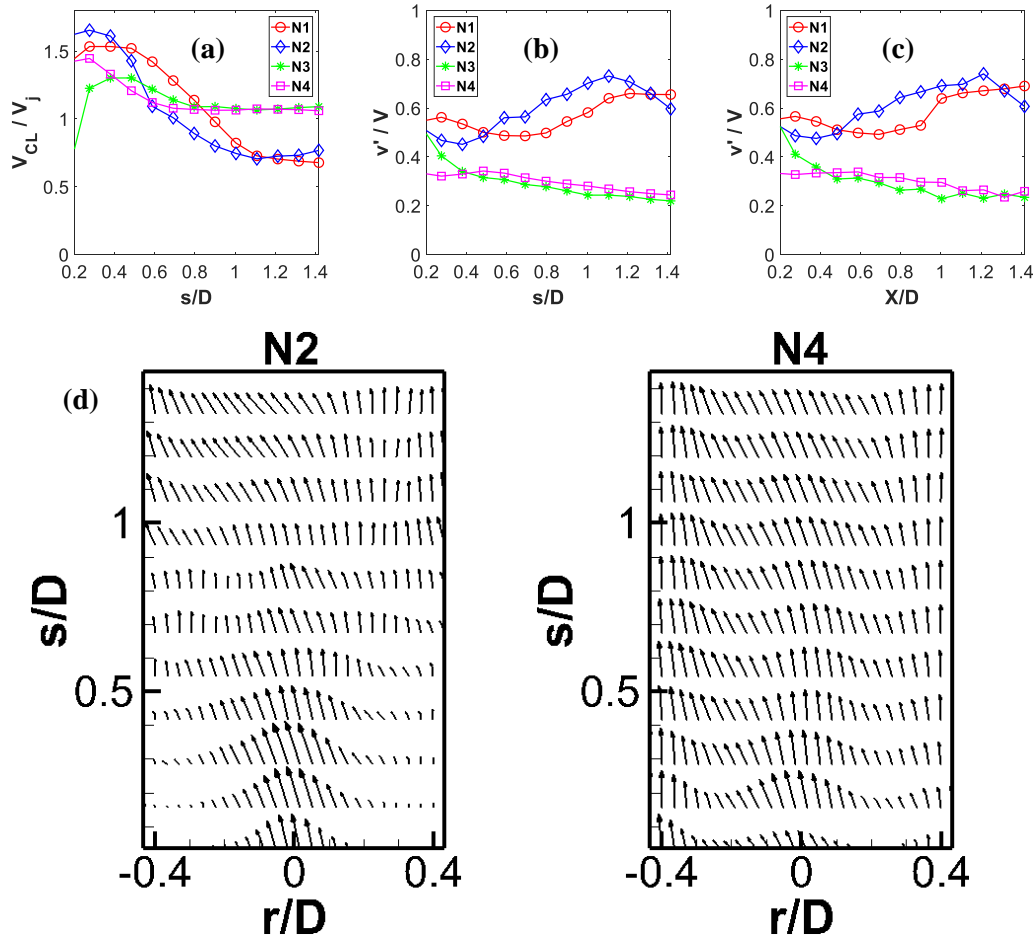


**Fig. 3.5.** Normalized profiles of the centerline axial (a) mean velocity and (b) turbulence intensity of the isothermal flow, and (c) turbulence intensity of the reacting flow case for different central fuel nozzle geometries inside the mixing tube, and (d) the mean axial velocity vector field for N2 and N4 inside the mixing tube.

Figure 3.6 presents the contours of the axial turbulence intensity in the mixing tube (note that the mixing tube exit is at  $s/D = 1.46$ ). The results show that single-orifice nozzles exhibit higher axial turbulence intensity along the centerline than multi-orifice nozzles. In addition, the peak values occur in the central region for single-orifice nozzles, whereas they are radially shifted from the centerline for multi-orifice nozzles. These findings corroborate those presented in Fig. 3.5. To emphasize on the effect of the central nozzle geometry, the integral length scale,  $\Lambda_L$  (see Table 1), was calculated inside the mixing tube at  $s/D = 0.1$  by integrating the autocorrelation

function of the centerline axial velocity fluctuations [35, 36]. The results show that single-orifice nozzles have the ability to produce larger eddies than multi-orifice nozzles, which implies more rapid development of the mixing layer [37].

In summary, the results presented above revealed a distinct difference in the flowfield characteristics between the single and multi-orifice nozzle. This is a clear indication that the central fuel nozzle geometry alters the turbulent flowfield upstream of the mixing tube exit and consequently the mixing characteristics inside the mixing tube. This, in turn, is expected to affect flame dynamics downstream of the mixing tube exit as discussed below.

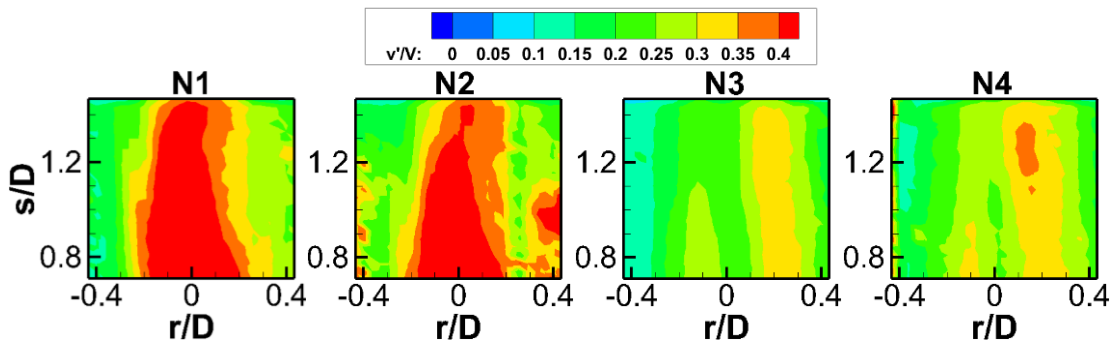


**Fig. 3.6.** Contours of the axial turbulence intensity in the mixing tube for different central nozzle geometries.

**Table 3.1.** Integral length scale in the mixing tube for the different central fuel nozzle geometries.

	N1	N2	N3	N4
$\Lambda_L$ (mm)	6.14	6.77	3.95	4.88

#### 3.4.1.2. Downstream of the mixing tube exit

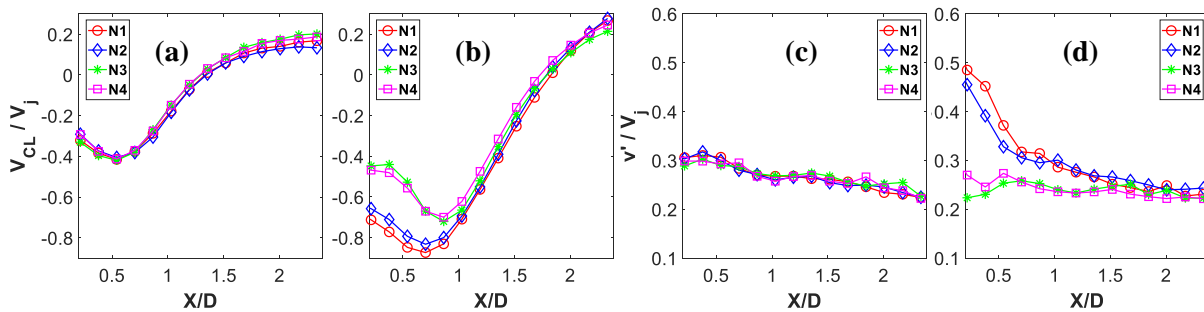
The normalized centerline axial mean velocity and its corresponding centerline axial turbulence intensity for different central nozzle geometries are shown in Fig. 3.7. The centerline axial mean velocity ( $V_{CL}$ ) is normalized by the mean bulk flow velocity ( $V_j$ ), and the axial distance downstream of the mixing tube exit ( $X$ ) is normalized by the inner diameter of the mixing tube

(D), where  $X/D = 0$  is the mixing tube exit plane. The results in Fig. 3.7a show that the profile of the normalized centerline axial mean velocity is approximately similar for all nozzles in the absence of flame (isothermal flow). The reversal flow due to the presence of a central recirculation zone (CRZ) results in a peak of negative velocity at  $X/D \approx 0.6$  (Fig. 3.7a,b). While the normalized mean axial velocity reaches a plateau at  $X/D > 1.9$  in the case of isothermal flow (Fig. 3.7a), it continues increasing steadily in the corresponding reacting flow case (Fig. 3.7b). In addition, in the reacting flow cases, N1 and N2 exhibit the highest peak negative centerline mean velocity at  $X/D \approx 0.6$ , whereas N3 and N4 exhibit the lowest peak at  $X/D \approx 0.7$  (Fig. 3.7b). Furthermore, in the reacting flow, the increase in velocity is steeper and the peak negative velocity for all nozzles is higher than their counterparts' isothermal flow cases. The similarity in the velocity profiles between the different nozzles in the isothermal flow case is an indication that the central nozzle's flow does not have influence on the behavior of the CRZ formed downstream of the mixing tube exit. However, in the reacting flow case, the difference in the upstream axial turbulence intensity causes a significant change in the CRZ behavior downstream of the mixing tube exit. It should be noted that the purpose of comparing the mean flowfield between the isothermal and reacting flow is to isolate the effect of turbulent field from that caused by combustion.

The profiles of the centerline axial turbulence intensity of the isothermal flow cases, which exhibit a slow gradual decrease with increasing  $X/D$ , are similar for all nozzles (see Fig. 3.7c). However, in contrast to the isothermal flow case, the profiles of the centerline axial turbulence intensity in the presence of heat release (flame) depends on nozzle geometry (Fig. 3.7d). N1 shows the highest centerline axial turbulence intensity for  $X/D < 1$ , followed by N2. The profiles of both N1 and N2 (i.e., single-orifice) nozzles exhibit a sharp decrease for  $X/D < 0.7$  followed by a gradual decrease. However, the profiles of N3 and N4 (multi-orifice) nozzles follow approximately

a plateau (i.e., nearly constant). The relationship of the profiles of the centerline axial turbulence intensity with nozzles geometry is less discernable at  $X/D > 1.5$ . It can be concluded that, for  $X/D < 1.5$ , there is a difference in the axial profiles of the centerline axial turbulence intensity between the different nozzles which indicates an apparent difference in the mixing rates in the early region downstream of the mixing tube exit, and thus its dependence on the nozzle geometry. The mean axial velocity ( $V$ ) contours of N3, as an example, for both isothermal and their corresponding reacting flow cases, are shown in Fig. 3.7e and f. For all nozzles, these results show the occurrence of vortex breakdown which is indicated by the central region of reversal flow due to the presence of CRZ.

In summary, the results presented above revealed dependence of the characteristics of the turbulent flowfield downstream of the mixing tube exit on nozzle geometry only in the reacting flow case. This implies different mixing characteristics upstream of the mixing tube exit between the single-orifice and multi-orifice nozzles, and hence causes a difference in the CRZ downstream of the mixing tube exit. This consequently causes different coherent structures' behavior downstream of the mixing tube exit depending on the nozzle geometry, as discussed below.



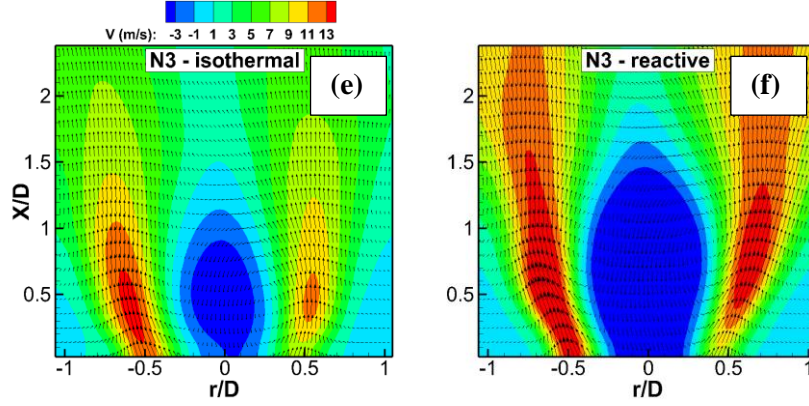


**Fig. 3.7.** Profiles of the normalized mean axial velocity for different nozzles of the (a) isothermal and (b) reacting flow cases, the corresponding axial profiles of the normalized axial RMS velocity of the (c) isothermal and (d) reacting flow cases, and contours of the mean flowfield for N3 of the (e) isothermal and (f) reacting flow.

### 3.4.2. POD of the velocity field

POD was used to capture coherent structures in the flowfield, and details about the procedure/methodology is reported elsewhere [16]. According to the work of Epps and Techet [38], not all the captured mode shapes represent coherent structures in the flowfield. Epps and Techet [38] proposed a criterion to validate the captured POD modes based on a threshold modal energy; where the modes with higher energy than the threshold are to be considered, the remaining modes are contaminated by the measurement noise. The expression of the threshold modal energy is  $\lambda_{th} = MN\varepsilon^2$ ; where  $\lambda_{th}$  is threshold modal energy,  $M$  is the total number of velocity vectors in both axial and radial direction in each image,  $N$  is the number of acquired images, and  $\varepsilon$  is the RMS error in estimating PIV velocity data (m/s). The value of  $\varepsilon$  is estimated based on a correlation peak estimation error of 0.1 pixel [39]; where  $\varepsilon \approx 0.037$  m/s for measurements inside the mixing tube and  $\varepsilon \approx 0.031$  m/s for measurements outside the mixing tube. Based on  $M = 1475$  and 2457 vectors in the field of view for measurements inside and outside the mixing tube, respectively, the corresponding value of  $\lambda_{th} \approx 1987$  and  $2361$  m<sup>2</sup>/s<sup>2</sup>.

### 3.4.2.1. Inside the mixing tube

POD analysis inside the mixing tube was performed in order to provide insight into the effect of the central nozzle geometry on the upstream coherent structures which can be convected downstream in the mean flow direction. The results show a significant difference in the modal energy between single-orifice and multi-orifice nozzles (Fig. 3.8a). By looking at the modal energy of single-orifice nozzles, it clearly shows that the larger bluff solid area of N2 increases slightly the energy of coherent structures compared to N1. Also, these results indicate that the number of orifices in the multi-orifice nozzles slightly alters the presence of coherent structures. It should be noted that based on the value of the threshold modal energy ( $\lambda_{th} \approx 1987 \text{ m}^2/\text{s}^2$ ), only the first three modes for single-orifice nozzles are considered whereas none of the multi-orifice nozzles' POD modes are considered as coherent structures since they are lower than the threshold value. The summation of the first four POD modes shows a clear difference between the modal energy of single-orifice nozzles and that of multi-orifice nozzles (Fig. 3.8b).

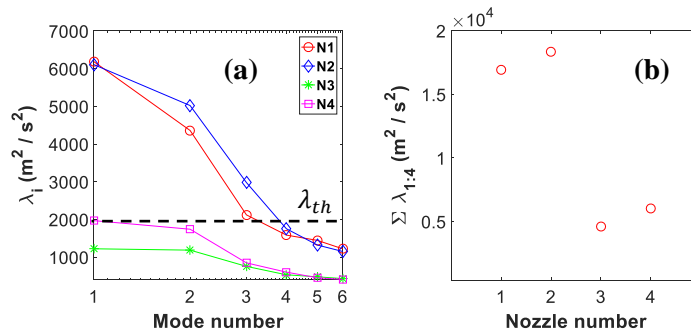


**Fig. 3.8.** (a) POD modal energy of the first six modes for different nozzles inside the mixing tube (dashed black line indicates the threshold modal energy), and (b) POD modal energy of the summation of the first four modes for the different central fuel nozzle geometries inside the mixing tube.

Phase averaging of the linear superposition of the first pair of POD modes is determined in order to shed light on the formation and convection of coherent structures inside the mixing tube



(i.e., upstream of the flame). The contribution of the first mode pair to the total turbulent kinetic energy for different central nozzles is listed in Table 2. The POD time coefficients are used to determine the phase angles of the instantaneous reconstructed velocity fields of the linear superposition of the first two POD modes [16]. The averaging was determined for eight phase angles ( $45^\circ$ ,  $90^\circ$ ,  $135^\circ$ ,  $180^\circ$ ,  $225^\circ$ ,  $270^\circ$ ,  $315^\circ$ ,  $360^\circ$ ). The results show that the vortex core seems to precess around the mixing tube axis which is often suppressed due to combustion downstream of the mixing tube exit as discussed later. It can be seen that the flow of single-orifice nozzles is characterized by strong elongated vortical structures (Fig. 3.9). The higher energy of coherent structures of single-orifice nozzles, as compared to that of multi-orifice nozzles, explains why the single-orifice nozzles centerline axial turbulence intensity is higher than that of multi-orifice nozzles (Fig. 3.5b). In conclusion, in contrast to multi-orifice nozzles, single-orifice nozzles promote coherent structures, which affect the turbulent flowfield characteristics, such as increasing the integral length scale. This, in turn, affects the mixing in the central region as witnessed by higher turbulence intensity (Fig. 3.6).

**Table 3.2.** Energy fraction of the summation of the first two modes in the mixing tube for the different central fuel nozzle geometries.

	N1	N2	N3	N4
$\frac{\sum \lambda_{1:2}}{E_{tot}}$	21.75%	24.85%	9.1%	13.55%

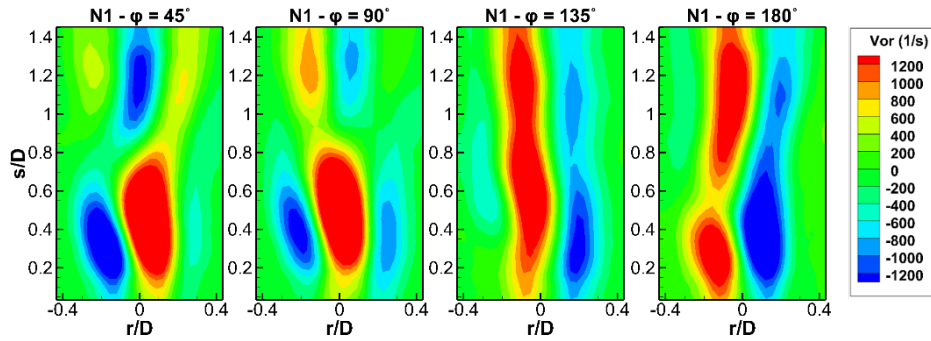


**Fig. 3.9.** Vorticity fields of the phase-averaged linear superposition of the first two POD modes at different phase angles in the mixing tube for N1.

### 3.4.2.2. Downstream of the mixing tube exit

POD of the velocity fields for different nozzles of both isothermal and reacting flow cases is used in order to capture coherent structures. Note that combustion usually reduces coherent structures' amplitude, and therefore, an investigation whether this reduction is attributed to the presence of chemical reactions (combustion) or the nozzle geometry is necessary. The first four eigenvalues ( $\lambda_i$ ) for different central nozzles of the isothermal and reacting flow cases are presented in Fig. 3.10a and 10b, respectively. It should be noted that based on the threshold modal energy ( $\lambda_{th} \approx 2361 \text{ m}^2/\text{s}^2$ ), the first four POD modes exceed this threshold value which confirms the validity of these POD modes. The results show approximately similar profiles in the case of the isothermal flow for higher order modes ( $\lambda_{i>2}$ ), whereas the first two modes exhibit a slight difference. However, in the reacting flow case, the difference in the modal energy of the first four modes between different nozzles is more discernable (Fig. 3.10b). In contrast to the isothermal flow case, a significant reduction in the first four modes energy is observed in the case of reacting flow. This indicates that, contrary to the isothermal flow case, heat release has an adverse effect on the energy of coherent structures. It can be seen in Fig. 3.10c that the modal energy of the summation of the first four POD modes of single-orifice nozzles is significantly higher than that

of multi-orifice nozzles. The contribution of the first four modes to the total kinetic energy listed in Table 3 for both isothermal and reacting flow cases. Despite the fact that coherent structures' amplitude decreases in the presence of combustion, the central nozzle further contributes to coherent structures' suppression. That is, there is a further reduction in coherent structures' amplitude with multi-orifice nozzles as compared to that of single-orifice nozzles, which indicates the dependence of coherent structures' suppression on the central nozzle geometry. Further investigation on whether PVC experiences a suppression or a reduction in its amplitude in the reactive flow case is discussed later.

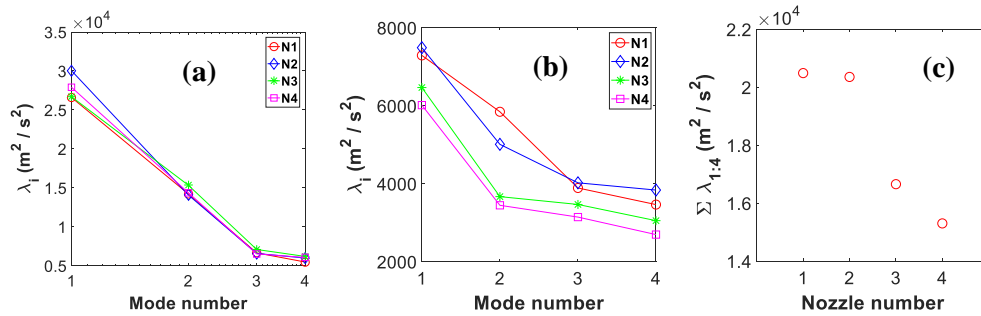


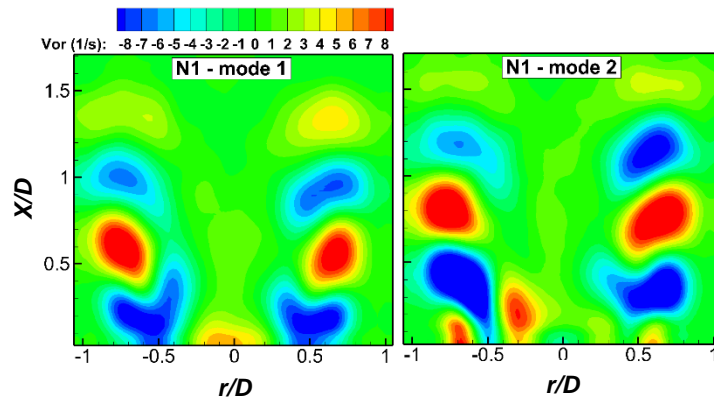
**Fig. 3.10.** POD modal energy of the first four modes for the different central fuel nozzle geometries in the (a) isothermal and (b) reacting flow cases, and (c) POD modal energy of the summation of the first four modes in the case of reacting flow for the different central fuel nozzle geometries.

**Table 3.3.** Energy fraction of the summation of the first four modes for the isothermal flow case (first row) and reacting flow case (second row) for different central fuel nozzle geometries.

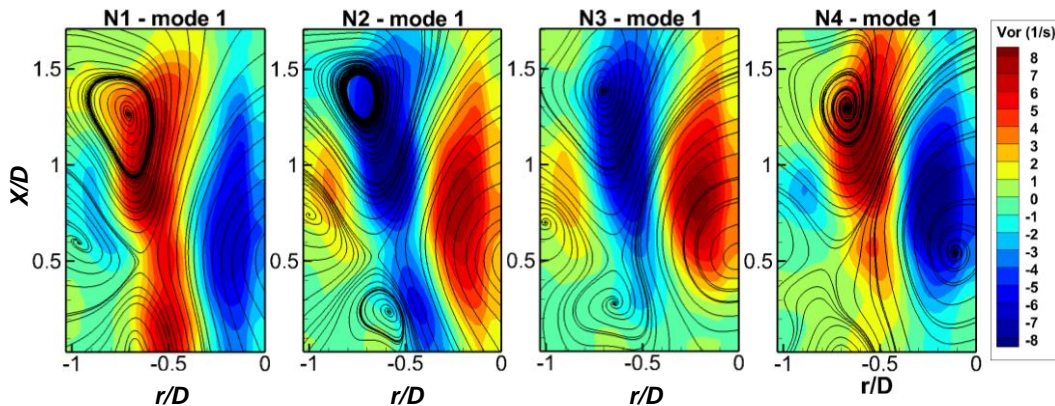
	N1	N2	N3	N4
$\frac{\sum \lambda_{1:4}}{E_{tot}}$	28.91%	28.89%	29.69%	29.07%
$\frac{\sum \lambda_{1:4}}{E_{tot}}$	30.62%	29.94%	30.72%	28.77%

Figure 3.11 presents the vorticity fields of the first two POD mode shapes for the isothermal flow case of N1. The results show that, for all examined central nozzles, the dominant flow structures are helical PVC that is present in the first two POD modes. The presence of PVC structures are

associated with the occurrence of vortex breakdown, which is the case for all central nozzle geometries. The similar coherent structures' behavior and energy regardless of the central nozzle geometries might be attributed to the dominance of the swirling airflow momentum downstream of the mixing tube exit where the effect of vortex breakdown is more significant. However, the effect of the central nozzle geometry on the behavior of the coherent structures is more pronounced in the reacting flow case (see Fig. 3.12). The vorticity fields of the first POD mode show elongated vortical structures for single-orifice nozzles. These elongated vortical structures are an extension of those developing inside the mixing tube. However, multi-orifice nozzles exhibit less elongated vortical structures.



**Fig. 3.11.** Vorticity fields of the shapes of the first two POD modes of the isothermal flow case for N1 nozzle.



**Fig. 3.12.** Vorticity fields of the shapes of the first POD mode of the reacting flow case for the different central nozzle geometries.

Phase-averaging is performed on the linear superposition of the first pair of POD modes to investigate the behavior of coherent structures at different phase angles. The linear superposition of the first pair of POD modes is averaged at eight different phase angles separated by  $45^\circ$  (i.e.,  $45^\circ, 90^\circ, 135^\circ, \dots, 360^\circ$ ). Figure 3.13 shows selected vorticity fields of the linear superposition of the reconstructed first two POD modes at different phase angles. It shows that, as compared to single-orifice nozzles, some phases of multi-orifice nozzles display smaller and separated regions of strong vortical structures. The presence of these small-scale strong vortical structures enhances the mixing and further contributes to the improvement of flame stability [40]. On the other hand, single-orifice nozzles' flowfield is associated with the transition of long vortical structures upstream of the mixing tube exit, but no flashback is observed.

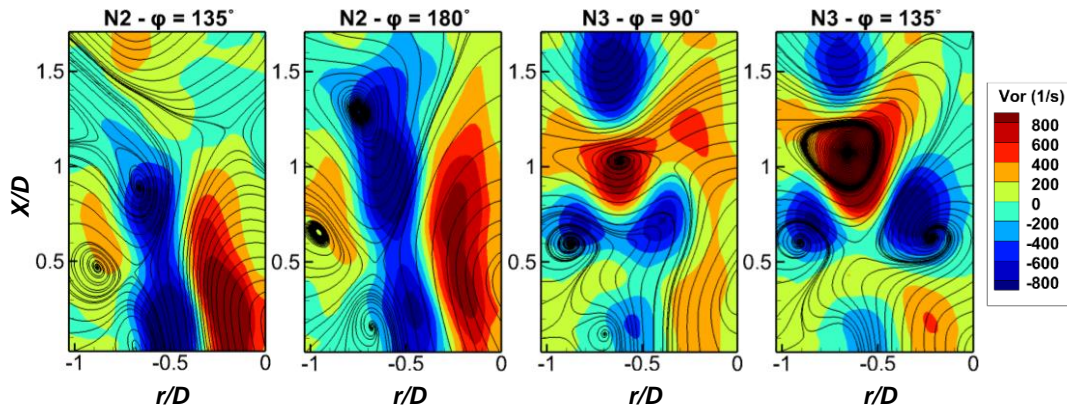


**Fig. 3.13.** Vorticity fields of the phase-averaged linear superposition of the first two POD modes for some phase angles of the reacting flow case for N2 and N3.

PIV measurements were conducted in the radial flow direction for different central nozzle geometries in the case of both, isothermal and reacting, flows to investigate whether PVC is suppressed in the reacting flow case or not. The results demonstrated the presence of typical

swirling flowfield, where the tangential velocity vectors can be seen rotating around the centerline (Fig. 3.14a). The POD mode shape of the first mode shows the occurrence of single helical PVC in the isothermal flow case for all examined central nozzle geometries, which is similar to that reported in [21]. However, compared to those of the isothermal flow case, the radial flowfield of the reacting flow, as shown in Fig. 3.14b, experience smaller in size vortical structures within the inner shear layer (ISL). This is an indication of the distortion of the precessing helical motion within the ISL in the reacting flow case.

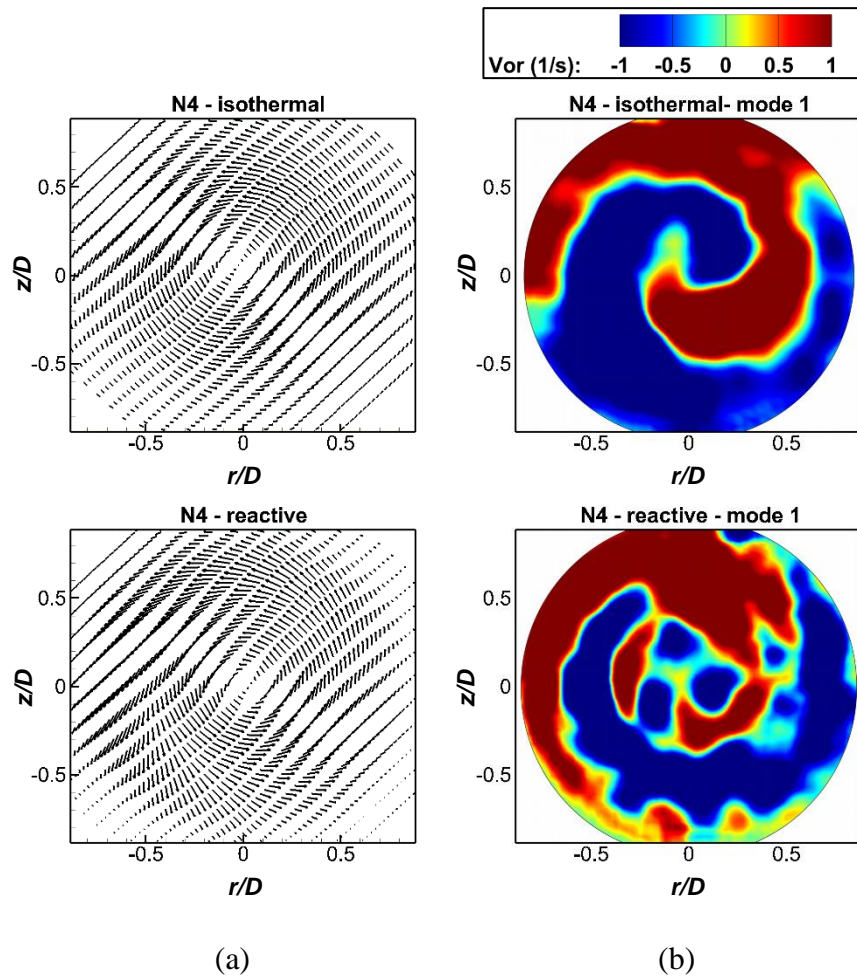


**Fig. 3.14.** (a) Time-averaged field of the azimuthal velocity ( $W$ ), and (b) the vorticity contours of the shape of the first POD mode of N4 in the isothermal (first row) and reacting flow (second row) cases.

Figure 3.15 depicts, as an example, the PSD of the axial velocity fluctuations for N2 and N4 of isothermal and reacting flowfields. The results reveal a well-defined peak for all nozzles in the case of the isothermal flow at a frequency of 429 Hz, which is the PVC frequency. The results of the reacting flow show a well-defined peak for single-orifice nozzles (e.g., N2), while only small peaks manifest for multi-orifice nozzles (e.g., N4). These peaks are found at approximately 162 Hz for all nozzles. This confirms the clear reduction of the amplitude of coherent structures in the case of reacting flow for multi-orifice nozzles. Also, the absence of the peak at 429 confirms PVC suppression by combustion. Although the amplitude of coherent structures is decreased in the presence of chemical reactions (combustion), multi-orifice nozzles still have the ability to further reduce coherent structures' amplitude.

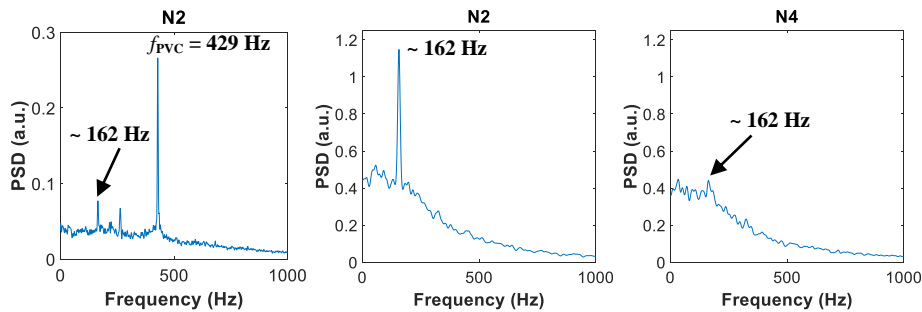


**Fig. 3.15.** PSD of the axial velocity fluctuations for (a) N2 in the case of isothermal flow, and (b) N2 and N4 in reacting flow case.

An indication of the effect of coherent structures' amplitude on the turbulent flowfield is the variation in the radial profiles of the axial and radial velocity with the phase angle. That is, higher PVC amplitude causes a significant variation in the axial and radial velocity with the phase angle. Therefore, the variation in the phase-averaged radial profiles of the axial and radial velocity with phase angle can be used as a qualitative indicator of the variation of the volumetric discharge with phase angle [41]. Figure 3.16 illustrates the radial profiles from the centerline of the phase-



averaged radial and axial velocity at different phase angles. The results show a slight variation of the volumetric discharge with the phase angle for multi-orifice nozzles. However, the variation is more pronounced for single-orifice nozzles. In addition, compared to multi-orifice nozzles, the peak axial velocity attains higher values for single-orifice nozzles, which implies higher entrainment and stronger dynamics associated with single-orifice nozzles.

In conclusion, the strong vortical structures upstream of the mixing tube exit results in larger oscillations in the volumetric discharge in the case of single-orifice nozzles, and hence induce stronger flame dynamics downstream of the mixing tube exit. In addition, the coherent structure' amplitude is attenuated in the presence of chemical reactions (combustion) due to high viscosity [8]. This results in a decrease in the angular momentum transfer through the central region and volume dilatation, which consequently leads to an attenuation of the coherent structures' amplitude. Furthermore, multi-orifice nozzles exhibits further attenuation of coherent structures' amplitude, whereas single-orifice nozzles promotes coherent structures.

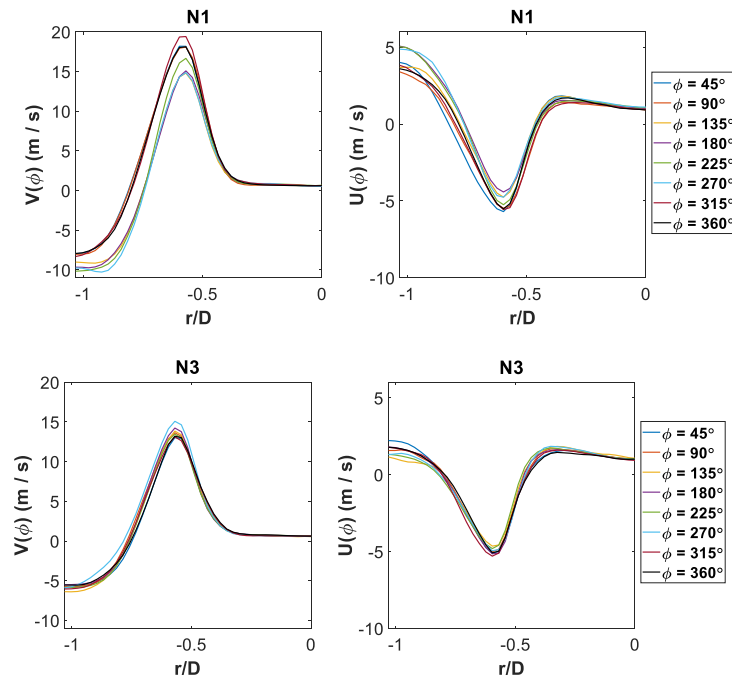




**Fig. 3.16.** Radial profiles of the phase-averaged radial and axial velocity at different phase angles in the reacting flow case for N1 and N3.

Figure 3.17a depicts the contours of the normalized mean density field obtained from QLS technique, which can be considered as a qualitative measurement method for mixing [22–25]. The results indicate that multi-orifice nozzles have the ability to enhance mixing, particularly within the central region. It can be observed that, compared to single-orifice nozzles, N4 (multi-orifice nozzle) exhibits darker central region, indicating a homogeneous lower flow density within this region. Moreover, the RMS of the normalized flow density is significantly higher with single-orifice nozzles (not shown here for conciseness). This indicates a less homogeneous density in the central region and hence a weak mixing as compared to that of multi-orifice nozzles. To confirm the results of QLS, the contours of the RMS velocity normalized by the mean bulk flow velocity ( $V_j$ ) are shown in Fig. 3.17b. These results show that single-orifice nozzles' flame exhibits higher value of RMS velocity particularly in the central region. This suggests that the interaction between the swirling flow and the jet flow discharged from a single-orifice nozzle persists up to downstream of the mixing tube exit, where large pockets of more rich mixture may reach the downstream region of the mixing tube exit, which hence causes a less mixing. On the other hand, the contours of turbulence intensity of multi-orifice nozzles show a better distribution in the central region with a higher gradient in the axial profiles of the axial turbulence intensity, indicating less effect of the axial flow and hence a more homogeneous distribution of fuel and air.

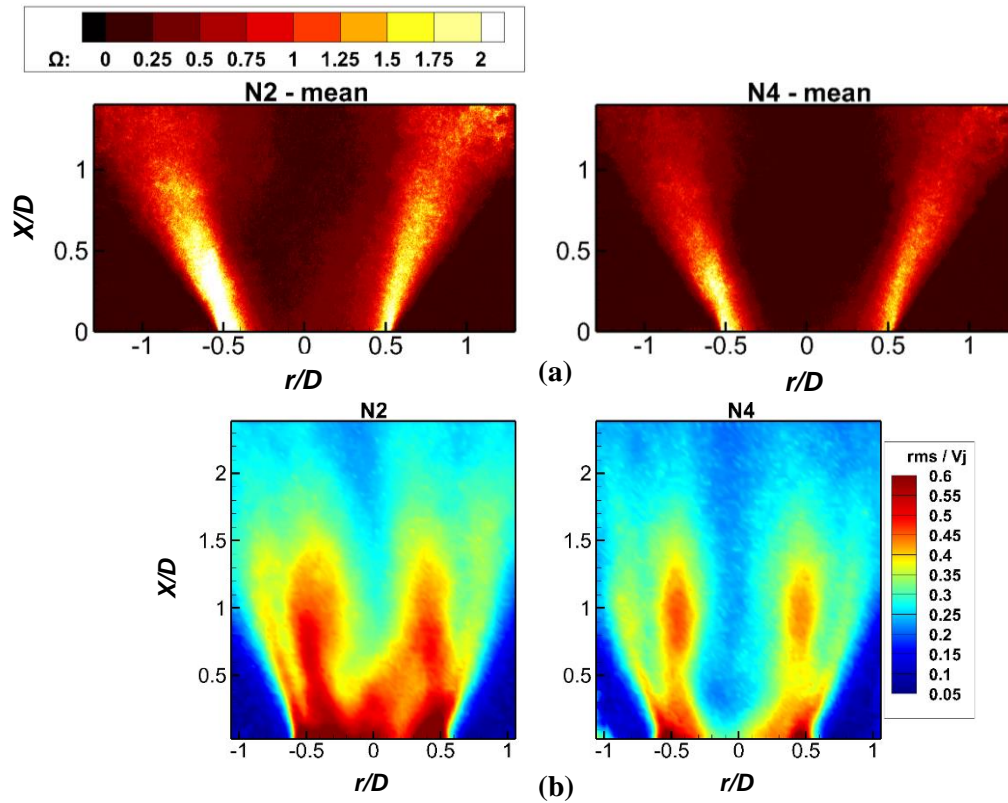


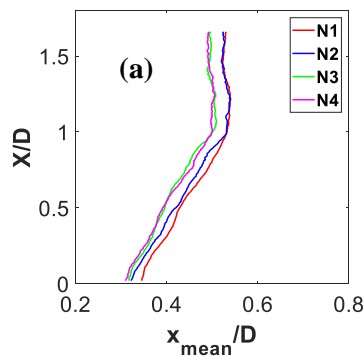
**Fig. 3.17.** Contours of (a) the normalized mean density fields, and (b) the normalized RMS velocity of N2 and N4.

### 3.4.3. Flame front dynamics

Mie scattering technique is used to acquire information on the time-resolved behavior of the flame front. The flame front position at each wing (i.e., right and left wings) is estimated by calculating the radial distance between the flame front surface and the mixing tube centerline at each  $X/D$ . Figure 3.18a presents the axial profiles of the mean flame front position normalized by the inner diameter of the mixing tube ( $D$ ). The results show that using less orifices in the central nozzle (single-orifice N1 and N2) nozzles results in higher mean and RMS (not shown here) flame front position which leads to more diverging flames. This implies that, compared to multi-orifice (N3 and N4) nozzles, flames of single-orifice nozzles experience larger eddies which corroborate the integral length scale findings reported in Table 1. Overall, both the mean and RMS of the flame

front position increase with  $X/D$ . These results are in line with those obtained by Kheirkhah and Gülder [42] for V-flames. It should be highlighted that premixed [42, 43] and stratified V-flames [44] are asymmetric as they are stabilized using a flame holder; whereas the PPFs in the present are asymmetric since they are stabilized by a swirl.

Flame brush thickness ( $\delta$ ) is estimated for different nozzles based on the mean progress variable (see Fig. 3.18b). As shown in Fig. 3.18c, the profile is similar to that of the error function, which allows representing the flame brush thickness as  $\delta = 1/\max(-dc/dx)$  according to Namazian et al. [45]. The results reveal approximately constant flame brush thickness upstream of  $X/D \approx 0.75$  which then followed by an increase with the axial distance. This behavior is different from that of V-flames which exhibit steady increase in the flame brush thickness with the axial distance in the entire flame region [42]. Single-orifice nozzles exhibit larger flame brush thickness as compared to that of multi-orifice nozzles. This shows the importance of turbulence intensity since single-orifice nozzles exhibit higher turbulence intensity than that of multi-orifice nozzles (Fig. 3.17b) while exhibiting larger flame brush thickness, a similar trend as in [46] for bluff-body stabilized lean premixed flames.



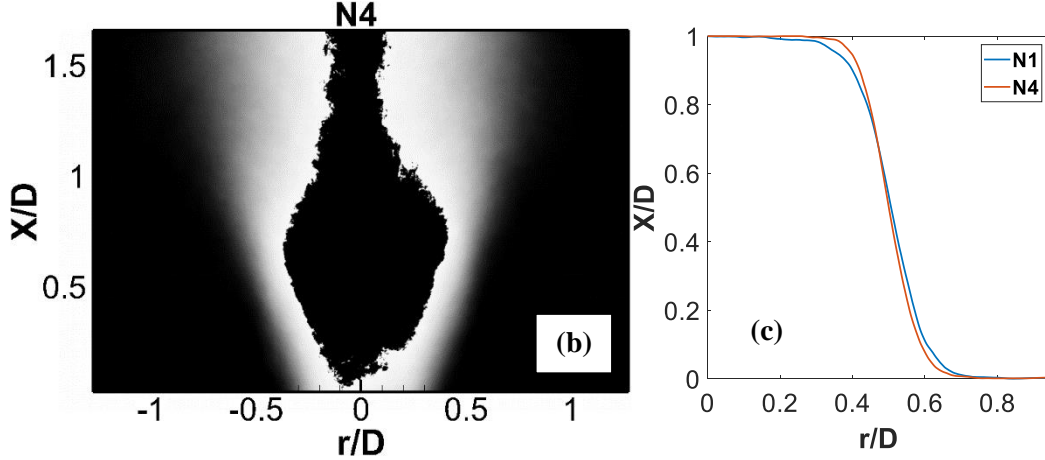


**Fig. 3.18.** (a) Axial profiles of the normalized mean flame front position, (b) contours of the mean progress variable,  $c$ , for N4 (black area in the core region represents  $c > 0.99$ ), and (c) variation of the mean progress variable,  $c$ , as a function of the normalized radial distance ( $r/D$ ) at  $X/D = 0.9$  for N1 and N4.

The axial profiles of the mean and the RMS of the right and left wings of the flame front seem to be symmetric around the mixing tube centerline, which is not the case in the instantaneous images. To determine the symmetry/asymmetry between the right and left wings, Hilbert transform technique is used [30]. The Hilbert transform is applied on the instantaneous fluctuations of the flame front position of the right and left wings as  $X^*_j = Hilbert(x'_j)$ , where  $j$  is the  $X/D$ ,  $x'_j$  is the flame front position fluctuation at a given  $X/D$  and frame, and  $X^*_j$  is the Hilbert transform complex function. The output complex function has real and imaginary components. The phase angles ( $\theta^\circ$ ) is calculated for both right ( $\theta^\circ_{right}$ ) and left ( $\theta^\circ_{left}$ ) wings of the flame front, and the difference between the two at different  $X/D$  is calculated. Finally, the phase angle at each  $X/D$  is averaged for all frames in order to estimate the mean phase difference ( $\Delta\theta^\circ_{mean}$ ) at each  $X/D$ . Figure 3.19a,b shows the axial profiles of the phase angles of the right and left wings of instantaneous images for, as an example, N2. These results indicate that the axial profile of the phase angle is most likely to behave as sawtooth wave. This is a clear evidence of the periodicity of the flame front surface. It is observed that the phase angle profile of the right wing is much different than

that of the left wing, indicating the asymmetry of the flame front surfaces of the right and left wings in the instantaneous image, as shown in Fig. 3.19a,b. In addition, the results reveal that flame front surfaces are asymmetric for all central nozzle geometries (see Fig. 3.19c). This is indicated by the relatively high values of the mean phase difference ( $\Delta\theta^{\circ}_{mean}$ ) along X/D. The  $\Delta\theta^{\circ}_{mean}$  ranges from 23° to -31° for N1, 30° to -25° for N2, 11° to -17° for N3 and 18° to -15° for N4. Overall, this indicates that the highest degree of asymmetry is observed with N1 (single-orifice) while the lowest with N4 (multi-orifice).

It is observed that multi-orifice nozzles, which promote coherent structures' suppression (see Figs. 3.8b and 3.10c), produces lower fluctuations of the flame front. The present results show good agreement with those reported in [43]; that is, the normalized mean flame front position and RMS of the flame front fluctuations are greater at elevated axial turbulence intensity, which is the case of single-orifice nozzles in the present study.

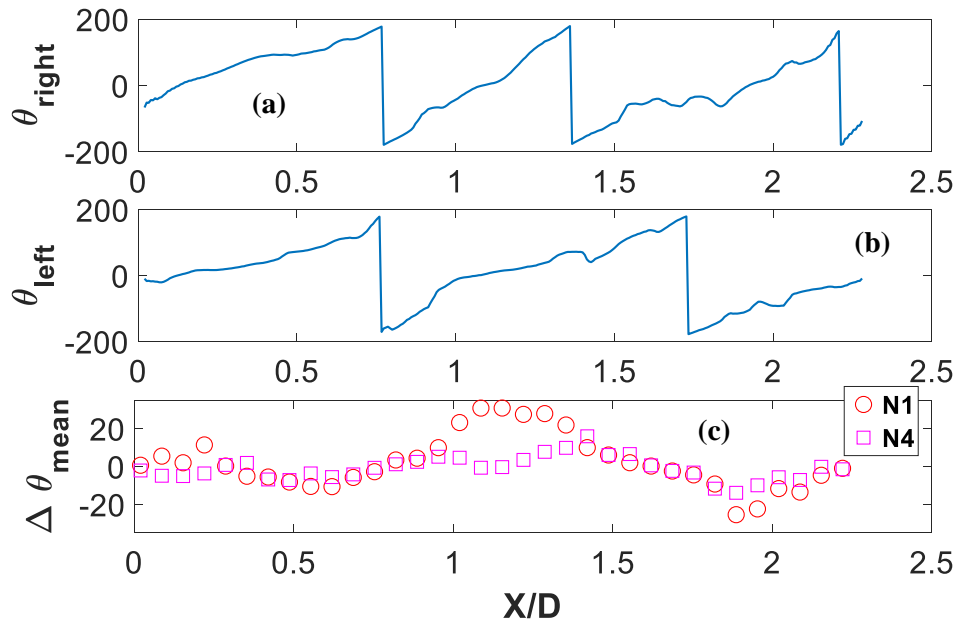


**Fig. 3.19.** Axial profiles of the phase angles of the (a) right and (b) the left wing of the flame front of instantaneous flame front positions for N2, and (c) mean phase difference between the right and left wings for N1 and N4 nozzles.

### 3.5. Discussion

The results presented above showed that varying the central fuel nozzle geometry and using a short mixing length allow generating different flowfields and hence mixing characteristics, which alter combustion instabilities of PPFs. For instance, contrary to multi-orifice nozzles, single-orifice nozzles' jet flows exhibit faster decay and higher spreading rate inside the mixing tube, which implies a higher entrainment in the central region ( $-0.2 < r/D < 0.2$ ). This is supported by the measurements of the integral length scale of the two-group nozzles, which is found larger for single-orifice nozzles (see Table 1). That is, larger eddies generated by single-orifice nozzles dissipate much slower than smaller eddies of multi-orifice nozzles. In addition, the results presented above demonstrated that single-orifice nozzles produce higher turbulence intensity along the centerline region of the mixing tube (see Figs. 3.5b and 3.6), in contrast to multi-orifice nozzles which exhibit homogeneous turbulence intensity field. This indicates that the flow, which discharges from a single-orifice nozzle, has a strong interaction with the swirling airflow issuing from the surroundings annulus. This results in a significant increase of the mixing in the flow central region. This is supported by the results of the single-orifice nozzles' mean velocity along the centerline inside the mixing tube which decays faster than that of multi-orifice nozzles (see Fig. 3.5a). Consequently, single-orifice nozzles induce a greater mixing in the central region of the mixing tube [47] as compared to that of multi-orifice nozzles whose mixing is uniform radially. This is because the intense shear between the axial flow from the central single-orifice nozzle and the surroundings swirling airflow results in higher entrainment and consequently faster decay of the jet flow issuing from the central nozzle. An earlier study by the present authors [16] found that

flashback occurs through the central region ( $-0.25 < r/D < 0.25$ ) in the vicinity of the high turbulent flow region. Thus, in the case of single-orifice nozzles, faster decay and higher centerline turbulence intensity inside the mixing tube create suitable conditions for flame flashback through the central region. On the other hand, multi-orifice nozzles produce a more homogeneous and lower turbulence intensity inside the mixing tube which implies a better upstream fuel-air distribution/mixing compared to that of single-orifice nozzles (with the exception of the central region of the mixing tube) but still not sufficient enough to allow flame flashback.

The characteristics of the upstream turbulent field are found to influence the mean field characteristics downstream of the mixing tube exit. Evidence of this can be seen by observing the difference in the centerline axial mean velocity and turbulence intensity between the single-orifice and multi-orifice nozzles (see Fig. 3.7b,d). For instance, single-orifice nozzles exhibit higher centerline turbulence intensity and stronger CRZ downstream of the mixing tube exit. At the same time, coherent structures' strength of single-orifice nozzles is significantly higher than that of multi-orifice nozzles, as shown in Figs. 3.8 and 3.10b,c. The larger and more elongated vortical structures of single-orifice nozzles in Fig. 3.13 corroborates the findings of the integral length scale in Table 1, which is higher for single-orifice nozzles. These results are in line with those reported in our previous study [16], where changing the fuel nozzle geometry affects coherent structures' amplitude. It should be noted that PVC, present in the isothermal flow case at  $f_{PVC} = 429$  Hz, is completely suppressed in the reacting flow case regardless of the central nozzle geometry. On the other hand, coherent structures suppression when using multi-orifice nozzles is evident as witnessed by the absence of large peaks of PSD of the axial velocity fluctuations compared to those of the single-orifice nozzles (see Fig 3.15b). High coherent structures' amplitude in the case of single-orifice nozzles affects the downstream flowfield in different ways. That is, higher

coherent structures' amplitude yields a significantly higher variation in volumetric discharge with the phase angle (see Fig. 3.16) which consequently leads to oscillations in the air-fuel ratio [41]. The QLS data in Fig. 3.17a clearly shows better mixing characteristics downstream of the mixing tube exit when using multi-orifice nozzles. This is attributed to the fact that, compared to single-orifice nozzles, the central jet flow (rich mixture) is split through several smaller orifices (see Table 1) in the case of multi-orifice nozzles, which consequently generate smaller scale eddies.

By comparing the turbulence intensity fields of the single-orifice nozzles inside and outside of the mixing tube (Figs 3.6 and 3.17b), the large values of the turbulence intensity are better distributed downstream of the mixing tube exit as compared to that inside of the mixing tube where it is concentrated in the central region. This further indicate a better overall mixing downstream of the mixing tube exit as compared to that inside the mixing tube. Additionally, stronger coherent structures, observed with single-orifice nozzles, have a significant effect on the flame front, as witnessed by highly asymmetric flame front (see Fig. 3.19) and higher flame front fluctuations. The strong shear between the central flow and its surroundings swirling airflow in the case of single-orifice nozzles (Figs. 3.5a and 3.7b) results in more divergent flames (Fig. 3.18a) that are more prone to interact with outwardly located large vortical structures.

The discussion above reveals that, in contrast to single-orifice nozzles, multi-orifice nozzles' flowfield does not stimulate conditions suitable for the occurrence of flashback, but promote better mixing downstream of the mixing tube exit, much weaker coherent structures' amplitude and lower flame front fluctuations, all of which promote stable combustion.

### **3.6. Conclusions**

The effect of central fuel nozzle geometry on the ensuing turbulent flowfield and its impact on coherent structures' suppression and hence stability of PPFs using a short mixing length is



experimentally examined. The main findings of this experimental study can be summarized as follows:

- Single-orifice nozzles exhibits faster decay and higher centerline axial turbulence intensity than their multi-orifice nozzles counterparts implying a different influence on the flowfield farther downstream of the mixing tube.
- Turbulence intensity of single-orifice nozzles exhibits peak values in the central region of the flowfield which indicates a significant difference in the mixing characteristics inside the mixing tube between the two group nozzles.
- Single-orifice nozzles features larger integral length scale, indicating a faster growth of the most energetic large structures, where the vortical structures of single-orifice nozzles are larger, more elongated and exhibit higher modal energy inside the mixing tube than those of multi-orifice nozzles.
- PVC, which is present in the isothermal flow case downstream of the mixing tube exit, is suppressed in the reacting flow case regardless of the nozzle geometry.
- Single-orifice nozzles induce higher negative peaks in the axial mean velocity and higher turbulence intensity in the early region of the flame along the centerline downstream of the mixing tube exit, indicating the presence of a stronger CRZ.
- The upstream turbulent field of single-orifice nozzles causes higher variation in the volumetric discharge indicating stronger flame dynamics.
- The PSD of velocity fluctuations of multi-orifice nozzles exhibit smaller peaks, which indicates that those nozzles further contribute to coherent structures' suppression.

- Single-orifice nozzles' flames are more divergent and exhibit higher flame front fluctuations and higher degree of asymmetry, which is a consequence of the effect of strong coherent structures' amplitude on flame front dynamics.

In summary, in contrast to single-orifice nozzles, multi-orifice nozzles promote coherent structures' suppression, better mixing, less flashback propensity due to less suitable conditions in the upstream flowfield, less volumetric discharge oscillations, less flame front oscillations, and more symmetric flame fronts. Consequently, contrary to single-orifice nozzles, multi-orifice nozzles have the ability to induce flow characteristics that promote PPFs stability.

## Nomenclature

$C$	particle density distribution
$c$	mean progress variable
$C_h$	homogeneous particle density distribution
$D$	inner diameter of the mixing tube (mm)
$d_o$	orifice diameter (mm)
$d_p$	seeding particle diameter (m)
$D_{cc}$	dark current of the camera
$D_e$	equivalent diameter (mm)
$f_{PVC}$	frequency of the precessing vortex core (PVC)
$I$	intensity of the acquired instantaneous image in reacting flow case
$I_h$	intensity of the acquired homogeneous particle density image in cold flow
$I_l$	local light sheet intensity
$I_o$	intensity of the background image
$L_m$	mixing length (mm)
$l$	orifice length (mm)
$M$	total number of velocity vectors in each acquired PIV image
$N$	number of acquired images
$R_q$	factor for reflections due to the use of quartz tube
$r$	radial position (mm)
$Re_D$	Reynolds number based on the inner diameter of the mixing tube
$S$	swirl number
$s$	axial position inside the mixing tube (mm)
$Sk$	Stokes number
$U$	radial velocity (m/s)
$V$	axial velocity (m/s)
$V_a$	factor for different viewing angles within the laser sheet plane

$V_{CL}$	centerline axial mean velocity (m/s)
$V_j$	mean bulk flow velocity (m/s)
$v'$	root mean square (RMS) of the axial velocity fluctuations (m/s)
$W$	azimuthal velocity (m/s)
$X$	axial position (mm)
$X^*_j$	Hilbert transform complex function
$x'_j$	flame front position fluctuation at certain axial position and certain frame
$x_{mean}$	mean flame front positions (mm)
$x_{RMS}$	RMS of the flame front positions
$z$	radial position normal to $r$ (mm)

### Greek symbol

$\alpha$	vane(s) angle of the swirl generator ( $^\circ$ )
$\Delta\theta^\circ_{mean}$	mean phase difference between the left and right wings of the flame front ( $^\circ$ )
$\delta$	flame brush thickness (mm)
$\varepsilon$	RMS error in estimating PIV velocity data (m/s)
$\theta^\circ$	phase angle of the flame front position ( $^\circ$ )
$\theta^\circ_{right}$	phase angles of the right wing of the flame front ( $^\circ$ )
$\theta^\circ_{left}$	phase angles of the left wing of the flame front ( $^\circ$ )
$\Lambda_L$	integral length scale (mm)
$\lambda_i$	POD modal energy of mode $i$
$\lambda_{th}$	threshold modal energy
$\rho$	fluid density ( $\text{kg/m}^3$ )
$\rho_h$	homogeneous fluid density ( $\text{kg/m}^3$ )
$\Sigma$	summation
$\Phi$	mixture/global equivalence ratio
$\varphi$	phase angle ( $^\circ$ )
$\Omega$	normalized fluid density

### Acronym

CRZ	central recirculation zone
FOV	field of view
ISL	inner shear layer
LDV	laser Doppler velocimetry
$\text{NO}_x$	nitrogen oxides
OSL	outer shear layer
PIV	particle image velocimetry
POD	proper orthogonal decomposition
PPFs	partially premixed flames
PSD	power spectral density (a.u.)
PVC	precessing vortex core
QLS	quantitative light sheet
RMS	root mean square
ROI	region of interest in the image
RSS	root-sum-square

### 3.6. References

- [1] Mansour, M. S., Elbaz, A. M., and Samy, M., 2012, “The Stabilization Mechanism of Highly Stabilized Partially Premixed Flames in a Concentric Flow Conical Nozzle Burner,” *Exp. Therm. Fluid Sci.*, 43, pp. 55–62.
- [2] Aggarwal, S. K., 2009, “Extinction of Laminar Partially Premixed Flames,” *Prog. Energy Combust. Sci.*, 35(6), pp. 528–570.
- [3] Syred, N., 2006, “A Review of Oscillation Mechanisms and the Role of the Precessing Vortex Core (PVC) in Swirl Combustion Systems,” *Prog. Energy Combust. Sci.*, 32(2), pp. 93–161.
- [4] Lee, S. Y., Seo, S., Broda, J. C., Pal, S., and Santoro, R. J., 2000, “An Experimental Estimation of Mean Reaction Rate and Flame Structure During Combustion Instability in a Lean Premixed Gas Turbine Combustor,” *Proc. Combust. Inst.*, 28(1), pp. 775–782.
- [5] Al-abdeli, Y. M., and Masri, A. R., 2015, “Review of Laboratory Swirl Burners and Experiments for Model Validation,” *Exp. Therm. Fluid Sci.*, 69, pp. 178–196.
- [6] Zhen, H. S., Leung, C. W., and Cheung, C. S., 2011, “A Comparison of the Thermal, Emission and Heat Transfer Characteristics of Swirl-Stabilized Premixed and Inverse Diffusion Flames,” *Energy Convers. Manag.*, 52(2), pp. 1263–1271.
- [7] Galley, D., Ducruix, S., Lacas, F., and Veynante, D., 2011, “Mixing and Stabilization Study of a Partially Premixed Swirling Flame Using Laser Induced Fluorescence,” *Combust. Flame*, 158(1), pp. 155–171.
- [8] Huang, Y., and Yang, V., 2009, “Dynamics and Stability of Lean-Premixed Swirl-Stabilized Combustion,” *Prog. Energy Combust. Sci.*, 35(4), pp. 293–364.
- [9] Samarasinghe, J., Peluso, S., Szedlmayer, M., De Rosa, A., Quay, B. D., and Santavicca, D. A., 2013, “Three-Dimensional Chemiluminescence Imaging of Unforced and Forced Swirl-

Stabilized Flames in a Lean Premixed Multi-Nozzle Can Combustor,” ASME J. Eng. Gas Turbines Power, 135(10), p. 101503.

[10] Roux, S., Lartigue, G., Poinso, T., Meier, U., and B\_erat, C., 2005, “Studies of Mean and Unsteady Flow in a Swirled Combustor Using Experiments, Acoustic Analysis and Large Eddy Simulations,” Combust. Flame, 141(1–2), pp. 40–54.

[11] Selle, L., Lartigue, G., Poinso, T., Koch, R., Shildmacher, K.-U., Krebs, W., Prade, B., Kaufmann, P., and Veynante, D., 2004, “Compressible Large Eddy Simulation of Turbulent Combustion in Complex Geometry on Unstructured Meshes,” Combust. Flame, 137(4), pp. 489–505.

[12] Gupta, A. K., Beer, J. M., and Swithenbank, J., 1977, “Concentric Multi- Annular Swirl Burner: Stability Limits and Emission Characteristics,” Proc. Combust. Inst., 14, pp. 79–91.

[13] Shih, W.-P., Lee, J. G., and Santavicca, D. A., 1996, “Stability and Emissions Characteristics of a Lean Premixed Gas Turbine Combustor,” Symp. (Int.) Combust., 26(2), pp. 2771–2778.

[14] Joo, S., Yoon, J., Kim, J., Lee, M., and Yoon, Y., 2015, “NO<sub>x</sub> Emissions Characteristics of the Partially Premixed Combustion of H<sub>2</sub>/CO/CH<sub>4</sub> Syngas Using Artificial Neural Networks,” Appl. Therm. Eng., 80, pp. 436–444.

[15] Kalt, P. A. M., Al-Abdell, Y. M., Masri, A. R., and Barlow, R. S., 2002, “Swirling Turbulent Non-Premixed Flames of Methane: Flow Field and Compositional Structure,” Proc. Combust. Inst., 29(2), pp. 1913–1919.

[16] Ahmed, M. M. A., and Birouk, M., 2018, “Effect of Fuel Nozzle Geometry and Airflow Swirl on the Coherent Structures of Partially Premixed Methane Flame Under Flashback Conditions,” Exp. Therm. Fluid Sci., 99, pp. 304–314.

- [17] Reichel, T. G., Terhaar, S., and Paschereit, O., 2015, “Increasing Flashback Resistance in Lean Premixed Swirl-Stabilized Hydrogen Combustion by Axial Air Injection,” *ASME J. Eng. Gas Turbines Power*, 137(7), pp. 71503–71509.
- [18] Iyogun, C. O., and Birouk, M., 2009, “Effect of Sudden Expansion on Entrainment and Spreading Rates of a Jet Issuing From Asymmetric Nozzles,” *Flow, Turbul. Combust.*, 82(3), pp. 287–315.
- [19] Iyogun, C. O., Birouk, M., and Kozinski, J. A., 2011, “Experimental Investigation of the Effect of Fuel Nozzle Geometry on the Stability of a Swirling Non- Premixed Methane Flame,” *Fuel*, 90(4), pp. 1416–1423.
- [20] Li, B., Baudoin, E., Yu, R., Sun, Z. W., Li, Z. S., Bai, X. S., Alden, M., and Mansour, M. S., 2009, “Experimental and Numerical Study of a Conical Turbulent Partially Premixed Flame,” *Proc. Combust. Inst.*, 32(2), pp. 1811–1818.
- [21] Stöhr, M., Sadanandan, R., and Meier, W., 2011, “Phase-Resolved Characterization of Vortex-Flame Interaction in a Turbulent Swirl Flame,” *Exp. Fluids*, 51(4), pp. 1153–1167.
- [22] Terhaar, S., 2015, “Identification and Modeling of Coherent Structures in Swirl-Stabilized Combustors at Dry and Steam-Diluted Conditions,” Ph.D. thesis, Technische Universität Berlin, Berlin, Germany.
- [23] Findeisen, J., Gnirb, M., Damaschke, N., Schiffer, H.-P., and Tropea, C., 2005, “Concentration Measurements Based on Mie Scattering Using a Commercial PIV System,” Sixth International Symposium on Particle Image Velocimetry, Pasadena, CA, Sept. 21–23.
- [24] Freund, O., Schaefer, P., Rehder, H.-J., and Roehle, I., 2011, “Experimental Investigations on Cooling Air Ejection at a Straight Turbine Cascade Using PIV and QLS,” ASME Paper No. GT2011-45296.

- [25] Terhaar, S., and Paschereit, C. O., 2012, “High-Speed PIV Investigation of Coherent Structures in a Swirl-Stabilized Combustor Operating at Dry and Stream-Diluted Conditions,” 16th International Symposium on Applications of Laser Techniques to Fluid Mechanics, Lisbon, Portugal, July 9–12.
- [26] Ahmed, M. M. A., 2019, “Experimental Study of Burner Geometry Effect on the Coherent Structures, Flashback, and Flame Front Dynamics of Unconfined and Confined Partially Premixed Swirling Methane Flames,” Ph.D. thesis, University of Manitoba, Winnipeg, MB, Canada.
- [27] Voigt, P., Schodl, R., and Griebel, P., 1997, “Using the Laser Light Sheet Technique in Combustion Research,” Proceedings of 90th AGARD-PEP Symposium on Non-Intrusive Measurement Techniques for Propulsion Engines, Brussels, Belgium, Oct. 20–24
- [28] Roehle, I., Schodl, R., Voigt, P., and Willert, C., 2000, “Recent Developments and Applications of Quantitative Laser Light Sheet Measuring Techniques in Turbomachinery Components,” *Meas. Sci. Technol.*, 11(7), pp. 1023–1035.
- [29] Chen, Y., Kim, M., Han, J., Yun, S., and Yoon, Y., 2007, “Analysis of Flame Surface Normal and Curvature Measured in Turbulent Premixed Stagnation- Point Flames With Crossed-Plane Tomography,” *Proc. Combust. Inst.*, 31(1), pp. 1327–1335.
- [30] Kheirkhah, S., Gülder, Ö. L., Maurice, G., Halter, F., and Gökalp, I., 2016, “On Periodic Behavior of Weakly Turbulent Premixed Flame Corrugations,” *Combust. Flame*, 168, pp. 147–165.
- [31] Knaus, D. A., and Gouldin, F. C., 2000, “Measurements of Flamelet Orientations in Premixed Flames With Positive and Negative Markstein Numbers,” *Proc. Combust. Inst.*, 28(1), pp. 367–373.

- [32] Miles, P. C., and Gouldin, F. C., 1992, “Mean Reaction Rates and Flamelet Statistics for Reaction Rate Modelling in Premixed Turbulent Flames,” *Proc. Combust. Inst.*, 24(1), pp. 477–484.
- [33] Tamadonfar, P., and Gülder, Ö. L., 2015, “Effects of Mixture Composition and Turbulence Intensity on Flame Front Structure and Burning Velocities of Premixed Turbulent Hydrocarbon/Air Bunsen Flames,” *Combust. Flame*, 162(12), pp. 4417–4441.
- [34] Chen, Y. C., Peters, N., Schneemann, G. A., Wruck, N., Renz, U., and Mansour, M. S., 1996, “The Detailed Flame Structure of Highly Stretched Turbulent Premixed Methane-Air Flames,” *Combust. Flame*, 107(3), pp. 223–244.
- [35] Pope, S. B., 2000, *Turbulent Flows*, Cambridge University Press, Cambridge, UK.
- [36] Ahmed, M. M. A., and Birouk, M., 2019, “Burner Geometry Effect on Coherent Structures and Acoustics of a Confined Swirling Partially Premixed Methane Flame,” *Exp. Therm. Fluid Sci.*, 105, pp. 85–99.
- [37] Fathali, M., Meyers, J., Rubio, G., Smirnov, S., and Baelmans, M., 2008, “Sensitivity Analysis of Initial Condition Parameters on the Transitional Temporal Turbulent Mixing Layer,” *J. Turbul.*, 9, pp. 1–28.
- [38] Epps, B. P., and Techet, A. H., 2010, “An Error Threshold Criterion for Singular Value Decomposition Modes Extracted From PIV Data,” *Exp. Fluids*, 48(2), pp. 355–367.
- [39] Raffel, M., Willert, C., Wereley, S., and Kompenhans, J., 2002, *Particle Image Velocimetry: A Practical Guide*, Springer, New York.
- [40] Sadanandan, R., Stöhr, M., and Meier, W., 2008, “Simultaneous OH-PLIF and PIV Measurements in a Gas Turbine Model Combustor,” *Appl. Phys. B*, 90(3–4), pp. 609–618.



- [41] Sadanandan, R., Stöhr, M., and Meier, W., 2009, “Flowfield-Flame Structure Interactions in an Oscillating Swirl Flame: An Investigation Using Phase Resolved and Simultaneous OH-PLIF and Stereoscopic PIV Measurements,” *Combust., Explos. Shock Waves*, 45(5), pp. 518–529.
- [42] Kheirkhah, S., and Gülder, Ö. L., 2013, “Turbulent Premixed Combustion in V-Shaped Flames: Characteristics of Flame Front,” *Phys. Fluids*, 25, pp. 1–23.
- [43] Kheirkhah, S., and Gülder, Ö. L., 2014, “Topology and Brush Thickness of Turbulent Premixed V-Shaped Flames,” *Flow, Turbul. Combust.*, 93(3), pp. 439–459.
- [44] Vena, P. C., Deschamps, B., Guo, H., Smallwood, G. J., and Johnson, M. R., 2015, “Heat Release Rate Variations in a Globally Stoichiometric, Stratified Iso-Octane/Air Turbulent V-Flame,” *Combust. Flame*, 162(4), pp. 944–959.
- [45] Namazian, M., Shepherd, I. G., and Talbot, L., 1986, “Characterization of the Density Fluctuations in Turbulent V-Shaped Premixed Flames,” *Combust. Flame*, 64(3), pp. 299–308.
- [46] Chowdhury, B. R., Wagner, J. A., and Cetegen, B. M., 2017, “Experimental Study of the Effect of Turbulence on the Structure and Dynamics of a Bluff- Body Stabilized Lean Premixed Flame,” *Proc. Combust. Inst.*, 36(2), pp. 1853–1859.
- [47] Mayer, C., Sangl, J., Sattelmayer, T., Lachaux, T., and Bernero, S., 2012, “Study on the Operational Window of a Swirl Stabilized Syngas Burner under Atmospheric and High Pressure Conditions,” *ASME J. Eng. Gas Turbines Power*, 134(3), p. 031506.

## **Chapter 4: Burner Geometry Effect on Coherent Structures and Acoustics of a Confined Swirling Partially Premixed Methane Flame**

### **4.1. Abstract**

The effect of the mixing tube length and fuel nozzle geometry on coherent structures and acoustics' characteristics of partially premixed swirling methane flame is experimentally studied. Particle image velocimetry (PIV) is used to document the flowfield inside the transparent confinement tube. Proper orthogonal decomposition along with phase-averaging are used to capture coherent structures. High-speed imaging is carried out to shed light on the flame front dynamics within the outer shear layer (OSL). The acoustic waves are measured using a Bruel & Kjaer type 4189 microphone. A radial-type swirl generator with a swirl number ( $S$ ) of 1.15 is adopted. Two different lengths of the mixing tube and two different geometries of the fuel nozzle with a similar equivalent diameter are tested. The swirling airflow and fuel flowrates are kept constant. The results showed a significant difference in the energy of coherent structures between the two central nozzle geometries with the same mixing length. Both, the mixing length and central nozzle geometry, are found to alter the integral length scale and the central recirculation zone (CRZ). The mixing length is found to alter the amplitude of the acoustics modes when using the same central nozzle geometry. However, keeping the same mixing tube and varying the central nozzle geometry has the same effect. The flame front dynamics within the outer recirculation zone (ORZ) is found to depend on both the central nozzle geometry and mixing tube length (i.e., level of mixing). High amplitude coherent structures are found to contribute to flame roll-up within the outer shear layer. The results showed that the mixing length is not the only parameter to mitigate

combustion instabilities. That is, combustion stability can be improved using a single-orifice nozzle with a long mixing length or a multi-orifice nozzle with a short mixing length.

## **4.2. Introduction**

Partially premixed flames (PPFs) are used in numerous combustion devices such as gas turbines, internal combustion engines, and industrial burners. PPFs can exhibit better flame stability than premixed and diffusion flames, and comparable pollutant emissions' characteristics to those of lean premixed flames [1]. The main feature of PPFs is the presence of multiple reaction zones which facilitate the interaction between different zones, which, in turn, further sustains chemical reactions and extends flame stability limits [2].

Swirl is used in many combustion applications in order to help improve fuel-air mixing process and flame stability. Swirl significantly affects several flow features such as decay rate, entrainment, and jet growth among others. At high swirl numbers ( $S > 0.6$ ), swirling flow is most likely to exhibit a central recirculation zone (CRZ), which acts as an aerodynamic blockage in the flow direction. The occurrence of periodic large-scale coherent structures, called precessing vortex core (PVC), is often associated with the formation of CRZ. It was found that both PVC and CRZ can affect flame position [3], which has a significant effect on combustion instability [4]. Despite the fact that PVC contributes to improved fuel-air mixing [5], it affects negatively the flowfield by provoking thermoacoustic oscillations [5], and altering the combustion process by modulating fuel-air mixing [6]. Nonetheless, PVC suppresses the receptivity of the shear layer to the acoustic oscillations which adds further complications to the coupling between heat release rate and acoustic modes [7]. The coupling between combustion and acoustic modes can lead to severe damage of a combustor [8], increases pollutant emissions [9], and induce flame extinction.

Acoustic waves can lead to a severe damage of a combustion chamber if these waves match the natural frequency of the combustor (i.e., resonance). The mechanism of combustion instabilities is not yet fully understood due to the complex interaction between the heat release rate, mixing, acoustic field, and velocity field [10]. For instance, acoustic waves propagate with the speed of sound and they can refract, diffract and reflect whereas vortical and entropic disturbances are convected out of a combustor. The occurrence of PVC depends on some parameters such as burner configuration/geometry, equivalence ratio, fuel supply/entry mode, and confinement level [11]. The mode of fuel entry (axial, radial or tangential) determines the location of flame front that strongly affects the occurrence of the PVC [11]. For instance, employing axial fuel injection with strong momentum which is interacting with air injected tangentially in a cone type burner followed by a cylindrical confinement was found to enhance flashback due to the enhancement of macroscopic mixing [12]. In addition, PVC can reappear after being suppressed at weak equivalence ratios [13]. Even after PVC suppression, swirling flames are prone to coupling with acoustic modes that can restore PVC [14].

One of the main constraints to understand the coupling mechanisms in swirling flames is related to the flame-vortex interaction complexity [3]. Partial premixing adds further complexity since describing PPFs requires more than a single conserved scalar [15]. The unmixedness within PPFs can also provoke thermoacoustic oscillations [16]. The level of partial premixing is found to be an important parameter for controlling flame stability, flashback, pollutant emissions, and combustion instability [1, 17]. The mixing tube length was found to significantly affect the amplitude of flame transfer function (FTF) [18]. Also, changing the contraction ratio of the exhaust nozzle and mixing tube length was shown to cause a significant change in the strength and location of large-scale vortices [19]. Some studies proposed the use of PPFs with a short mixing length to

mitigate combustion instabilities, but concluded that this may engender an increase in pollutant emissions [17]. To the authors' best knowledge, only a few attempts in the literature were made to study the coupled effect of fuel nozzle geometry and mixing tube length on coherent structure' behavior, especially when using axial fuel injection. For instance, it was reported that increasing the mixing length beyond a certain limit can increase flashback propensity, whereas using a relatively long mixing length does not always guarantee better mixing [5]. Some studies suggested the use of either a two co-rotating or counter-rotating swirl generator, or a multi-point fuel injection to enhance mixing [5]. It was revealed that the optimum conditions for flame stability and reduced pollutant emissions can be met at a certain partial premixing level [1].

Fuel nozzle geometry was found to alter some of the main features of the flowfield such as spreading rate, entrainment, decay rate, turbulent intensity and mixing [20-22]. Therefore, the geometry of the fuel injector is expected to influence turbulent flow characteristics within the mixing tube. Additionally, the axial mode of fuel entry through the fuel nozzle/injector can contribute to the PVC suppression. Based on this and the review above, the present study aims to investigate the effect of fuel nozzle geometry at different mixing tube lengths on coherent structures (PVC), acoustic modes, and flame front dynamics of confined partially premixed methane flames. Specifically, the present study attempts to investigate whether i) the axial mode of fuel entry suppresses PVC in particular and coherent structures' amplitude in general independently of fuel nozzle geometry; and ii) decreasing the mixing tube length mitigates combustion instability regardless the fuel nozzle geometry.

<b>Nomenclature</b>	
$A$	Cross-sectional area ( $\text{mm}^2$ )
$a_{i1}$	time coefficient of the first POD mode
$a_{i2}$	time coefficient of the second POD mode

CRZ	central recirculation zone
D	inner diameter of the mixing tube (mm)
$D_o$	outer diameter of the mixing tube (mm)
$f_1$	frequency of the first longitudinal mode (Hz)
FOV	field of view
FTF	flame transfer function
HSV	hue, saturation, value color space
IRZ	inner recirculation zone
ISL	inner shear layer
$k$	specific heats ratio
$L$	length of the confinement tube (m)
$n$	number of orifices
ORZ	outer recirculation zone
OSL	outer shear layer
PPFs	partially premixed flames
PSD	power spectral density
PVC	precessing vortex core
$R$	gas constant (kJ/kg.k)
$r$	radial position (mm)
rms	root mean square
$Re_D$	Reynolds number based on the inner diameter of the mixing tube
RGB	red, green, blue color space
ROI	region of interest
$S$	strain rate (1/s)
$S_{CL}$	centerline strain rate of the mean field (1/s)
$S$	swirl number
$s$	axial distance inside the mixing tube (mm)
SNR	signal-to-noise ratio
$T$	temperature (K)
$U$	radial velocity (m/s)
$V$	axial velocity (m/s)
$V_{CL}$	centerline axial mean velocity (m/s)
$V_j$	mean bulk flow velocity (m/s)
$V_{RMS}$	centerline axial rms velocity (m/s)
$v'$	root mean square (rms) of the velocity fluctuations (m/s)
$X$	axial position (mm)
<i>Greek symbols</i>	
$\Lambda_L$	integral length scale (mm)
$\lambda_i$	POD modal energy of mode i
$\Sigma$	summation
$\Phi$	mixture equivalence ratio
$\varphi$	phase angle (°)
$\omega$	vorticity (1/s)

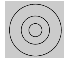
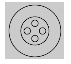
### 4.3. Experimental Setup and Methodology

#### 4.3.1. Burner configuration

Figure 4.1 depicts a schematic of the burner setup. The burner consists of two interchangeable tapered central (fuel) nozzles, two interchangeable mixing tubes, a swirl generator, and a confinement tube. The tapered central nozzles (named as N1 and N2), which have similar outer dimensions and similar orifice equivalent diameter (3 mm), as shown in Fig. 4.1a, are used to reduce the flame-holding effect inside the mixing tube. The diameter of each orifice of N2 is calculated as  $d_o = \sqrt{4A_{N1}/\pi/n_{N2}}$ , where  $A_{N1}$  is the orifice cross-sectional area of N1, and  $n_{N2}$  is the number of orifices of N2. Nozzle N2 provides multi-point injection which aims to accelerate and enhance the mixing [23]. Both nozzles, which have similar equivalent diameter (3 mm), exhibit similar local momentum flux, while the dissipation is faster with N2 due to smaller length scale. The two mixing tubes have a similar inner ( $D = 24$  mm) and outer diameter ( $D_o = 36$  mm) but with different lengths (this results in a mixing tube length/diameter ratio of 1.42 and 2.5). The distance between the tip of the central nozzle and mixing tube exit plane is called the mixing length (see Fig. 4.1b). The mixing tube length is used as an indicator of the level of partial premixing [1], where longer mixing tube implies higher partial premixing level. The lengths of the two mixing tubes are 34 and 60 mm, which represent low partial premixing level (high level of mixture inhomogeneity) and high partial premixing level (low level of mixture inhomogeneity), respectively. The combination of fuel nozzle geometry and mixing length is denoted as N1S, N1L, N2S and N2L, where 1, 2, S, L stand for nozzle 1, 2, short and long mixing tube, respectively. Varying the mixing tube length is expected not only to alter the mixture inhomogeneity level, but also can affect to some extent the characteristics of the turbulent field such as turbulence intensity and integral length scale. A fused silica quartz tube of 200 mm length, 90 mm inner diameter and

2.5 mm wall thickness is used as a confinement to facilitate the optical access of the laser sheet. For acoustics measurements, a stainless steel water-cooled tube of 200 mm length is used. A radial-type swirl generator of 60° vane angle is used to produce the swirling motion of the airflow introduced around the central nozzle. Radial-type swirl generators are known to generate stronger recirculation zone, as compared to that of axial-type swirl generators [6, 24]. The geometrical swirl number corresponding to the 60° vane angle is 1.15 [21]. A fuel rich premixed mixture of 17 LPM and 10.5 LPM of methane and air, respectively, is introduced through the central nozzle (fuel-air are completely mixed prior to their injection through the nozzle). The purpose of introducing rich premixed mixture from the central nozzle (with an equivalence ratio  $\phi$  of 15.4) is to eliminate flashback which could be promoted at this swirl number (i.e.,  $S = 1.15$ ). The swirling mixture is introduced into the atmospheric combustion chamber where it is ignited using a spark plug. Details of the test conditions are listed in Table 4.1.

**Table 4.1.** Experimental test conditions.

Cases		Swirl number $S$	Mixing length (mm)	Swirling airflow rate (LPM)	Central nozzle flow rate (LPM)	Mixture equivalence ratio $\phi$	$V_j$ (m/s)	$Re_D$
N1S		1.15	34	266.85	27.5	0.58	10.85	15975
N1L			60					
N2S			34					
N2L			60					

#### 4.3.2. Laser diagnostics

Particle image velocimetry (PIV), as depicted in Figure 4.1a, was used to investigate the mean flowfield characteristics and coherent structures. Laser Doppler velocimetry (LDV) was used to determine the PSD of the axial velocity fluctuations of the isothermal flow case on the centerline at an axial distance of 4 mm from the dump plane. The choice of this location is based



on the fact that the associated dynamics retains the features of that inside the mixing tube. Since details of the experimental setups of PIV and LDV were reported elsewhere [25], only a brief description is given in the present paper. For PIV measurements, a total of 1000 image pairs were captured at each case. Incense particles of an average diameter of  $1\ \mu\text{m}$  is used as tracers for the isothermal flow measurements. For the reacting flow measurements,  $\text{TiO}_2$  particles are used as seeding particles due to their thermal stability at high temperatures. The maximum particles size in the image was found to be 4 pixels. Emitting the laser sheet through the quartz tube wall was found to increase the intensity of the accumulated particles onto the quartz tube in the captured image, which deteriorates particles images. This problem was solved by emitting the laser vertically via a  $45^\circ$  2-inch protected silver mirror, as shown in Fig. 4.1a, where the laser sheet has no contact with the quartz tube wall. The intensity of the reflected laser on the wall was significantly reduced. Image dewarping was required to fix the optical distortion caused by a 2.5-mm thick quartz tube. The field of view is cropped into two region of interests (ROI). A large ROI ( $65 \times 115\ \text{mm}^2$ ) was used to capture the mean field of view and determine the locations where coherent structures are dominant. The small ROI ( $65 \times 54\ \text{mm}^2$ ) was selected such that it contains only the locations where coherent structures are dominant. As a result, the modes energy were significantly increased when reducing the ROI [26]. In both ROIs, the positions at longer distances from the confinement tube centerline, where the curvature is steep normal to the camera direction, are avoided in the captured image pairs in order to avoid the near-wall striations. The resultant pixel resolution was found to be  $55\ \mu\text{m}$ .

LDV measurements in the reacting flow case were challenging due to the large amount of  $\text{TiO}_2$  seeding particles required, which accumulated onto the quartz wall and significantly reduced the signal-to-noise ratio (SNR). Thus, LDV measurements were performed on the corresponding

isothermal flow case using incense particles with a diameter of approximately 1  $\mu\text{m}$ . The measurements were accomplished using a total of 200,000 data at a sampling frequency of 2.8 kHz. An in-house developed Matlab code was used to resample the raw data where a Hampel filter and Savitzky-Golay filter of 3<sup>rd</sup> order and length of segment of 9 were used in order to remove the outliers and smoothen the raw velocity data, respectively.

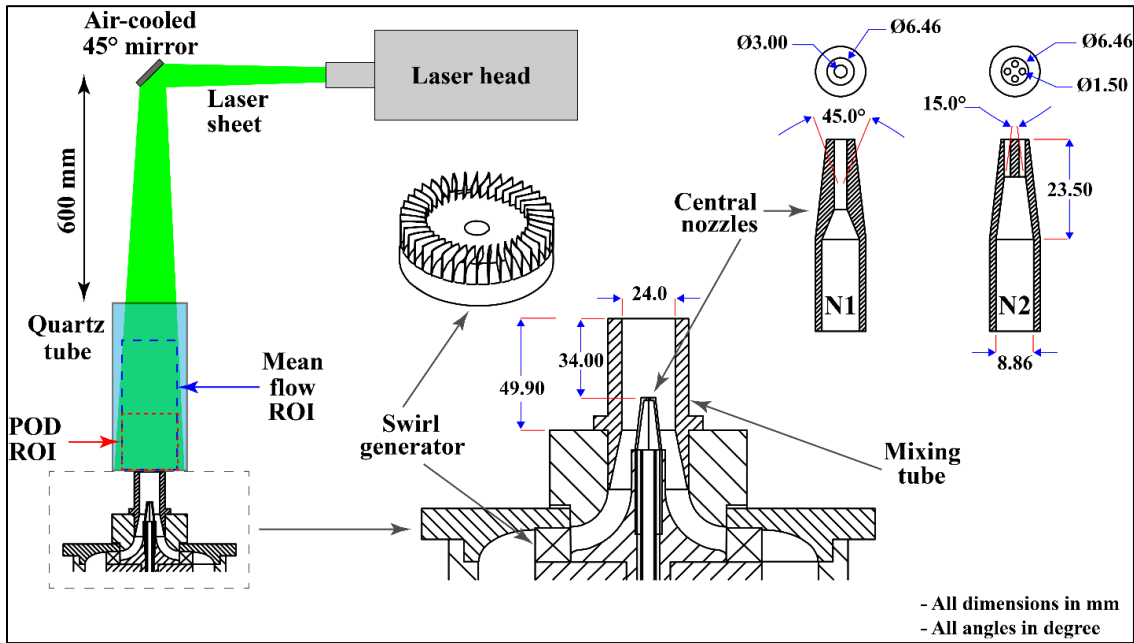


**Fig. 4.1.** PIV setup configuration and the ROI, and burner configuration including the swirl generator and central nozzles.

#### 4.3.3. Acoustics and flame appearance measurements

Figure 4.2 depicts a schematic of the setup for acoustics measurements. Bruel & Kjaer type 4189 microphone was positioned through a hole in a semi-infinite waveguide. The semi-infinite waveguide is connected to a water-cooled confinement tube through a 200-mm stainless steel tube which is flush-mounted in the confinement tube. The inner diameter and the length of the semi-infinite waveguide are 19.05 mm and 25 m, respectively, and it is positioned as a helix of 0.5 m diameter (see Fig. 4.2), similar to that in [23]. Similar amount of cooling water was flowed in order

to maintain a similar output cooling water temperature to keep the wall temperature constant for all cases. The microphone was calibrated before and after each test using type 4230 Bruel & Kjaer calibrator that generates sound with  $94 \pm 0.3$  dB and  $1000 \pm 1.5$  Hz at 23 °C. The microphone was connected to a Bruel & Kjaer sound level analyzer type 2260 Investigator and operated by BZ7210 v2.2 software. The Bruel & Kjaer type 4189 microphone was then placed in a Bruel & Kjaer 4230 sound level calibrator. Upon the completion of the internal calibration, the calibrator was turned on for external calibration in order to generate the correct sound pressure level. The resultant final deviation was found -0.03 dB. The dynamic range was selected at 50.6 – 130.6 dB. The signal was converted into a pressure fluctuation with a sensitivity of 50 mV/Pa.

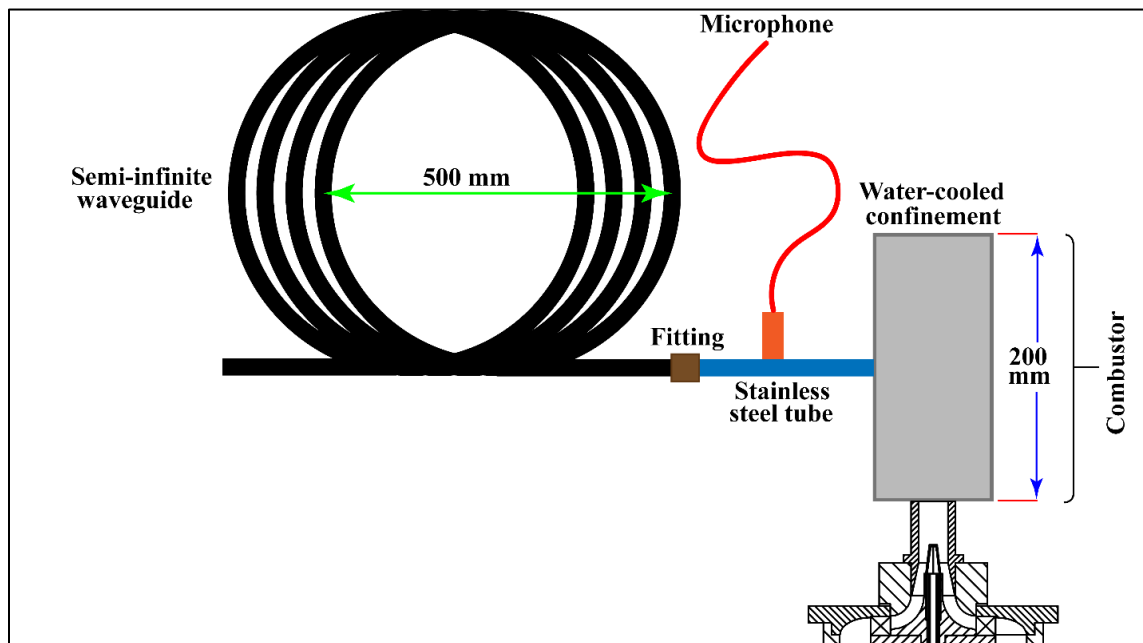


**Fig. 4.2.** Schematic representation of the acoustics measurement configuration.

For flame front dynamics, a total of 1200 flame images were captured at 400 fps using Nikon 1 V2 camera having a resolution of 0.14 mm/pixel and a maximum ISO of 6400. The camera was equipped with Nikon AF-S VR Micro-Nikkor 105mm f/2.8G objective. An optimal shutter

speed of 1/4000 s was used in order to avoid the blur of flame edges. Flame imaging provides comparatively qualitative information on the flame front behavior for different central nozzles and different lengths of the mixing tube. Since the quality of the captured images were significantly affected by the frame rate, a procedure for image enhancement should be followed [27]. One of the possible ways to enhance flame images was achieved using a HSV (Hue, Saturation, Value) color space [28][29]. An in-house developed Matlab code was used for images' enhancement (see Fig. 4.3a). The blue component (Fig. 4.3a,ii) in the acquired images in the RGB (Red, green, Blue) color space (Fig. 4.3a,i) was intensified and combined with the red and green components (Fig. 4.3a,iii). These images were converted to a HSV color space in order to further improve the blue component of the flame. Each component in the HSV color space (i.e., hue, saturation, and value) varies from 0 to 1 (see Fig. 4.3b), where value component indicates the brightness and hue component indicates the color. The blue range lies between 0.5 and 0.7 in the hue component. After increasing the value and saturation of the blue color, the HSV components were combined again (Fig. 4.3a,iv). The HSV images were converted back to the RGB color space and binarized to detect the edges (Fig. 4.3a,v). Finally, the edges of the flame were smoothed using moving average filter of  $3 \times 3$  pixel<sup>2</sup>. It should be noted that this method of detecting the flame front positions is based on the line-of-sight method. The main drawback of this method is that only the outer contour of the flame front positions is detected whether it is on the same plane or not. The consequences of using this method onto the results is discussed in the results and discussion section.

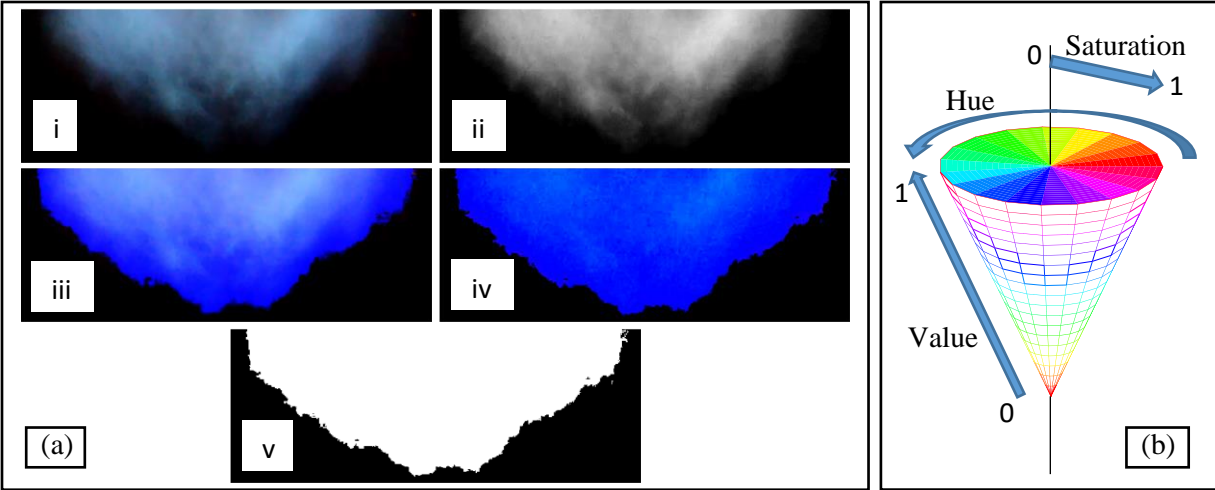


**Fig. 4.3.** (a) Flame edge detection procedure, and (b) illustration of HSV color space.

#### 4.3.4. Error analysis

Error estimation of PIV, LDV, acoustics, and high-speed imaging measurements was performed. Further details on the main sources of error and the methodology of error estimation can be found elsewhere [25]. For PIV measurements, the uncertainty due to the truncation error was estimated to be less than 1%. A maximum measurement error of 1% was estimated by using particle image density of higher than 10 particles per interrogation area. The use of high accuracy sub-pixel interpolation led to a maximum displacement error of 6%. The estimated total error was found approximately  $\pm 0.4$  m/s.

The LDV estimated total error was found less than  $\pm 0.2$  m/s. The acquisition time of a total of 200,000 instantaneous velocities was  $\sim 10^5$  times the integral time scale which guaranteed the convergence of the data. The relative uncertainty of the instantaneous velocity measurement was less than  $\pm 0.006$ . For acoustics measurement, the calibration revealed a bias of 0.1 Hz in the frequency estimation. Moreover, the large number of data ( $> 5 \times 10^6$  pressure fluctuations) significantly minimized the standard error and made it negligible. In addition, inserting the

microphone inside the semi-infinite waveguide prevented the ambient noise to be mixed with the input signal to the microphone.

In the plane perpendicular to the camera, the flame front position close to the quartz tube centerline was less affected (distorted) by the quartz wall curvature as compared to that near the quartz tube wall. In order to minimize the error resulted from this effect, image dewarping as a function of the radius was made to remap the images according to the distance from the centerline. In this procedure, a black-dotted white board or checkerboard, with known dot/square dimensions and spacing, is placed in the plane perpendicular to the camera inside the quartz tube. A comparison of the dots or square locations is made between the cases with and without the quartz tube. This allowed to track the positions as a function of the quartz tube radius. A shutter speed of 1/4000 s was selected in order to avoid the blurring of the flame front. An image resolution of 0.14 mm/pixel resulted in an average error in the mean flame front positions of  $\pm 3\%$ . The binarization threshold is a critical parameter since the incorrect threshold can either remove part of the flame front or add background noise to the flame front. The optimum binarization threshold was selected as 20% of the unburnt region while the selected filter for noise reduction was a median filter of  $9 \times 9$  window size. The maximum standard error related to the highest rms value was  $\pm 0.5$  mm, and the maximum uncertainty due to the post-processing was estimated to be  $\pm 1\%$ .

#### **4.4. Results and Discussion**

Results on the effect of the central nozzle geometry and the length of the mixing on the central region's axial mean velocity and its corresponding turbulence intensity are presented in first sub-section below. In addition, the effect of the central nozzle geometry and the mixing tube length on the integral length scale and CRZ are investigated and included. The second subsection

discusses the effect of the central nozzle geometry and the mixing tube length on the coherent structures in the velocity field. The third subsection presents the flame dynamics within the outer shear layer (OSL) for each examined test case, and finally, the fourth subsection discusses the acoustic field characteristics and its relationship with the flame dynamics.

#### *4.4.1. Mean velocity field characteristics*

Figure 4.4a,b presents, respectively, the streamlines of the mean velocity field of both, isothermal and reacting, flow cases for different central nozzle geometry and different mixing tube lengths. In this figure, a large inner (IRZ) and an outer recirculation (ORZ) zones are observed along with the vortex breakdown downstream of the dump plane. The CRZ is associated with the presence of negative velocities in the central region of the flame and two counter-rotating vortices within the shear layer. The location of the point indicated by the brown dot in Fig. 4.4a,b implies that the flowfield is asymmetric since it is off-centered around the upstream stagnation point. This flow most likely represents the asymmetric helical vortex breakdown [11, 30]. This might be an indication of the occurrence of PVC [31]. Therefore, POD analysis is used in the section below to investigate whether PVC is promoted or suppressed. The black solid line in Fig. 4.4c,d represents the zero-velocity line ( $V = 0$ ) that surrounds the negative velocity region in the central zone of the mean flowfield. The results show that the IRZ in the isothermal flow cases does not exhibit a strong negative velocity while it expands farther downstream (see Fig. 4.4a,c). On the other hand, the IRZ in the reacting flow cases (Fig. 4.4b,d) exhibits a strong negative velocity with a slight expansion of the IRZ downstream of the FOV, indicating a stronger, but a shorter CRZ in the reacting flow cases. The dilatation in the reacting flow cases causes the axial velocity to be significantly higher than that of its counterpart isothermal cases. The CRZ size is obviously

different in the reacting flow cases as compared to that of its isothermal counterparts. Increasing the mixing tube length does not lead to a reduction in the CRZ height in isothermal flow cases. The results show that, in the reacting flow cases, increasing the mixing tube length has a significant effect on the CRZ size for N1, while there is only a slight effect for N2, as shown in Fig. 4.4d. In addition, the CRZ size of N1S indicates that the flame is shorter compared to the other cases. Shorter flames may promote unstable combustion [6, 32], where the length of the flame plays an important role in facilitating the interaction between the flow dynamics and heat release oscillation.



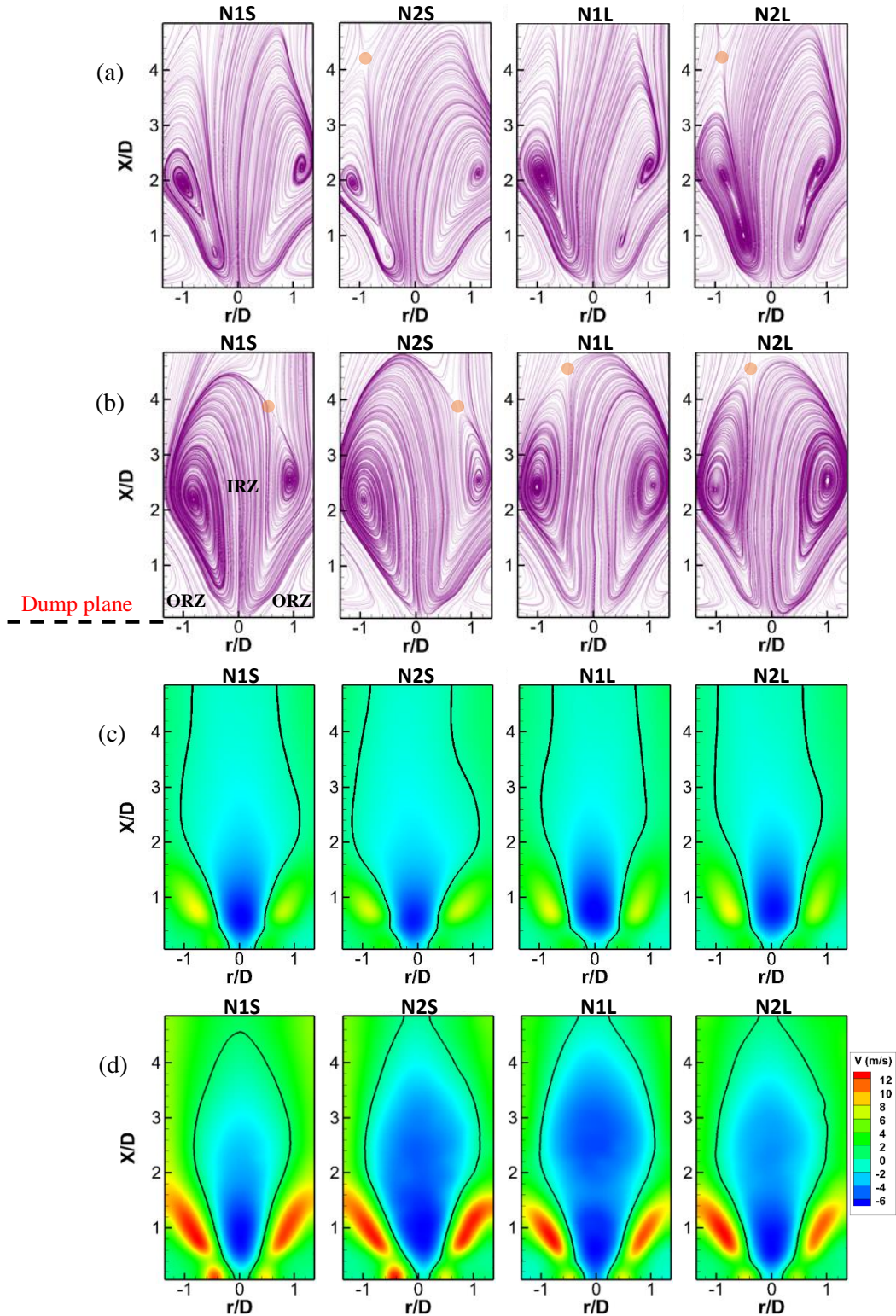


**Fig. 4.4.** Typical streamlines of the mean velocity field of the (a) isothermal and (b) reacting cases, and contours of the axial mean velocity of (c) isothermal and (d) reacting cases (the black solid line represents  $V = 0$ ) for different central nozzle geometries and different mixing tube lengths.

The profiles of the centreline axial mean velocity of the reacting flow cases are presented in Fig. 4.5a, which show that the highest negative velocity is attained with N1S followed by N2L. This high negative velocity does not necessarily indicate a shorter flame length, yet it supports the findings in Fig. 4.4d where smaller size CRZ occurred in the two aforementioned cases. It is observed that the centerline axial mean velocity increases with N1 as the mixing tube length increases, whereas this trend is the opposite with N2. Moreover, the centerline axial mean velocity of N1S is lower than that of N2SS, whereas this trend is the opposite with a longer mixing tube. It was reported that the backflow intensity controls the suppression or excitation of PVC [33, 34]. Thus, the results in section 3.2 corroborate this trend. Moreover, this trend is not similar to that in the case of isothermal flow (Fig. 4.5b), where it most likely depends only on the mixing tube length. Figure 4.5c shows the profiles of the axial rms normalized by local axial mean velocity for the reacting flow cases. These profiles show that increasing the mixing tube length significantly reduces the normalized axial centreline rms velocity in the very near-field region of the flame ( $X/D < 1$ ). This indicates that the effect of the central nozzle flow momentum on the central region of the flame is more pronounced at shorter mixing lengths in the reacting flow cases. This trend is reversed in the isothermal flow cases (see Fig. 4.5d), implying a significant effect of the central nozzle geometry in the presence of heat release.

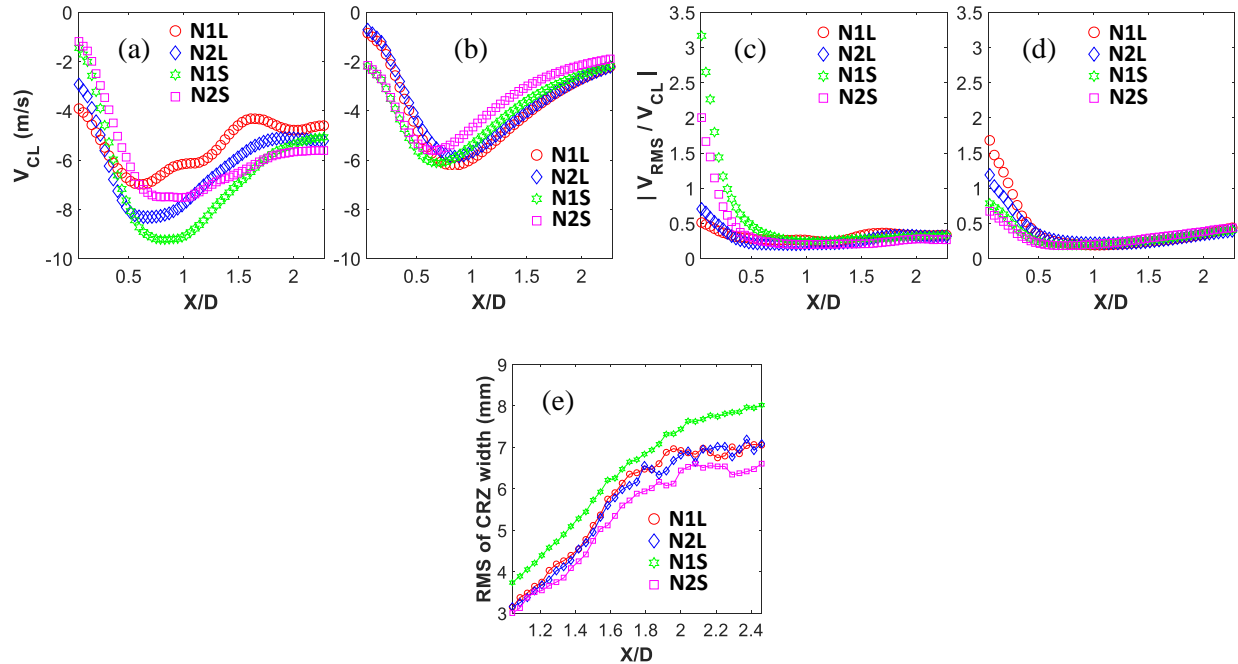


**Fig. 4.5.** Profiles of the centerline axial mean velocity of (a) reacting and (b) isothermal cases, the absolute normalized centerline axial rms velocity of (c) reacting and (d) isothermal cases, and (e) rms of the CRZ width of the reacting flow cases for different central nozzles at different mixing tube lengths.

It is essential to examine the behavior of the CRZ since it significantly affects the combustion dynamics, as CRZ size can alter combustion instabilities [11]. The profiles of rms of the CRZ width for different reacting flow cases at different  $X/D$  are shown in Fig. 4.5e. The CRZ width at each  $X/D$  is estimated as the radial distance between the zero-velocity lines for each instantaneous velocity vector map. The results show that the rms of the CRZ width increases with  $X/D$ . The highest rms of the CRZ width is attained with N1S, indicating higher CRZ oscillations; while the lowest is attained with N2S (see Fig. 4.5e). The presence of swirling jet flame between the IRZ and ORZ results in the occurrence of an inner (ISL) and an outer shear layer (OSL) (see Fig. 4.6). The contours of the axial turbulence intensity for the reacting flow cases in Fig. 4.6 show that high velocity gradients' region is present in the ISL and OSL which result in high axial turbulence intensity. The highest turbulence intensity is attained with N1S, where the white-colored region, which represents ISL, is the largest.

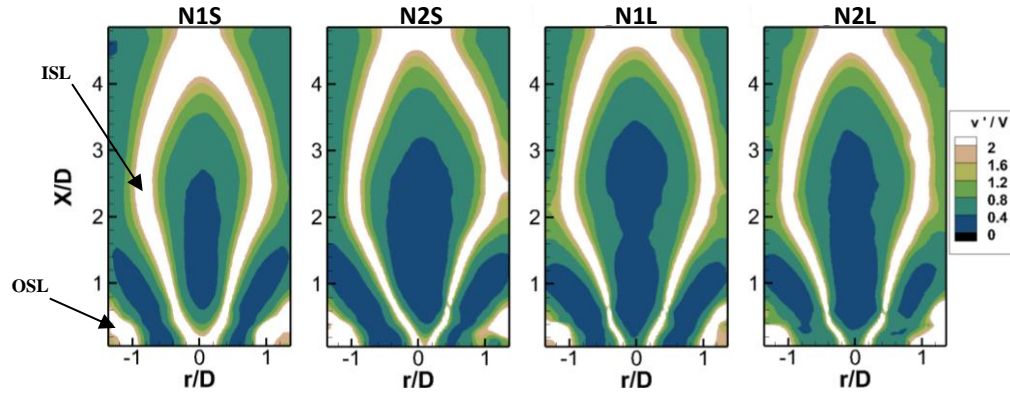


**Fig. 4.6.** Contours of the axial turbulence intensity for the different central nozzle geometries and different mixing tube lengths in reacting flow cases.

The longitudinal integral length scale ( $\Lambda_L$ ), which represents the size of large-scale turbulent eddies, is calculated in the case of isothermal flow along the centerline at a distance of 3 mm downstream of the dump plane. Note that PIV velocity data is used to determine the integral length scale, which is estimated by integrating the autocorrelation function of the axial velocity along the centreline [35]. Despite the fact that the longitudinal integral length scale inside the mixing tube increases as the mixing tube length increases, increasing the mixing tube length does not necessarily result in a larger longitudinal length scale outside of the mixing tube due to the formation of CRZ. Table 4.2 shows that the longitudinal length scale is approximately one-half of the characteristic length scale ( $D$ ). The largest longitudinal integral length scale is achieved with N1S and N2L. For N2, the integral length scale is proportional to the length of the mixing tube as expected.

**Table 4.2.** Longitudinal integral length scale ( $\Lambda_L$ ) for different central nozzles and different mixing tube lengths.

Cases	$\Lambda_L$ (mm)
N1S	13.0588
N1L	11.0139
N2S	11.5102
N2L	11.995

It is of importance to show the turbulence intensity contours just upstream of the mixing tube exit (see Fig. 4.7). This is a qualitative indication of the difference in the mixing characteristics between the different cases. As expected, the results show a decrease in the turbulence intensity as the mixing tube increases. It is observed that the contours of the turbulence intensity of N1L is somewhat similar to that of N2S. This implies that the influence of the flowfield of N1 still persists even farther down inside the mixing tube. In addition, the low level of turbulence intensity of N2L indicates a less influence of the flowfield of N2 at high axial distance (farther down the mixing tube) which partly mitigate the role of the axial fuel injection on PVC suppression. Turbulence intensity and integral length scale inside the mixing tube along with the level of mixture inhomogeneity all have an effect on the flame dynamics as discussed in the sections below.

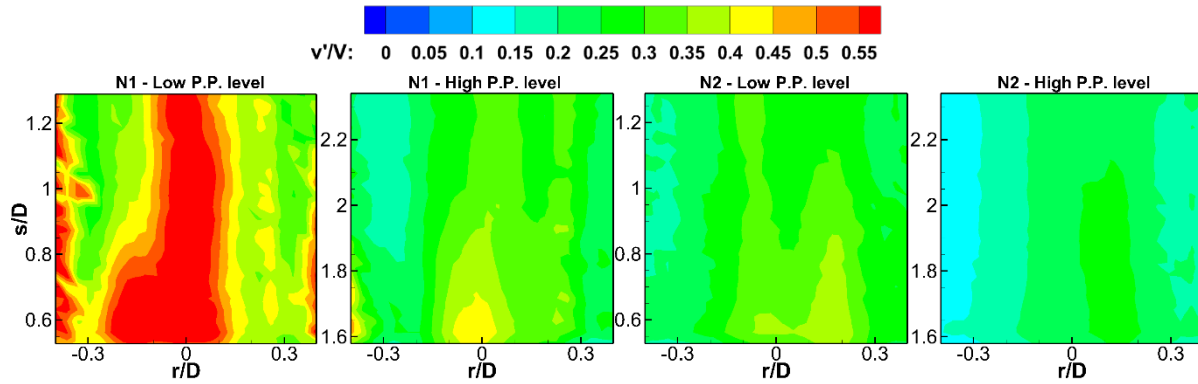


**Fig. 4.7.** Contours of the axial turbulence intensity inside the mixing tube for different central nozzles and different mixing tube lengths.

The behavior of the strain rate structures play an important role on flame wrinkling and flame-vortex interaction [36]. The strain rate is calculated using the following equation:

$$S = \frac{1}{2} \left( \frac{dv}{dx} + \frac{dU}{dy} \right) \quad (1)$$

where  $U$  and  $V$  are the radial and axial velocity, respectively. Figure 4.8a depicts the axial profiles of the centerline strain rate of the mean fields for different central nozzles and different mixing tube lengths. The results show that there is a series of positive and negative strain rate within the central flow region. The largest magnitude of the centerline strain rate is observed with N1S and N2L for  $X/D < 1$ . For  $X/D > 1$ , no significant difference was observed. Additionally, the instantaneous strain rate contour, in Fig. 4.8b, shows that the largest magnitude of the strain rate is observed within the outer and inner shear layers regions, where a series of positive and negative strain rates occurred. The occurrence of these highly strained regions along the inner and outer shear layers does not necessarily indicate the presence of PVC. These regions can interact with the flame front and hence causes flame wrinkling.

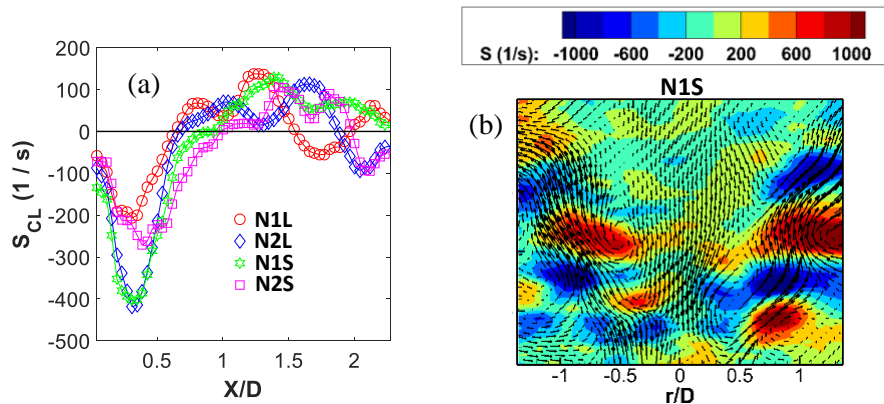


**Fig. 4.8.** (a) Axial profiles of the centerline strain rate of the mean flowfields for different central nozzles and different mixing tube lengths, and (b) typical instantaneous contour of strain rate for N1S.

It can be concluded from these results that the mean flow characteristics are not controlled by only the mixing tube length (and consequently the level of mixture inhomogeneity, turbulence intensity, and integral length scale inside the mixing tube), but also by the central nozzle geometry (inlet flow conditions into the mixing tube). The significance of the effect of the central nozzle

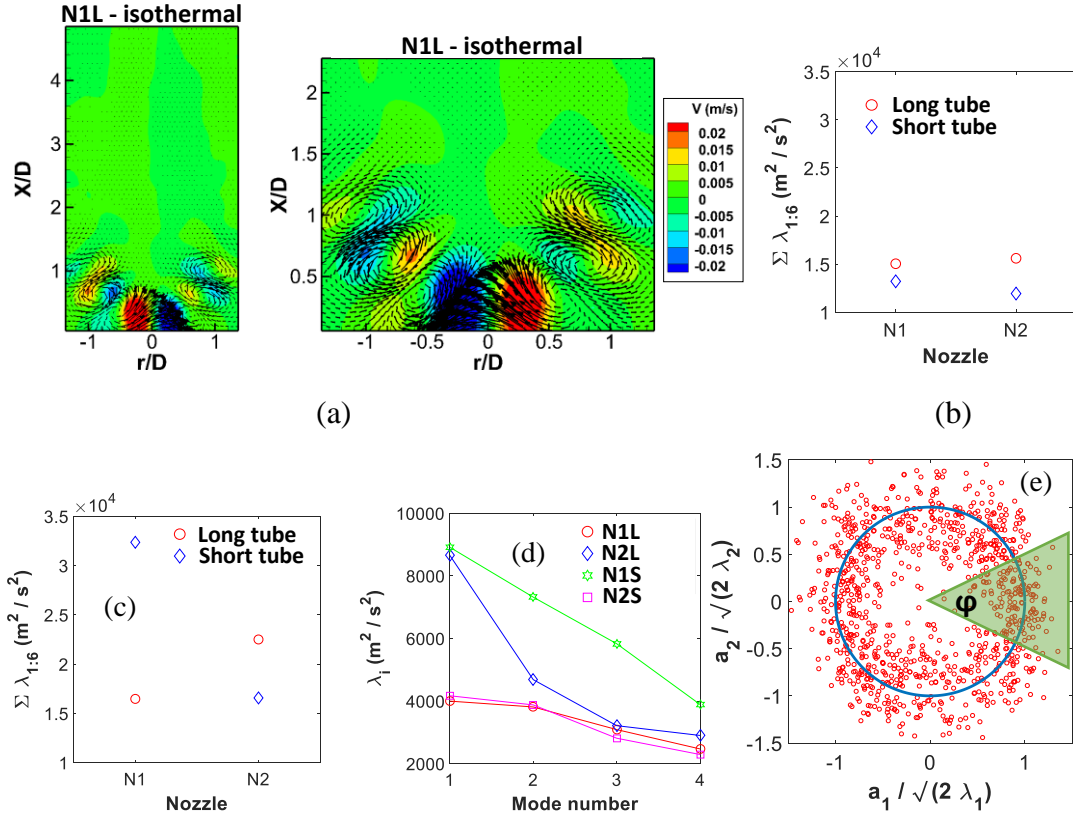
geometry is only obvious in the reacting flow cases. For instance, in the reacting flow case of N1, increasing the mixing length reduces turbulence intensity, strain rate in the near-field and the fluctuations of the CRZ size, whereas it increases the flame length in the far-field. However, the opposite scenario is observed with N2 in the reacting flow case. This is a clear indication of the significance of the central nozzle geometry on the flowfield in the reacting cases.

#### *4.4.2. POD of velocity field*

Proper orthogonal decomposition (POD) is applied to capture the dominant coherent structures. POD modes are calculated based on the method of snapshots described in [37]. Detailed description of POD procedure can be found elsewhere [25, 26]. Despite the fact that the sampling rate of the PIV setup used in the present study is low (10 Hz), POD still has the ability to capture coherent structures in the flowfield [38]. The POD is performed for the isothermal flow cases, which are used as a reference in order to confirm the occurrence of PVC in the isothermal cases for the studied burner configurations, and consequently determine the most appropriate ROI for POD procedure. As mentioned earlier in section 2.2, there are two ROIs; a large ROI for mean flowfield measurements and a smaller ROI for POD analysis (see Fig. 4.9a). It is found that cropping the ROI to include only the region that contains high amplitude coherent structures results in a higher modal energy [26]. After finding the locations of the more energetic structures, the raw PIV images are cropped into a smaller ROI that is restricted to these locations (see Fig. 4.9a). POD analysis is reprocessed using the new ROI, which provides more accurate analysis. The results confirm the presence of PVC as a dominant coherent structure in the flowfield of the isothermal cases. By comparing Fig. 4.9b,c, the coherent structures' energy is higher in the reacting cases than in the isothermal cases. Furthermore, the modal energy of the summation of the first six modes

in the isothermal cases is always proportional to the mixing tube length (Fig. 4.9b), which is not the trend in the reacting cases (Fig. 4.9c, N1). This can be attributed to the stronger effect of N1 flow with a short mixing length than that of a longer mixing length (i.e., low level of mixture inhomogeneity) (see Fig. 4.7). In addition, the centreline axial turbulence intensity is higher for a short mixing length, with the highest for N1S flow amongst all cases (see Fig. 4.5c). This is a demonstration of the role of coherent structures in enhancing turbulence intensity. Figure 4.9d depicts the modal energy of the first four POD modes. The results show that N1S followed by N2L exhibit the highest modal energy of the first four modes. In addition, increasing the mixing tube length when using N1 results in an approximately similar trend to that of N2 when decreasing the mixing tube length. This confirms the role of backflow intensity on the suppression of PVC amplitude, where a similar trend is observed in Fig. 4.5a.





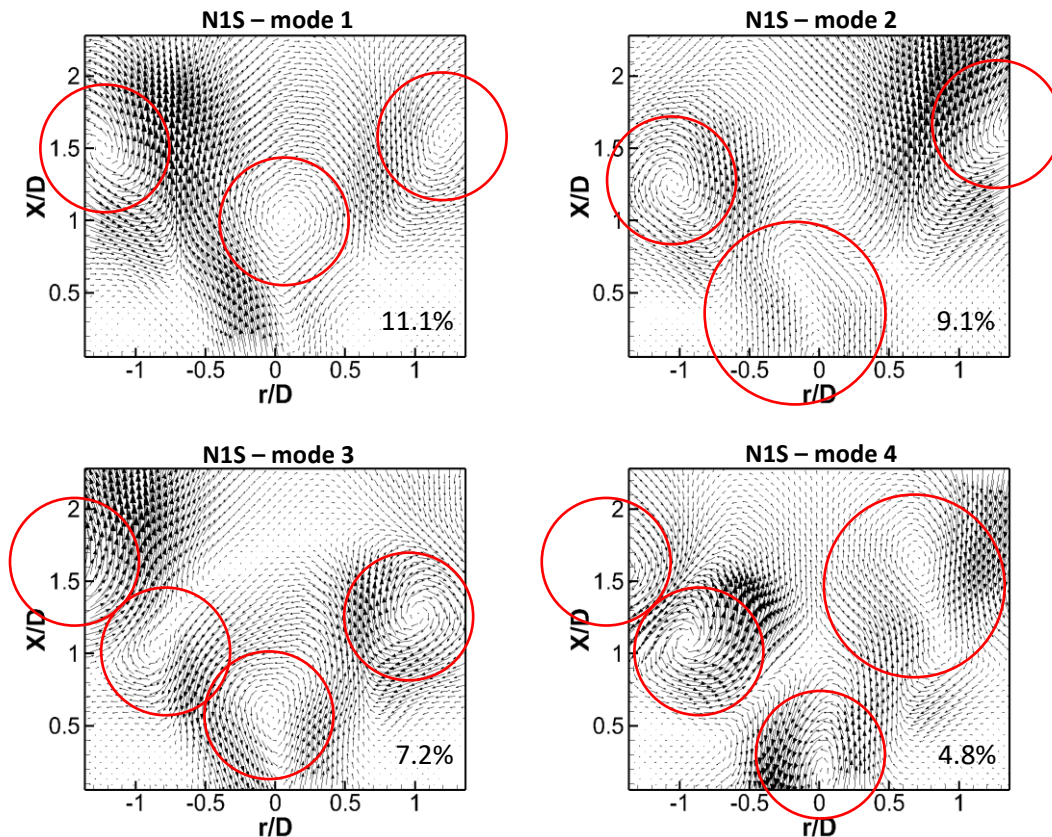
**Fig. 4.9.** (a) Typical large ROI and cropped ROI for an isothermal flow case with the first POD mode, POD modal energy of the summation of the first six modes for (b) isothermal and (c) reacting cases, (d) POD modal energy of the first four modes for different central nozzles and different mixing tube lengths, and (e) scatter plot of the normalized time coefficients of the first two POD modes with phase angle ( $\phi$ ).

Figure 4.9e depicts the scatter plot of the normalized time coefficients of the first POD mode versus those of the second POD modes for N1L for the isothermal flow case (shown as an example). The POD time coefficients  $a_{i1}$  and  $a_{i2}$  of the first two modes for each snapshot ( $i$ ) are calculated in order to determine the phase angle ( $\phi_i$ ) for each snapshot ( $i$ ) using the following equation:

$$\phi_i = \frac{1}{i} \ln \frac{a_{i1} + ia_{i2}}{\sqrt{a_{i1}^2 + a_{i2}^2}} \quad (2)$$

Eight phases are selected such that each phase covers 45 degrees; namely  $45^\circ \pm 22.5^\circ$ ,  $90^\circ \pm 22.5^\circ$ ,  $135^\circ \pm 22.5^\circ$ ,  $180^\circ \pm 22.5^\circ$ ,  $225^\circ \pm 22.5^\circ$ ,  $270^\circ \pm 22.5^\circ$ ,  $315^\circ \pm 22.5^\circ$ , and  $360^\circ \pm 22.5^\circ$ . The reconstructed velocity fields of the linear superposition of the first two POD modes are averaged

within a certain range of phase angles using Eq. (18) given in [26]. For example, the reconstructed velocity fields of the linear superposition of the first two POD modes whose phase angles are between  $-22.5^\circ$  and  $22.5^\circ$  are averaged to represent the phase-averaged reconstructed velocity field at  $\varphi = 360^\circ$ , as show in Fig. 4.9e. Before presenting the phase-averaged fields, it is useful to present the shapes of the first POD modes for, as an example, N1S (see Fig. 4.10a). This figure shows the shape of the most energetic coherent structures in the reacting flow cases. PVC is most likely suppressed in the first POD modes in the reacting flow cases. This is confirmed by observing the phase-averaged contours. Moreover, the PSD of the axial velocity fluctuations, which is extracted from the LDV measurements with a frequency resolution of 4 Hz, shows well-defined peaks in each test case (see Fig. 4.10b). The highest peak is associated to N1S, followed by N2L. The following sections provide further evidence of the suppression of PVC.



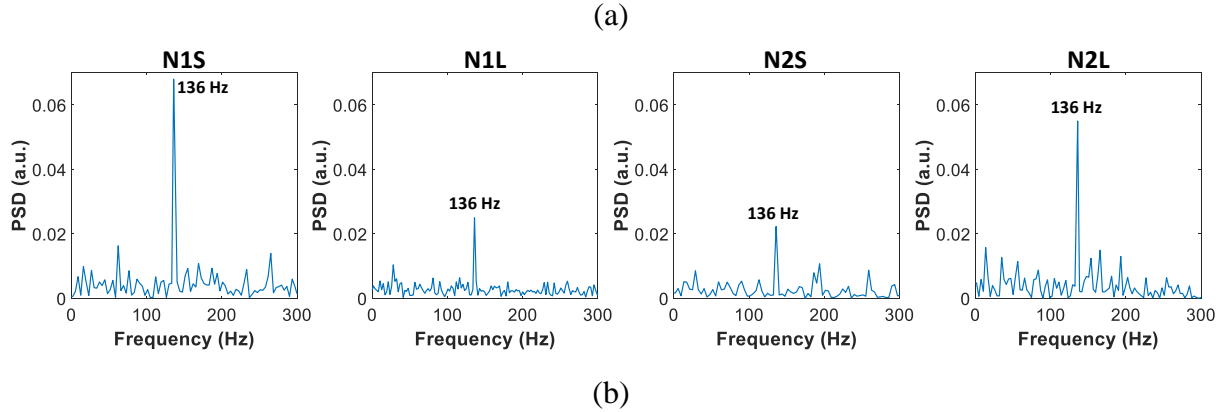


**Fig. 4.10.** (a) Representation of the shapes of the first four POD modes with the corresponding modal energy fraction for N1S (red circles represents the large turbulent structures), and (b) PSD of the axial velocity fluctuations, which shows the coherent structures' frequency, for different central nozzles and different mixing tube lengths.

Phase averaging is used to investigate the evolution and transition of coherent structures. It should be noted that the first two POD modes contribute by about 17.5% to 26.2% to the total turbulent kinetic energy depending on the test case. The phase-averaged vorticity fields shown in Fig. 4.11 reveal that shortening the mixing length results in the occurrence of coherent structures which are slightly more confined towards the central region as compared to those of a longer mixing length. When the vortical structures occur near the ORZ, flames are more prone to interact with the first longitudinal acoustic mode. This can increase the propensity for thermoacoustic instabilities [39]. On the other hand, the shear layers are well established for N2L at  $\phi = 45^\circ$  and  $180^\circ$ . This implies a change from a semi-solid cone V-shaped flame to a lifted flame, as demonstrated in the next section. The occurrence of smaller coherent structures is associated with N2S. It is reported that small scale vortical structures within the ISL and OSL can promote mixing, which, in turn, improve flame stability [40]. The largest coherent structures are generated with N1S, whereas the ones generated with N2L are more elongated. The phase-averaged contours exhibit somewhat similar shapes to that of PVC type II reported in [41]. Further PIV measurements in the horizontal (crosswise) plane was conducted to investigate the occurrence of this type (not

shown here for conciseness). These measurements, however, revealed no evidence of the presence of PVC in the horizontal plane in reacting flow cases.

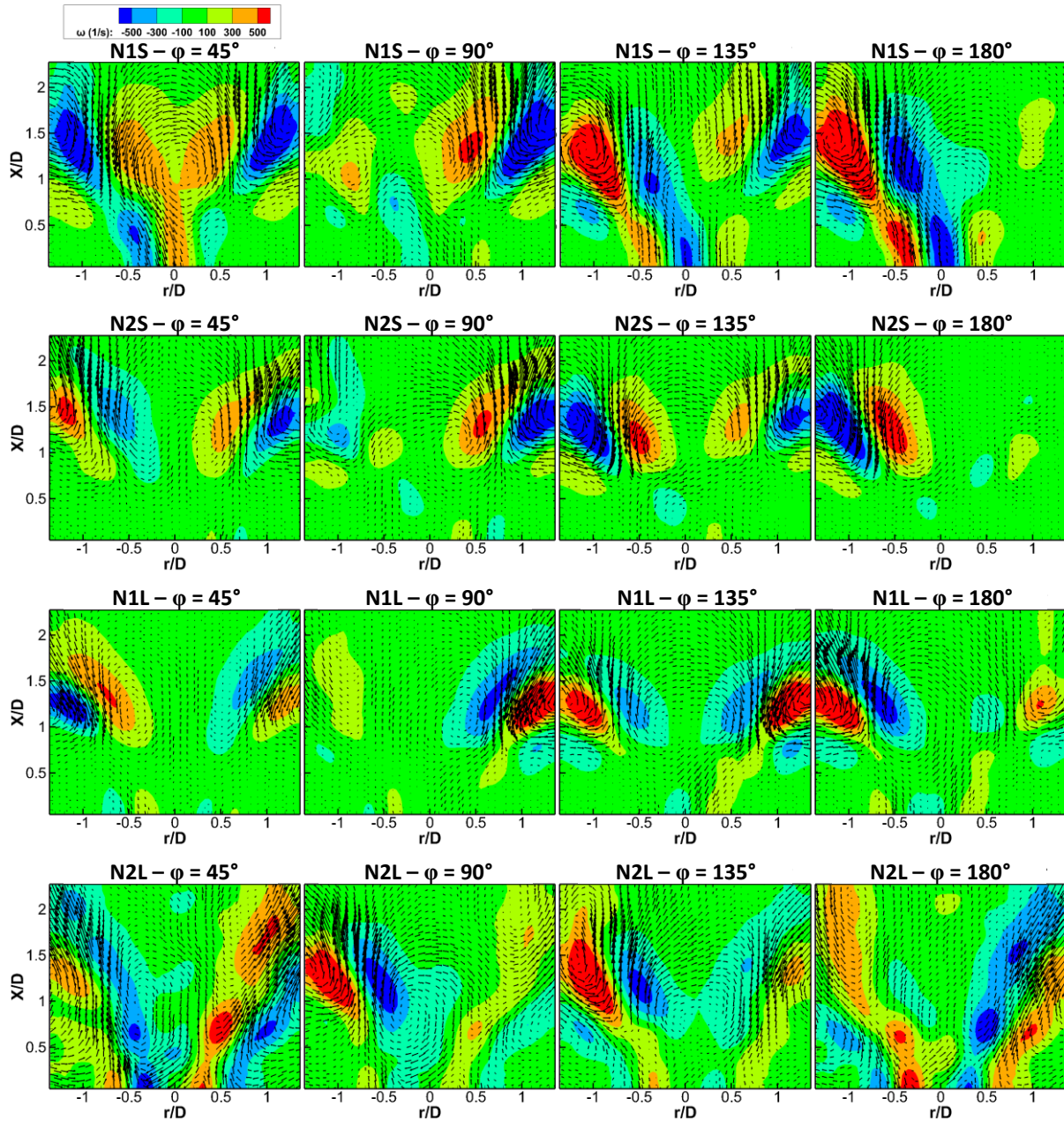


**Fig. 4.11.** Vorticity fields of the phase averaged linear superposition of the reconstructed first two POD modes for different central nozzles and different mixing tube lengths.

To confirm the results of POD, it is useful to determine the phase-averaged axial and radial velocity at constant  $X/D$ . The volumetric discharge can be calculated by integrating the axial

velocity over a plane at a fixed  $X/D$  [42]. Hence, the variation of the axial velocity with the phase angle at the same  $X/D$  can provide qualitative representation of the change of the volumetric discharge with the phase angle [10]. The results show a significant variation of the axial and radial velocity at, as an example,  $X/D = 0.45$  with the variation of the phase angle in one cycle of N1S and N2L (see N2L in Fig. 4.12). However, the radial profiles are much less discernable particularly at the positive axial velocity peaks of N1L and N2S (see N1L in Fig. 4.12). This indicates that cases with higher strength of coherent structures (N1S and N2L) experience higher oscillations in volumetric discharge with the variation of the phase angle.

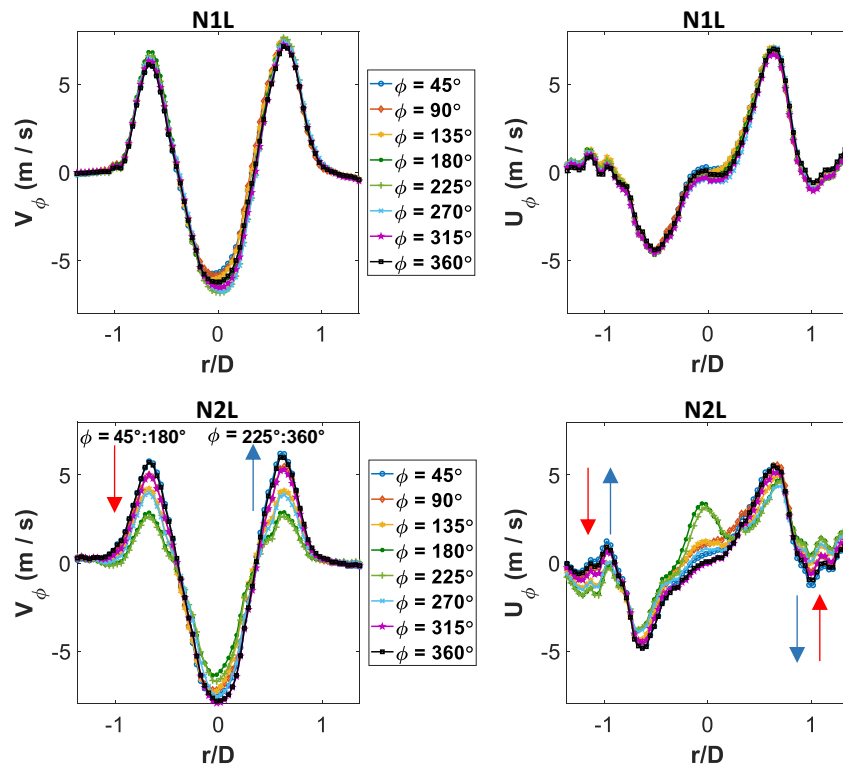


**Fig. 4.12.** Variation of the radial profiles of phase-averaged axial and radial velocity with phase angle at  $X/D = 0.45$  for N1L and N2L (red arrow represents the phase angles from  $45^\circ$  to  $180^\circ$  and blue arrow represents the phase angles from  $225^\circ$  to  $360^\circ$ ).

#### 4.4.3. *POD of flame front positions*

POD of the flame front positions is needed to reaffirm the effect of coherent structures on the flame front dynamics. Flame front dynamics in the OSL can contribute to flame-acoustic coupling. That is, the coupling between natural frequency of a burner/combustor and flame dynamics in the ORZ can lead to an overall instability [39]. The procedure of the POD of the flame front positions is similar to that of the POD of the velocity fluctuations, and the only difference is the input matrix that consists of the fluctuations of the flame front positions. Before discussing the POD results, it is useful to present flame luminescence images and flame mean progress variable. Figure 4.13a depicts the line-of-sight flame luminescence images for each test case. Images are acquired using a high-speed (Flowsense EO 4M) camera with an exposure time of  $48 \times 10^3 \mu\text{s}$  and an image resolution of  $32 \mu\text{m}/\text{pixel}$ . The images in Fig. 4.13a show that flames with long mixing tube experience higher jet divergence, which implies that these flames are more shifted outwardly/radially towards the ORZ. This implies a larger roll-up of these flames. For the mean progress variable calculation, the instantaneous flame colored images are converted into grayscale images (see Fig. 4.3), which are then converted to binary images with a suitable threshold. The binary image has only two pixel values; namely 0 (for black pixels, which represent the reactants), and 1 (for white pixels, which represent the flame region). After calculating the mean flame image, the pixels' value in the resultant image varies between 0 and 1, which represent the mean progress variable (c). The contours of the mean progress variable (c) in Fig. 4.13b confirm the trend observed in Fig. 4.13a. N1S exhibits the largest flame brush thickness, followed by N2L. However, N2S displays the smallest flame brush thickness.



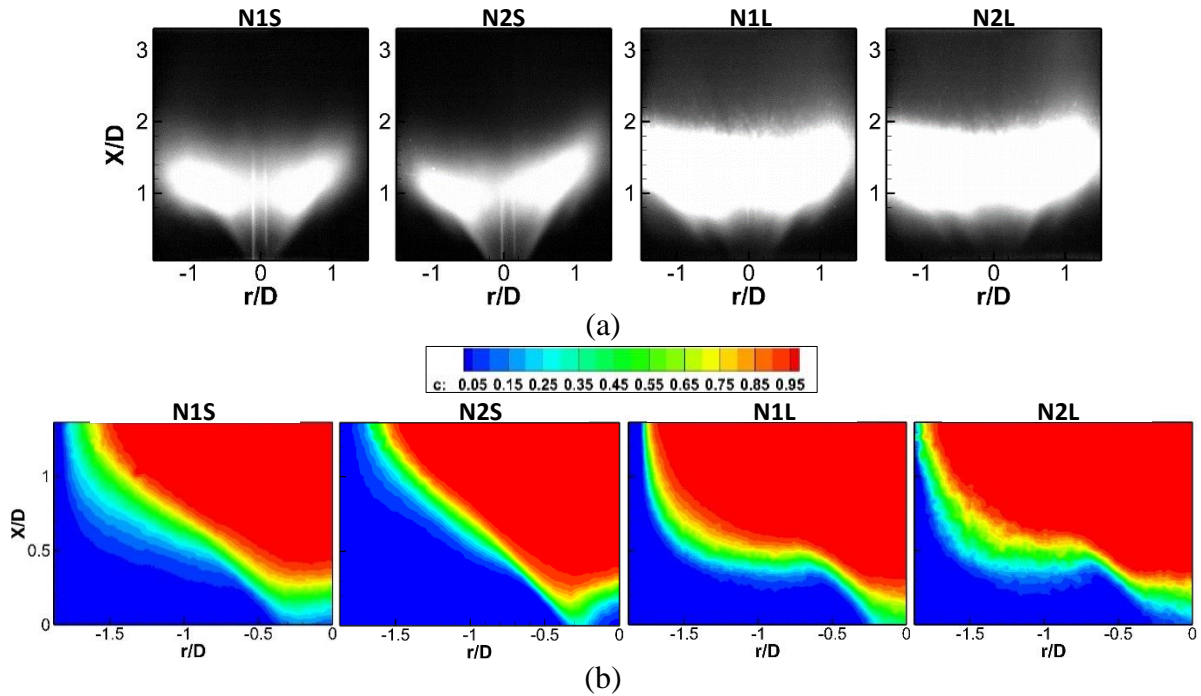


**Fig. 4.13.** (a) Flame luminescence images, and (b) contours of the mean progress variable,  $c$ , of the flame front positions for different central nozzles and different mixing tube lengths.

The POD modal energy distribution of the first six POD modes follows the same trend as that of the POD of the velocity field in Fig. 4.9c,d (see Fig. 4.14a). This suggests that there is a strong flame-vortex interaction. N1S exhibits the highest modal energy; whereas N2S has the lowest. By looking at Fig. 4.14b, the summation of the first six POD modes of N2S appears much lower than that of N1L which is not the case in Fig. 4.9c. This might suggest a weaker flame-vortex interaction for N2S.

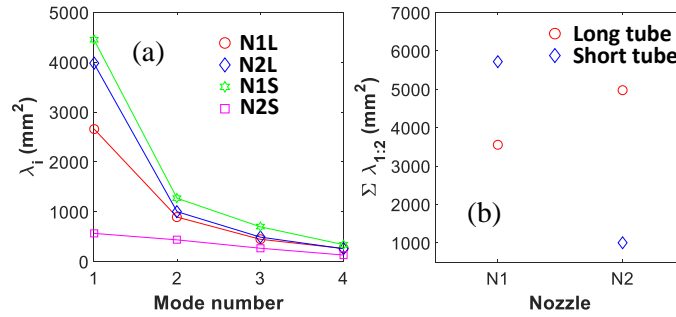


**Fig. 4.14.** (a) POD modal energy of the first four modes of flame front positions, and (b) POD modal energy of the summation of the first two modes for different central nozzles and different mixing tube lengths.

The time coefficient of the first POD mode is used to determine the peak frequency of the largest eddies. The power spectrum is estimated using Welch method at 400 Hz acquisition frequency with a resolution of 4 Hz. The results show the presence of a sharp spectral peak at 136 Hz for all test cases (see Fig. 4.15). The highest peak is observed for N1S and the lowest for N2S. This is an indication that the mixing tube length significantly affects the amplitude of the flame front fluctuations for both central nozzles, but with an opposite trend. That is, increasing the mixing tube length decreases the amplitude of flame front fluctuations when using N1, whereas it increases when using N2.

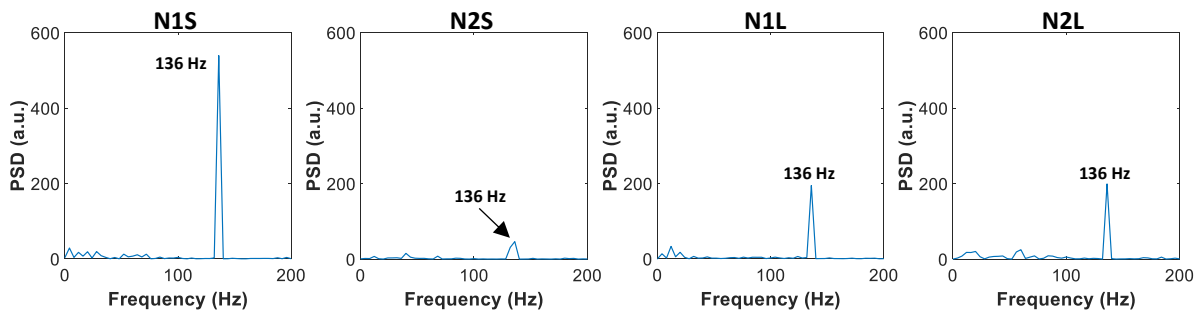
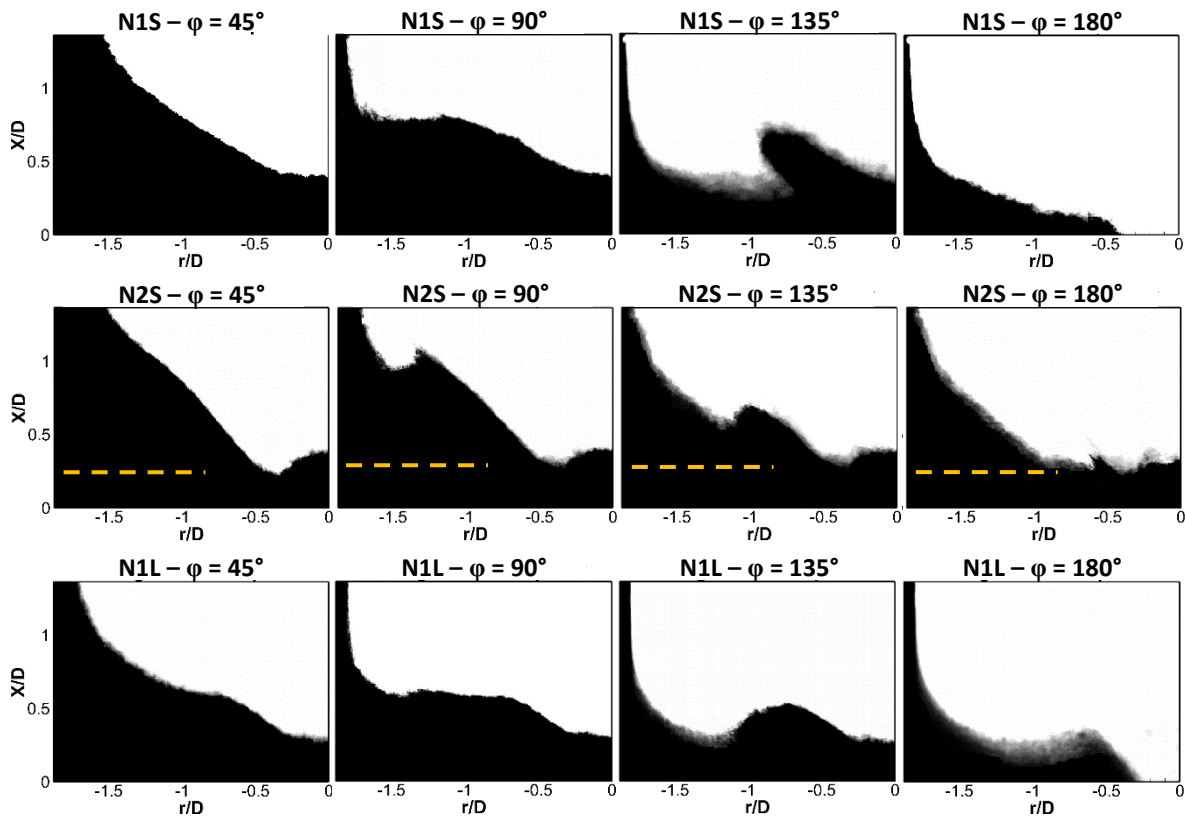


**Fig. 4.15.** PSD of time coefficients of the first POD mode for different central nozzles and different mixing tube lengths.



Flame dynamics within the OSL is better seen in the analysis of phase averaging of the flame front positions. The methodology of the phase averaging adopted here follows the same technique used in section 3.2 for the velocity field. The POD time coefficients of the first two modes are used for the calculation of the instantaneous phase angle. The reconstructed linear superposition of the first two POD modes of the flame front positions are obtained based on the binarized flame images. Note that the first two POD modes contribute to the total energy by 57.5% to 75.5% depending on the test case. Figure 4.16 depicts the variation of the flame front positions as a function of the phase angle for different central nozzle geometries and mixing tube lengths. The results show the appearance of a larger flame roll-up within the OSL as the mixing tube length increases. This is indicated by a large flame area within the ORZ. The results reveal that the flame of N2S is always stabilized at an approximately fixed X/D ( $X/D \approx 0.25$ ) for all phases of the dominant modes of the flame front fluctuations (see Fig. 4.16). This suggests that the flame of N2S does not reach upstream of the mixing tube exit and, hence, does not experience periodic flashback in any phase of the dominant modes. It is reported that fuel distribution/injection significantly affects the stability range of combustion oscillations [6]. Hence, it is noteworthy to mention that the measurement of flame stability limits show that N2S extends the stability limits (highest flame stability), while N1S significantly reduces the stability limits (the lowest flame stability). That is, the blowout occurs at a global equivalence ratio of 0.25 and a Reynolds number of 36440 for N2S, whereas it occurs at 0.29 and 30945, respectively, for N1S. The values of the other test cases fall within these ranges. In contrast to N1, the multi-orifice N2 nozzle supplies more homogeneous fuel distribution upstream and downstream of the dump plane. This outwardly radial shift of the flame front towards the confinement wall for N1S can cause high propensity of flame-vortex interaction. This can explain why N2S exhibits the lowest values of POD modal energy for both

velocity and flame front positions. Although increasing the mixing length (i.e., decreasing the level of mixture inhomogeneity) makes it susceptible to combustion instabilities for some burner configurations [17], it is not the case with N1. Increasing the mixing length for N1 creates more homogeneous fuel distribution upstream of the dump plane since the flow strength of N1 can be sustained over a longer axial distance than that of N2, which enhances macroscopic mixing [12]. It is noteworthy to mention that the line-of-sight method used to acquire the flame front position may also capture the flame front positions that are not on the same plane. This may lead to a different local flame wrinkling that could be measured by other techniques such as OH-PLIF, which consequently affects the accuracy of the measurement. However, the used technique in the present study can still provide a qualitative comparative analysis between the different test cases.



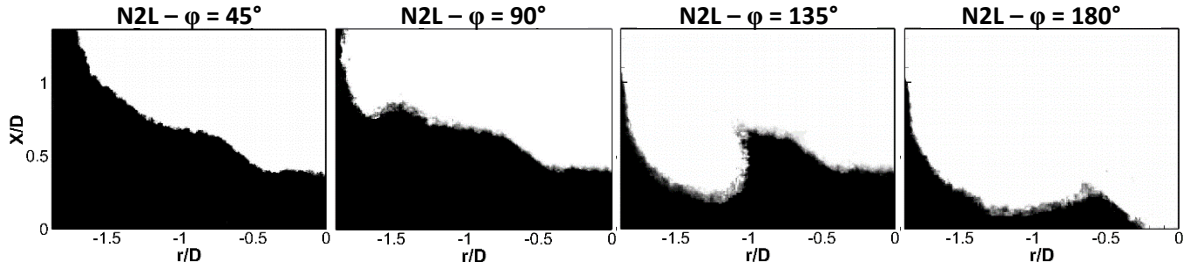


**Fig. 4.16.** Phase-averaged flame front positions of the reconstructed linear superposition of the first two POD modes for different central nozzles and different mixing tube lengths.

#### 4.4.4. Acoustics measurements

The PSD of the acoustic signal is determined using Welch method at 44100 Hz acquisition frequency with a resolution of 4 Hz (see Fig. 4.17). The results show two dominant peaks for each test case. The first peak indicates the possibility of a coupling between coherent structures and acoustics [23]. This is due to the fact that vortical structures can cause pressure fluctuations. The second peak corresponds to the first longitudinal mode of the combustor (the confinement tube starting from the dump plane). The frequency of the first longitudinal mode within the combustor/confinement is estimated as  $f_1 = \sqrt{kRT}/4L$ , where  $k$  is the specific heats ratio,  $R$  is the gas constant,  $T$  is the temperature of the working gas, and  $L$  is the length of the confinement quartz tube. The working gas is assumed to be air with a temperature ranging from 900 to 1400 K. The corresponding first longitudinal mode frequency estimated using this formula ranges from 752 to 890 Hz. The estimated values are not similar, however, they are approximately close to the observed frequency values of the first longitudinal mode in Fig. 4.17. This is because the assumed temperature is not similar to the actual one of the burner downstream of the dump plane. Also, the length is assumed to be that of the burner only (i.e., confinement tube length starting from the dump plane), while the acoustic waves can propagate within the mixing tube as well.

The results revealed that increasing the mixing tube length decreases the peaks' amplitude for N1, while it is the opposite trend with N2. It should be noted that the frequency of the first acoustic

peak coincides with that of the PSD of the first POD mode of the flame front positions and axial velocity fluctuations. This implies that N1S is more susceptible to the coupling between flame dynamics and acoustics.

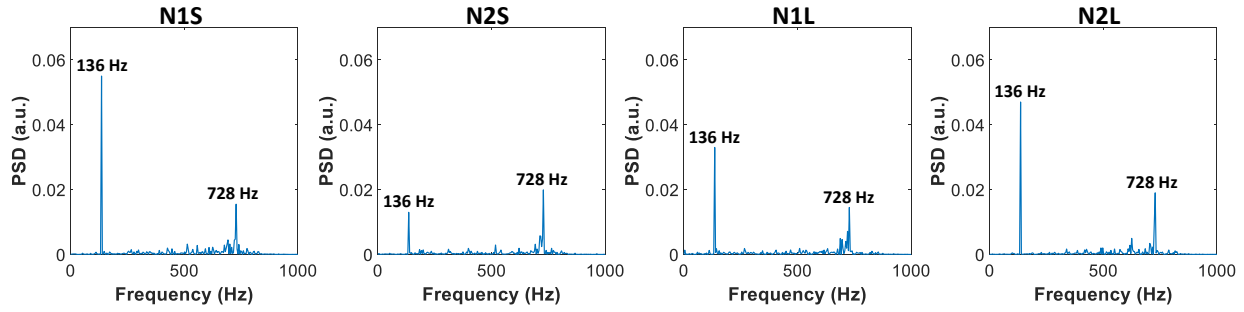


**Fig. 4.17.** PSD of the acoustic signal for different central nozzles and different mixing tube lengths.

It should be noted that the amplitude of instabilities increases when the coupling between the heat release and the acoustic fluctuations are in-phase [41][42], according to Rayleigh criterion. The results of the present study show that multi-orifice fuel injection can be the best alternative if the mixing length is short for two reasons. First, it can mitigate instabilities resulting from coherent structures by shifting the flame front away from the ORZ. Second, it is expected to enhance the fuel-air mixing downstream of the dump plane. In contrast to N2, using N1 with a shorter mixing length causes a greater interaction with the ORZ, which acts as an acoustic source. Increasing the mixing tube length and when using N1 significantly retains the effect of axial fuel injection, which promotes further suppression of coherent structures' amplitude.

## 4.5. Conclusions

This paper investigated the effect of the geometry of the fuel nozzle and the mixing tube length on the coherent structures, acoustics, and flame front dynamics within the OSL of confined

swirling PPFs. The results revealed that decreasing the mixing tube length does not always lead to a reduction in combustion instabilities. That is, the central nozzle geometry, which is used to mitigate PVC, is another important factor. The effect of the central nozzle geometry on the width of CRZ and flame length is evident. Injecting fuel through a multi-orifice nozzle instead of a single-orifice nozzle reduces its influence on the central flow which is further weakened by increasing the mixing tube length. This is attributed to smaller length scales produced by smaller orifices, and consequently makes the swirling airflow more dominant. The use of multi-orifice nozzle with shorter mixing lengths promote less interaction of the flame with the ORZ dynamics and hence leads to a better flame stability. On the other hand, using a single-orifice nozzle with a short mixing length promotes greater interaction of the flame with the ORZ, a condition favourable to combustion instabilities. However, using a single-orifice nozzle through long mixing lengths mitigate the occurrence of PVC and hence combustion instabilities. An optimum mixing length is achievable for reducing combustion instabilities while using a single-orifice nozzle. The cases that exhibit high coherent structures' amplitude are found to promote a significant variation of the volumetric discharge such as the cases of N1S and N2L, both of which contribute to the heat release rate fluctuations. In addition, the aforementioned cases (N1S and N2L) are found to be highly strained as a signature of high amplitude coherent structures.

In summary, the current study demonstrated the possibility of further mitigating coherent structures' amplitude at both short and long mixing lengths using a passive technique (i.e., varying the fuel nozzle geometry) which potentially can help mitigate combustion instabilities. In addition, using the axial mode of fuel entry to suppress PVC does not completely reduce coherent structures' amplitude as it depends on both the fuel nozzle geometry and the mixing tube length. Finally, further analysis of the heat release rate is required in order to investigate the coupling mechanism

between combustion dynamics and acoustics since the PSD peaks of the flame front fluctuations coincide with those of the acoustic fluctuations and velocity fluctuations.

#### 4.6. References

- [1] M. S. Mansour, A. M. Elbaz, and M. Samy, “The stabilization mechanism of highly stabilized partially premixed flames in a concentric flow conical nozzle burner,” *Exp. Therm. Fluid Sci.*, vol. 43, pp. 55–62, 2012.
- [2] S. K. Aggarwal, “Extinction of laminar partially premixed flames,” *Prog. Energy Combust. Sci.*, vol. 35, no. 6, pp. 528–570, 2009.
- [3] A. M. Steinberg, I. Boxx, M. Stöhr, C. D. Carter, and W. Meier, “Flow-flame interactions causing acoustically coupled heat release fluctuations in thermo-acoustically unstable gas turbine model combustor,” *Combust. Flame*, vol. 157, pp. 2250–2266, 2010.
- [4] P. Allison, J. Driscoll, and M. Ihme, “Acoustic Behavior of a Partially-Premixed Gas Turbine Model Combustor,” in *50th AIAA Aerospace Sciences Meeting including the New Horizons Forum and Aerospace Exposition*, 2012, p. AIAA 2012-0504 1-11.
- [5] D. Galley, S. Ducruix, F. Lacas, and D. Veynante, “Mixing and stabilization study of a partially premixed swirling flame using laser induced fluorescence,” *Combust. Flame*, vol. 158, pp. 155–171, 2011.
- [6] Y. Huang and V. Yang, “Dynamics and stability of lean-premixed swirl-stabilized combustion,” *Prog. Energy Combust. Sci.*, vol. 35, pp. 293–364, 2009.
- [7] M. Frederick, J. Dudash, B. Brubaker, and J. O. Connor, “Impact of Precessing Vortex Core Dynamics on Shear Layer Response in a Swirling Jet,” *J. Eng. Gas Turbines Power*, vol. 140, no. June, pp. 1–10, 2018.

- [8] S. Candel, "Combustion dynamics and control: progress and challenges," *Proc. Combust. Inst.*, vol. 29, pp. 1–28, 2002.
- [9] T. Lieuwen and V. Yang, "Combustion Instabilities: Basic Concepts," in *Combustion Instabilities In Gas Turbine Engines: Operational Experience, Fundamental Mechanisms, and Modeling*, Reston, VA.: American Institute of Aeronautics and Astronautics, 2006, pp. 3–26.
- [10] R. Sadanandan, M. Stöhr, and W. Meier, "Flowfield-flame structure interactions in an oscillating swirl flame : An investigation using phase resolved and simultaneous OH-PLIF and stereoscopic PIV measurements," *Combust. Explos. Shock Waves*, vol. 45, pp. 518–529, 2009.
- [11] N. Syred, "A review of oscillation mechanisms and the role of the precessing vortex core (PVC) in swirl combustion systems," *Prog. Energy Combust. Sci.*, vol. 32, no. 2, pp. 93–161, 2006.
- [12] C. Mayer, J. Sangl, T. Sattelmayer, T. Lachaux, and S. Bernero, "Study on the operational window of a swirl stabilized syngas burner under atmospheric and high pressure conditions," *J. Eng. Gas Turbines Power*, vol. 134, pp. 1–11, 2012.
- [13] N. Syred and J. M. Beer, "Combustion in Swirling Flows : A Review," *Combust. Flame*, vol. 23, pp. 143–201, 1974.
- [14] W. Fick, "Ph.D Thesis," Cardiff University, 1968.
- [15] M. S. Mansour, "A study of turbulent partially premixed flames based on simultaneous imaging of velocity field and OH radical," *Combust. Sci. Technol.*, vol. 174, no. 2, pp. 47–78, 2002.
- [16] S. Y. Lee, S. Seo, J. C. Broda, S. Pal, and R. J. Santoro, "An experimental estimation of

- mean reaction rate and flame structure during combustion instability in a lean premixed gas turbine combustor,” *Proc. Combust. Inst.*, vol. 28, no. 1, pp. 775–782, 2000.
- [17] S. Joo, J. Yoon, J. Kim, M. Lee, and Y. Yoon, “NO<sub>x</sub> emissions characteristics of the partially premixed combustion of H<sub>2</sub>/CO/CH<sub>4</sub> syngas using artificial neural networks,” *Appl. Therm. Eng.*, vol. 80, pp. 436–444, 2015.
- [18] S. Bade, M. Wagner, C. Hirsch, T. Sattelmayer, and B. Schuermans, “Influence of Fuel-Air Mixing on Flame Dynamics of Premixed Swirl Burners,” *Proc. ASME Turbo Expo*, vol. GT2014, p. 25381, 2014.
- [19] G. Li and E. J. Gutmark, “Geometry effects on the flow field and the spectral characteristics of a triple annular swirler,” *Proc. ASME Turbo Expo*, vol. GT2004, no. 38799, pp. 1–10, 2003.
- [20] C. O. Iyogun and M. Birouk, “Effect of Fuel Nozzle Geometry on the Stability of a Turbulent Jet Methane Flame,” *Combust. Sci. Technol.*, vol. 180, no. 12, pp. 2186–2209, 2008.
- [21] C. O. Iyogun, M. Birouk, and J. a. Kozinski, “Experimental investigation of the effect of fuel nozzle geometry on the stability of a swirling non-premixed methane flame,” *Fuel*, vol. 90, no. 4, pp. 1416–1423, 2011.
- [22] C. O. Iyogun and M. Birouk, “Effect of sudden expansion on entrainment and spreading rates of a jet issuing from asymmetric nozzles,” *Flow, Turbul. Combust.*, vol. 82, no. 3, pp. 287–315, 2009.
- [23] T. Providakis, L. Zimmer, P. Scouflaire, and S. Ducruix, “Characterization of the acoustic interactions in a two-staged multi-injection combustor fed with liquid fuel,” *J. Eng. Gas Turbines Power*, vol. 134, no. 11, p. 111503, 2012.



- [24] K. O. Smith, F. R. Kurzynske, and L. C. Angello, "Experimental Evaluation of Fuel Injection Configurations for a Lean-Premixed Low NO<sub>x</sub> Gas Turbine Combustor," *ASME Pap. 1987-GT-0141*, pp. 1–9, 1987.
- [25] M. M. A. Ahmed and M. Birouk, "Effect of fuel Nozzle Geometry and Airflow Swirl on the Coherent Structures of Partially Premixed Methane Flame under Flashback Conditions," *Exp. Therm. Fluid Sci.*, vol. 99, pp. 304–314, 2018.
- [26] M. Stöhr, R. Sadanandan, and W. Meier, "Phase-resolved characterization of vortex-flame interaction in a turbulent swirl flame," *Exp. Fluids*, vol. 51, no. 4, pp. 1153–1167, 2011.
- [27] L. Zheng and Y. Zhang, "High Speed Digital Imaging for Flame Studies: Potentials and Limitations," *Energy Procedia*, vol. 66, no. 0, pp. 237–240, 2015.
- [28] H. Huang and Y. Zhang, "Flame colour characterization in the visible and infrared spectrum using a digital camera and image processing," *Meas. Sci. Technol.*, vol. 19, no. 8, p. 085406 (9pp), 2008.
- [29] D. Ghimire and J. Lee, "Color Image Enhancement in HSV Space Using Nonlinear Transfer Function and Neighborhood Dependent Approach with Preserving Details," in *2010 Fourth Pacific-Rim Symposium on Image and Video Technology*, 2010, pp. 422–426.
- [30] S. Taamallah, Z. A. LaBry, S. J. Shanbhogue, M. A. M. Habib, and A. F. Ghoniem, "Correspondence Between 'Stable' Flame Macrostructure and Thermo-acoustic Instability in Premixed Swirl-Stabilized Turbulent Combustion," *J. Eng. Gas Turbines Power*, vol. 137, pp. 071505-1–12, 2015.
- [31] O. Lucca-Negro and T. O'Doherty, "Vortex breakdown: A review," *Prog. Energy Combust. Sci.*, vol. 27, pp. 431–481, 2001.
- [32] I. Hernández, G. Staffelbach, T. Poinso, J. C. Román Casado, and J. B. W. Kok, "LES and

- acoustic analysis of thermo-acoustic instabilities in a partially premixed model combustor,” *Comptes Rendus - Mec.*, vol. 341, no. 1–2, pp. 121–130, 2013.
- [33] S. Terhaar, B. Ćosić, C. O. Paschereit, and K. Oberleithner, “Suppression and excitation of the precessing vortex core by acoustic velocity fluctuations: An experimental and analytical study,” *Combust. Flame*, vol. 172, pp. 234–251, 2016.
- [34] S. Terhaar, K. Oberleithner, and C. O. Paschereit, “Key parameters governing the precessing vortex core in reacting flows: An experimental and analytical study,” *Proc. Combust. Inst.*, vol. 35, pp. 3347–3354, 2015.
- [35] S. B. Pope, *Turbulent Flows*. Cambridge University Press, 2000.
- [36] A. M. Steinberg and J. F. Driscoll, “Straining and wrinkling processes during turbulence – premixed flame interaction measured using temporally-resolved diagnostics,” *Combust. Flame*, vol. 156, no. 12, pp. 2285–2306, 2009.
- [37] L. Sirovich, “Turbulence and the dynamics of coherent structures,” *Quart Appl Math*, vol. 45, pp. 561–590, 1987.
- [38] S. Kheirkhah, Ö. L. Gülder, G. Maurice, F. Halter, and I. Gökalp, “On periodic behavior of weakly turbulent premixed flame corrugations,” *Combust. Flame*, vol. 168, pp. 147–165, 2016.
- [39] J. Meadows and A. K. Agrawal, “Time-resolved PIV of lean premixed combustion without and with porous inert media for acoustic control,” *Combust. Flame*, vol. 162, pp. 1063–1077, 2015.
- [40] R. Sadanandan, M. Stöhr, and W. Meier, “Simultaneous OH-PLIF and PIV measurements in a gas turbine model combustor,” *Appl. Phys. B*, vol. 90, pp. 609–618, 2008.
- [41] S. Terhaar, T. G. Reichel, C. Shrodingner, L. Rukes, and C. O. Paschereit, “Vortex

breakdown types and global modes in swirling combustor flows with axial injection,” *J. Propuls. power*, vol. 31, no. 1, pp. 219–229, 2015.

- [42] M. Stöhr, R. Sadanandan, and W. Meier, “Experimental study of unsteady flame structures of an oscillating swirl flame in a gas turbine model combustor,” *Proc. Combust. Inst.*, vol. 32, pp. 2925–2932, 2009.

## Chapter 5: Conclusions and Recommendations for Future Work

This chapter presents the major findings of the present study, and some recommendations for future studies.

### 5.1. Research summary

The present study experimentally investigated the effect of burner geometry (i.e., fuel nozzle geometry, mixing tube length, swirl number) on coherent structures, acoustics, and flashback of unconfined and confined PPFs. The main findings and concluding remarks of the present study are summarized below.

a) Effect of fuel nozzle geometry on coherent structures and flashback of unconfined PPFs:

- At fixed swirl number of the co-airflow, polygonal orifice nozzles are found to promote flow characteristics favorable to flame stability owing to their lowest coherent structures' amplitude and frequency inside the mixing tube as compared to those of single-orifice and multi-orifice nozzles.
- Similarly to what is observed with coherent structures' amplitude and frequency, polygonal orifice nozzles generate the smallest mean flashback region inside the mixing tube at constant swirl number of the co-airflow.
- Flashback is found to manifest in the case of all fuel nozzle geometries at high swirl number, whereas only the seven-orifice nozzle exhibits flame flashback at low swirl number and equivalence ratio. This is attributed to the fact that the seven-orifice nozzle does not have a strong effect on the centerline region of the flow inside the mixing tube

and also owing to its improved fuel-air mixing caused by injecting the rich fuel mixture through a number of orifices.

- In addition to the nozzle geometry, flashback is found to depend on coherent structures (PVC or vortex shedding) that are controlled by the equivalence ratio and swirl number.

This is a confirmation of the interaction between coherent structures and flashback.

This study is possibly the first one that reveals the role of nozzle geometry on the association between flashback and coherent structures' amplitude and frequency.

b) Relationship between fuel nozzle geometry and coherent structures' suppression for unconfined PPFs:

- Changing fuel nozzle geometry is found to cause a significant effect on the mean flowfield and coherent structures' amplitude, where multi-orifice nozzles exhibit better characteristics of flame stability as compared to single-orifice nozzles.
- Multi-orifice nozzles are found to promote the coherent structures' suppression. For instance, in contrast to multi-orifice nozzles, single-orifice nozzles generate larger integral length scales and higher turbulence intensity inside and outside the mixing tube.
- Moreover, in contrast to multi-orifice nozzles, stronger and more elongated coherent structures inside the mixing tube, which are convected downstream of the mixing tube exit and resulted in higher coherent structures' amplitude, are associated with single-orifice nozzle. These characteristics are detrimental to flame stability.
- Multi-orifice nozzles, on the other hand, exhibit lower degree of asymmetry and rms of the flame front positions as compared to single-orifice nozzles, indicating weaker signature

of the coherent structures. This is attributed to a weaker flame-vortex interaction and a more stable flames when using multi-orifice nozzles.

This investigation demonstrated that suppression of coherent structures' amplitude via the use of axial mode of fuel injection is also dependent on the central nozzle geometry.

c) Relationship between fuel nozzle geometry, coherent structures, and acoustics for confined PPFs:

- Both the central nozzle geometry and mixing tube length are found to affect the mean field characteristics (i.e., integral length scale, rms of the CRZ width, centerline strain rate), volumetric discharge oscillations, coherent structures' amplitude, flame front dynamics, and acoustics behavior.
- The amplitude of coherent structures is found to depend not only on the mixing tube length. It is found that increasing the mixing tube length decreases the amplitude of coherent structures and acoustics of single-orifice nozzle; whereas it is the opposite trend for multi-orifice nozzle.
- Employing multi-orifice nozzle in a short mixing tube is found to be the optimum configuration with respect to the suppression of coherent structures and acoustics fluctuations. To the author's best knowledge, only a few studies in literature investigated the combined effect of mixing tube length and fuel nozzle geometry on coherent structures' amplitude and acoustic modes for confined PPFs.

To conclude, this study focused on the role of a passive technique to mitigate flashback for unconfined PPFs, acoustics for confined PPFs, and coherent structures' amplitude for both

unconfined and confined PPFs. This study revealed that flashback, coherent structures' amplitude, acoustics of PPFs can be controlled/suppressed by varying not only the mixing tube length but also the fuel nozzle geometry. This, in fact, is advantageous as it can lead to extending the operating conditions of a stable PPF.

## **5.2. Recommendations for future work**

Following the conclusions presented above, some recommendations for further research are presented as follows:

- 1- According to Rayleigh criterion, combustion instability intensifies when heat release rate and acoustics oscillations are in-phase and coupled. However, the collected data from the present burner configuration could not reveal any information about the coupling between the heat and acoustic oscillations and whether they are in-phase or not. Therefore, simultaneous PIV/PLIF measurements should be conducted in order to acquire information about the heat release rate contours and to further provide insight into flame-vortex interaction. Some recent studies utilized Hilbert transform to detect local phase difference between pressure oscillations and heat release rate [1, 2] based on acoustics and PLIF measurements. That is, flame regions which exhibit a matching between the phases of pressure oscillations and heat release rate (i.e., local phase difference is approximately zero) can be the main source for combustion instabilities. This methodology of using Hilbert transform to detect local phase difference can be useful for investigating these regions and, consequently develop strategies to mitigate related combustion instabilities.
- 2- Since one of the main parameters contributing to thermoacoustic oscillations inside a combustor is acoustic oscillations, it is essential to damp acoustic waves in order to

promote more stable and less noisy combustion [3]. Several passive techniques to damp acoustic waves were reported in the literature such as baffles, Helmholtz resonators, quarter-wave tubes, and porous inert media (PIM). The use of PIM in premixed confined swirling flames as an acoustic damper is introduced in [5]. Baffles damp transverse acoustic oscillations with the damping effect increases as the baffles length increases [4]. The use of baffles with swirling flames are rarely employed (e.g., [6]), especially in the case of PPFs. Furthermore, there exist no study which utilized PIM for PPFs. This might be due to the complexity in thermophysics, transport, and heat transfer process that makes flame stabilization inside a PIM challenging [7]. This could be complicated since local equivalence ratio of PPFs is not uniform throughout the flowfield. Therefore, more suitable acoustic dampers for PPFs with a well-defined geometry and inlet and outlet conditions should be developed. This might be achieved via a combination of baffles and perforated plates.

- 3- The exhaust nozzle downstream of the confinement of a dump combustor can control acoustic waves inside a combustor since the choked exhaust nozzle can reflect the incident acoustic waves and act as an acoustically rigid surface [3]. Therefore, varying the exhaust nozzle shape could alter the behavior of acoustic waves. It was stated that eccentric exhaust can mitigate the formation of PVC and alter the acoustic modes of a combustor [8]. Moreover, the conical inlet (or quarl) of a combustor can also damp large eddies by guiding the flow expansion where no ORZ is present in the flowfield [8]. Conical elliptically shaped burners also mitigate combustion instabilities via controlling large-scale coherent structures [3]. The suppression of coherent structures of swirling PPFs under the effect of different partial premixing levels using a conical expansion inlet into a combustor has



rarely been investigated [9]. Thus, this configuration is worthwhile testing in order to investigate the relationship between coherent structures, acoustics and mixing in the absence of ORZ.

- 4- Changing the fuel type can alter turbulent flame speed and, hence, flashback behavior. Moreover, flame kernel propagation speed, which affects flame stability [1], of PPFs is dependent on the fuel type within a certain range of flow Reynolds number. In some cases auto-ignition, which was found to match the center of PVC, can be the cause of flame kernels. This may suggest an interplay between fuel type and coherent structures. Consequently, the results of the present thesis may only apply to methane PPFs. Thus, it is recommended to vary the fuel type in order to draw more general conclusions.

### 5.3. References

- [1] S. Kheirkhah, J. D. M. Cirtwill, P. Saini, K. Venkatesan, and A. M. Steinberg, “Dynamics and mechanisms of pressure, heat release rate, and fuel spray coupling during intermittent thermoacoustic oscillations in a model aeronautical combustor at elevated pressure,” *Combust. Flame*, vol. 185, pp. 319–334, 2017
- [2] W. Culler, X. Chen, J. Samarasinghe, S. Peluso, D. Santavicca, and J. O’Connor, “The effect of variable fuel staging transients on self-excited instabilities in a multiple-nozzle combustor,” *Combust. Flame*, vol. 194, pp. 472–484, 2018
- [3] Y. Huang and V. Yang, “Dynamics and stability of lean-premixed swirl-stabilized combustion,” *Prog. Energy Combust. Sci.*, vol. 35, no. 4, pp. 293–364, 2009.
- [4] D. You, D.D. Ku, V. Yang, “Acoustic waves in baffled combustion chamber with radial and circumferential blades,” *J. Propuls. Power* 29 (6) (2013) 1-15.

- [5] J. Meadows, A.K. Agrawal, “Time-resolved PIV of lean premixed combustion without and with porous inert media for acoustic control,” *Combust. Flame* 162 (2015) 1063-1077.
- [6] J.R. Dawson, N.A. Worth, “The effect of baffles on self-excited azimuthal modes in an annular combustor,” *Proc. Combust. Inst.* 35 (2015) 3283-3290.
- [7] S. Sobhani, B. Haley, D. Bartz, J. Dunnmon, J. Sullivan, M. Ihme, “Investigation of lean combustion stability, pressure drop, and material durability in porous media burners.” ASME. Turbo Expo: Power for Land, Sea, and Air (2017) V05CT17A001.
- [8] N. Syred, “A review of oscillation mechanisms and the role of the precessing vortex core (PVC) in swirl combustion systems,” *Prog. Energy Combust. Sci.*, vol. 32, no. 2, pp. 93–161, 2006.
- [9] S. Bade, M. Wagner, C. Hirsch, T. Sattelmayer, and B. Schuermans, “Influence of Fuel-Air Mixing on Flame Dynamics of Premixed Swirl Burners,” *Proc. ASME Turbo Expo*, vol. GT2014, p. 25381, 2014.

## Appendix A: Error Analysis and Calibration

### A.1. Uncertainty in the mean and rms velocity

The axial mean and rms velocity, as an example, are calculated using the follow equations, respectively:

$$\bar{V} = \frac{\sum_{i=1}^N V}{N} \quad \text{A.1}$$

$$v' = \sqrt{\frac{\sum_{i=1}^N (V - \bar{V})^2}{N}} \quad \text{A.2}$$

The uncertainty in the mean velocity is calculated based on the student's t-distribution and rms velocity.

Figure A.1 depicts the students t-distribution for  $N = 1000$  showing the rejection regions. For this number of samples,  $t_{critical} = 1.96$ . The equations used to calculate the 95% confidence interval for the mean velocity are as follows:

$$\bar{V} - t_{critical} \frac{v'}{\sqrt{N}} \leq X_m \leq \bar{V} + t_{critical} \frac{v'}{\sqrt{N}} \quad \text{A.3}$$

$$t_{critical} = t(\alpha_c/2, N) \quad \text{A.4}$$

where  $\alpha_c = 1 - C_i$  where  $C_i = 0.95$

This error is related to the random error (precision error). Another error that is related to the inaccuracy of the measurement method is called the bias error. This error is a systematic error and it is repeated for all samples. The bias error is calculated using the following:

$$B = \sqrt{\sum_{j=1}^{N_{source}} B_j^2} \quad \text{A.5}$$

The total error is calculated using the following equation:

$$e = \sqrt{B^2 + P^2} \quad \text{A.6}$$

where

$$P = t_{critical} \frac{v'}{\sqrt{N}} \quad \text{A.7}$$

The aforementioned procedure is applied for the data of PIV, LDV, and flame front positions. In PIV, for example, the maximum uncertainty in the mean velocity was found to be  $\pm 0.4$  m/s.

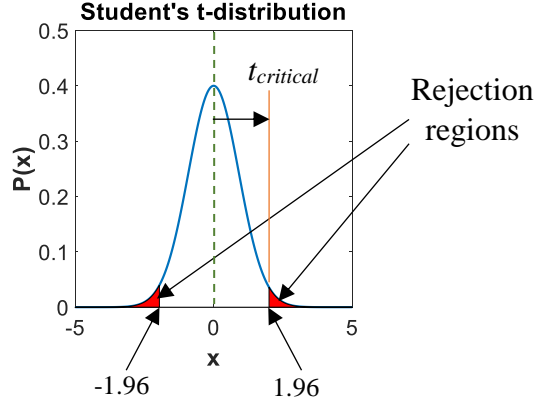


**Fig. A.1.** Student's t-distribution showing the rejection regions and the  $t_{critical}$ .

The uncertainty in the rms velocity is calculated based on Chi-square distribution (see Fig. A.2).

The 95% confidence interval for rms velocity is calculated using the following equations:

$$\sqrt{\frac{v'^2 N}{\chi_{p1}^2}} \leq X_{rms} \leq \sqrt{\frac{v'^2 N}{\chi_{p2}^2}} \quad \text{A.8}$$

Where

$$\chi_{p1}^2 \approx (1/2)[p_1 + \sqrt{2(N-1) - 1}]^2 \quad \text{A.9}$$

where  $p_1 = (1/2)(1 - C_i)$

$$\chi_{p2}^2 \approx (1/2)[p_2 + \sqrt{2(N-1) - 1}]^2 \quad \text{A.10}$$

where  $p_2 = (1/2)(1 + C_i)$

Accordingly, the maximum uncertainty in the rms velocity was found to be approximately 4%.

Furthermore, it is important to examine whether the 1  $\mu\text{m}$   $\text{TiO}_2$  particles faithfully track the smallest flow structures or not, which is essential for Mie scattering and QLS techniques. For that purpose, Stokes number is calculated based on the highest centerline turbulent kinetic energy and integral length scale in Table 3.1. The Stokes number is calculated using the following expression:

$$Sk = \frac{\tau_P}{\tau_F} \quad \text{where} \quad \tau_P = \rho_P \frac{d_p^2}{18\mu_F} \quad \text{and} \quad \tau_F = \frac{\Lambda_L}{u_o} \quad \text{A.11}$$

where  $\tau_P$  is particle response time (s),  $\tau_F$  is integral time scale (s),  $d_P$  is mean particle diameter (m),  $\rho_P$  is particle density ( $\sim 4260 \text{ kg/m}^3$ ),  $\mu_F$  is the fluid dynamic viscosity ( $\sim 1.836 \times 10^{-5} \text{ kg/m}\cdot\text{s}$ ),  $\Lambda_L$  is integral length scale (m), and  $u_o$  is velocity scale (m/s). The resultant Stokes number ranges between 0.007 and 0.009 which is much smaller than the threshold limit (i.e.,  $Sk \approx 0.1$ ).

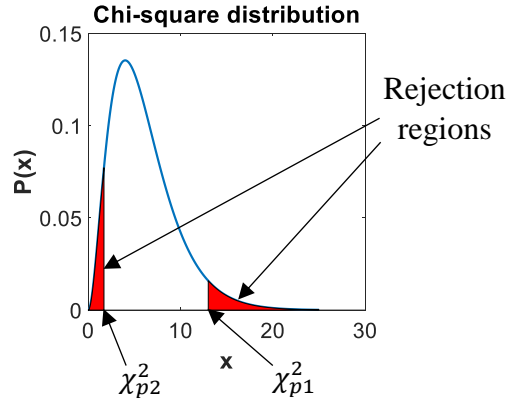


**Fig. A.2.** Chi-square distribution showing the rejection regions with the corresponding variables for  $N = 7$  as an example.

In order to deliver the methane, swirling air, and central air, three flow meters are used. Brooks SLA5853, and two Matheson FM-1050 flow meters are employed for delivering the swirling airflow, and both central air and methane, respectively. The accuracy of Brooks SLA5853 is found to be 1% whereas the accuracy of the two Matheson FM-1050 flow meters is 2% based on using reference scale. Therefore, these types of flow meters yield an error in the employed equivalence ratio of  $\pm\sqrt{3}$  based on the RSS of the accuracies of the three flow meters.

## A.2. Calibration

To minimize the bias error, calibration should provide a relatively high-resolution image and a correction for image distortion due to the presence of a transparent optical access such as the quartz

mixing tube or the quartz confinement. To capture smaller FOV without losing regions that have important flow field details, it is essential to keep the resolution as high as possible. A calibration board is used to estimate the spatial resolution in units of  $\mu\text{m}/\text{pixel}$ . The calibration board consists of black dots on a white background (see Fig. A.3a). Each dot has a diameter of 1 mm while the spacing between dots is 2 mm. According to Snell's law, when the light passes through a medium with a higher refractive index ( $n_{ref}$ ), the light is refracted and propagates through the medium with an angle of refraction less than the incidence angle. Therefore, the image on the CCD array in the camera is dissimilar to the physical positions inside the confinement (see Fig. A.3c). The refractive index of the fused silica depends on the wavelength of light ( $\lambda_w$ ) and varies from 1.49 to 1.45 within the visible range limits of 300 – 700 nm. The PIV laser, with a wavelength of 532 nm, yields a refractive index of fused silica of approximately 1.46. This can result in different flame front positions depending on the color of the flame. However, the difference in the refraction angles between the flame colors obtained in the present study is negligible and the resulting difference between the positions on the CCD array is less than the image resolution. Nonetheless, an image dewarping procedure is still mandatory when imaging flames inside the quartz mixing tube or quartz confinement. For PIV, the calibration board is placed inside either the mixing or confinement quartz tubes and an image is captured for calibration. An image model fit (IMF) is created after selecting the calibration board type (i.e., checkerboard or dots) based on predefined calibration targets in DynamicStudio software. After selecting the IMF, image dewarping is processed using interpolation as a resampling scheme. It should be noted that aberration was considered negligible since the quartz tube wall thickness is 2.5 mm. For flame front positions, after detecting the flame front positions using an in-house developed Matlab code, the correction

is made by applying ray tracing based on Snell's law to obtain the actual positions. Hence, the positions are corrected according to their radial distance from the centerline (see Fig. A.3c).

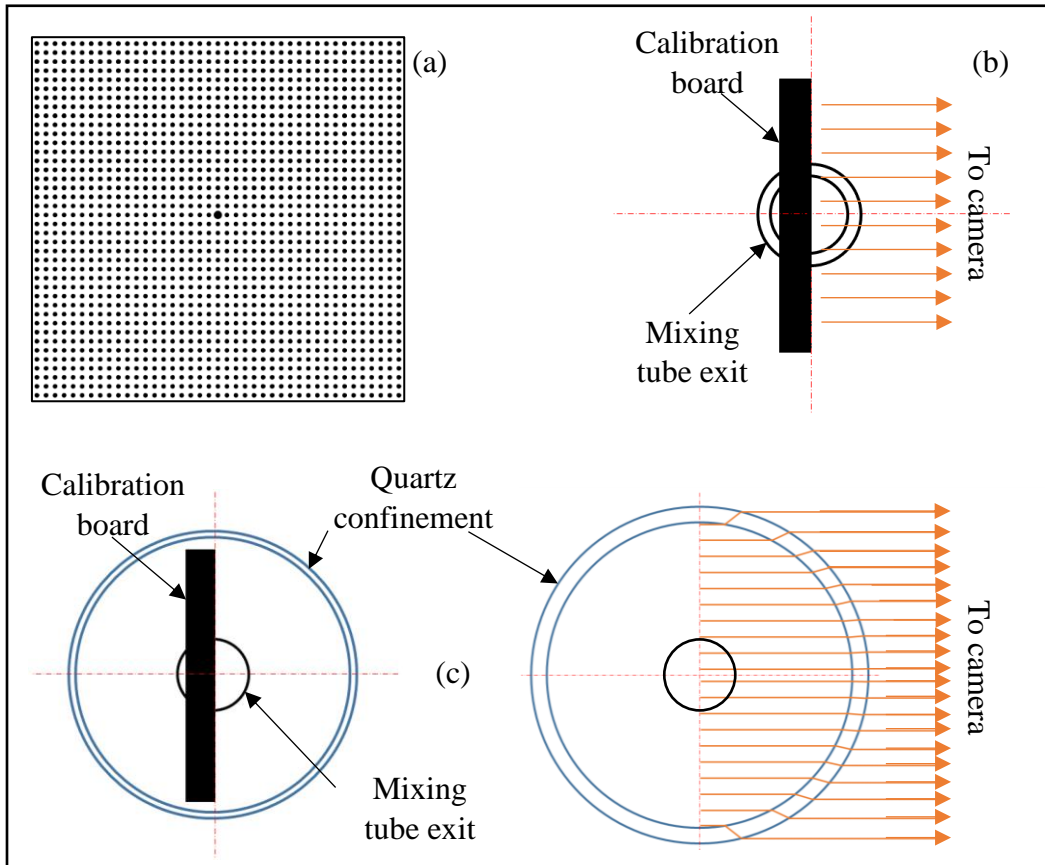


**Fig. A.3.** (a) Calibration board, and calibration procedure for both (b) unconfined and (c) confined flows.

## Appendix B: Laser Doppler Velocimetry (LDV)

LDV in the present study is used for single point measurements. The LDV system consists of Coherent Innova 70c-5 Ar-ion 5 W laser, Fiberlight FBL-3 multicolor beam separator, TSI TR 260 fiberoptic, TLN06-350 lens, TSI PDM 1000 photo detector module, and TSI FSA 4000 Doppler burst correlator. Figure B.1 depicts the LDV system. The laser head is directly connected to the multicolor beam separator to provide the different beam colors at different wavelengths ( $\lambda_w$ ) and deliver the shifted and unshifted beams to the TSI TR 260 fiberoptic through the optical fibers. The beam steering mirror and the dispersion prisms are responsible for dispersing the input laser beam into different beams with different wavelengths. A Bragg cell splits the beam of similar wavelength into shifted and unshifted beams by adding 40 MHz frequency to the shifted beam. The laser is aligned by adjusting the fine and course x-y adjustment knobs, and the focusing ring (see Fig. B.1a). The TSI TR 260 fiberoptic is equipped with TLN06-350 lens. The four laser beams are intersected at the focal length and form the focal volume (measurement volume). When two laser beams are intersected, a fringe pattern is obtained. As a result, the measurement volume contains a series of dark and bright fringes which move with a rate of 40 MHz. This series of fringes has a certain spacing between each successive dark or bright fringes called fringe spacing ( $d_f$ ). This fringe spacing is constant since it depends on the laser wavelength and the angle between the two beams with similar color ( $\kappa$ ). The fringe spacing is calculated as follows:

$$d_f = \frac{\lambda_w}{2\sin(\kappa/2)} \quad \text{B.1}$$

Incense and TiO<sub>2</sub> particles of a mean diameter of 1  $\mu\text{m}$  are used in isothermal and reactive flow cases, respectively. Once the seeding particles pass across the focal volume, the light scatters and the signal is obtained (see Fig. B.2). The scattered light signal is received in the backscatter mode arrangement through the TSI TR 260 fiberoptic. It should be noted that the



scattered intensity obtained by backscatter mode arrangement is less than that of the forward scatter mode arrangement. The signal is transmitted to the photo detector module (see Fig. B.3). The optical signal is converted to an electrical signal by photomultiplier tubes (PMT). The phase delay is corrected using a calibration diode equipped in the photo detector module. The photo detector module and the Doppler burst correlator are connected. The function of the Doppler burst correlator is to derive the phase and frequency of the signal. The seeding particle velocity is calculated by multiplying the fringe spacing by the derived signal frequency as follows:

$$V = f_D d_f$$

B.2

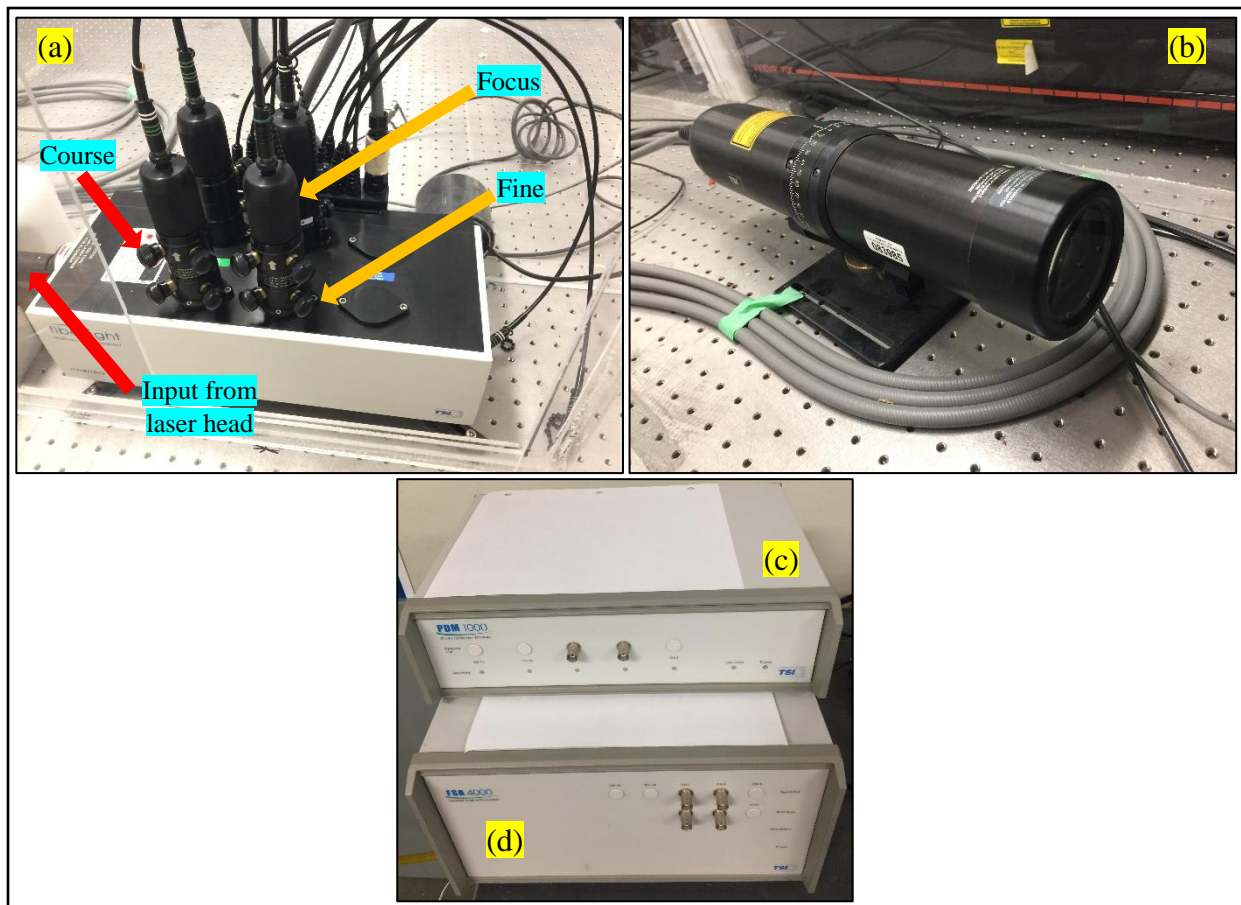


**Fig. B.1.** LDV system including (a) the multicolor beam separator, (b) probe, (c) PDM, and (d) Doppler burst correlator.

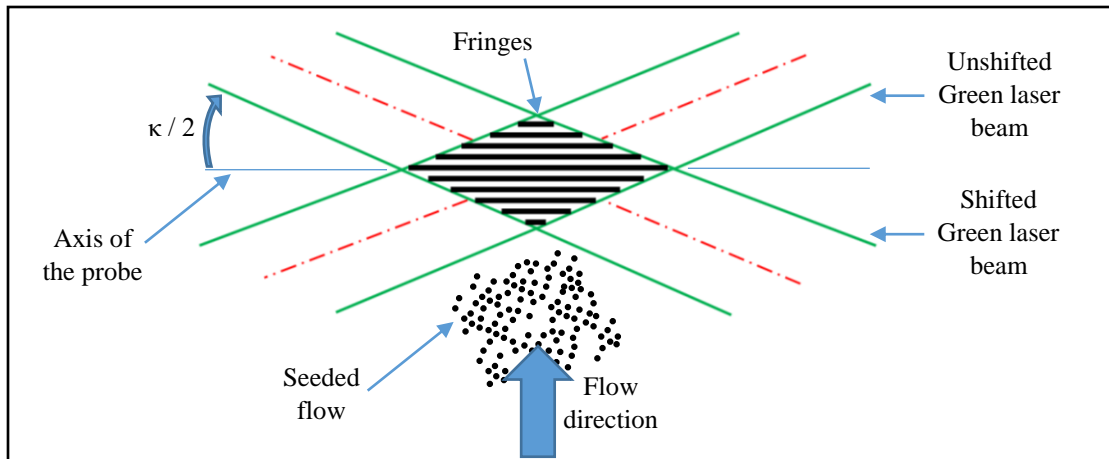


**Fig. B.2.** The measurement volume with the formed fringes.

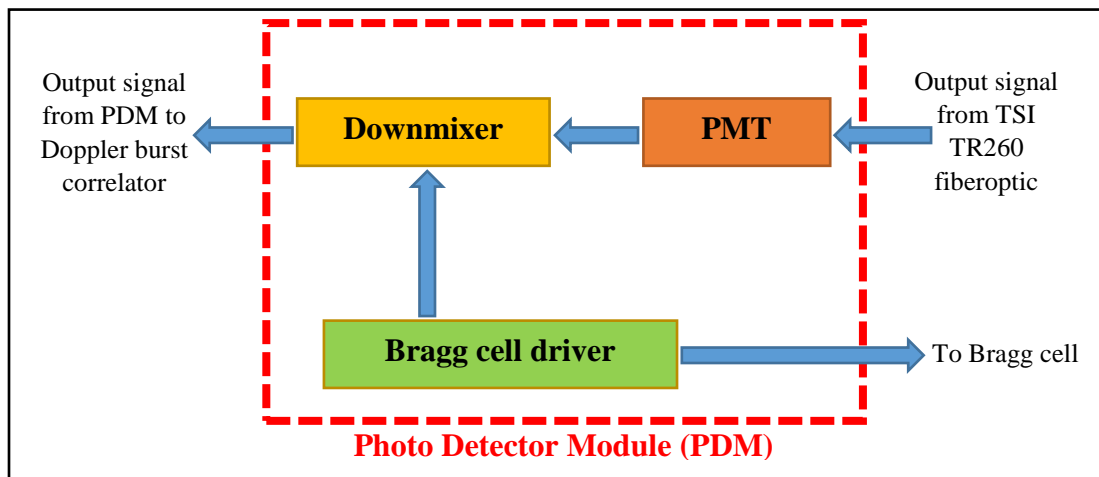


**Fig. B.3.** The photo detector module with the main components.

TSI FlowSizer software is used to operate and control the LDV system and acquire the data. As previously mentioned, four laser beams with two different wavelengths are emitted. That is, two blue laser beams with a wavelength of 488 nm are used to capture the radial velocity component while two green laser beams with a wavelength of 514.5 nm are used to capture the axial velocity component. Since only the axial velocity component is investigated, the blue laser beams are disabled by using the shutter and by unchecking the channel 2 checkbox in the software (see Fig.

B.4). More details on the optical parameters are shown in Fig. B.4. The calculated length and diameter of the focal volume are 1.25 mm and 90  $\mu\text{m}$ , respectively.

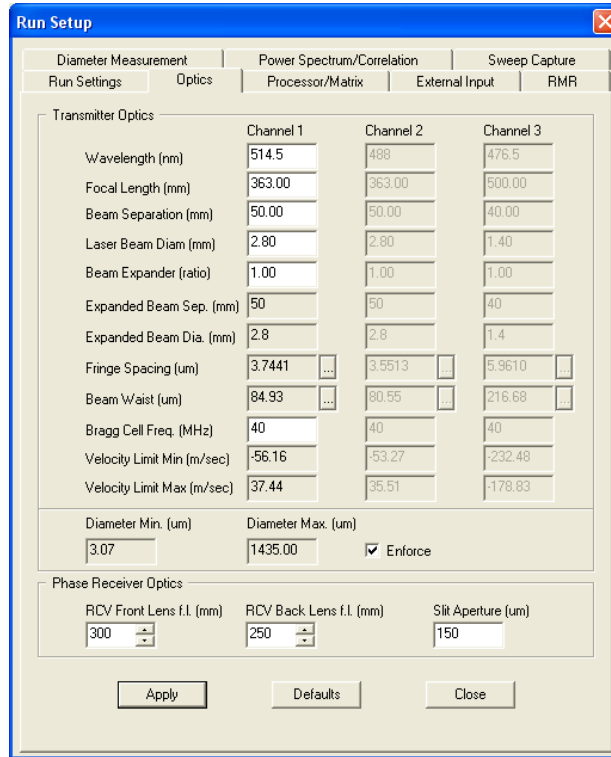


**Fig. B.4.** The optical parameters used in the present configuration

Once the electrical signal is obtained from the PMT, the signal is filtered by a high-pass filter to remove the pedestal resulting from the Gaussian distribution of the laser beam (see Fig. B.5). Due to that movement, the obtained signal frequency is the sum of the Doppler frequency plus 40 MHz. By selecting a certain downmix frequency value, this value is subtracted from the Bragg cell shift (40 MHz) and the resultant frequency is added to the Doppler frequency. In the present study, the selected downmix frequency is 20 MHz which allows flow reversal up to 20 MHz. This obtained signal is filtered again by a low-pass filter to remove the high frequency noise. More details on the processor control parameters are listed in Table B.1. The signal from seeding is significantly

altered using confinement and by the flame in the reactive cases. Accordingly, the resultant data rates vary from 2.4 to 12 kHz whereas the number of the collected samples varies from 150,000 to 500,000 depending on the test case. Furthermore, the employed laser power varies from 700 to 1000 mW depending on the test case. When measuring the confined flows, frequent cleaning of the quartz confinement is important to keep the SNR high during the measurements. The output data is exported to Matlab for further data filtering and equidistant resampling procedure.

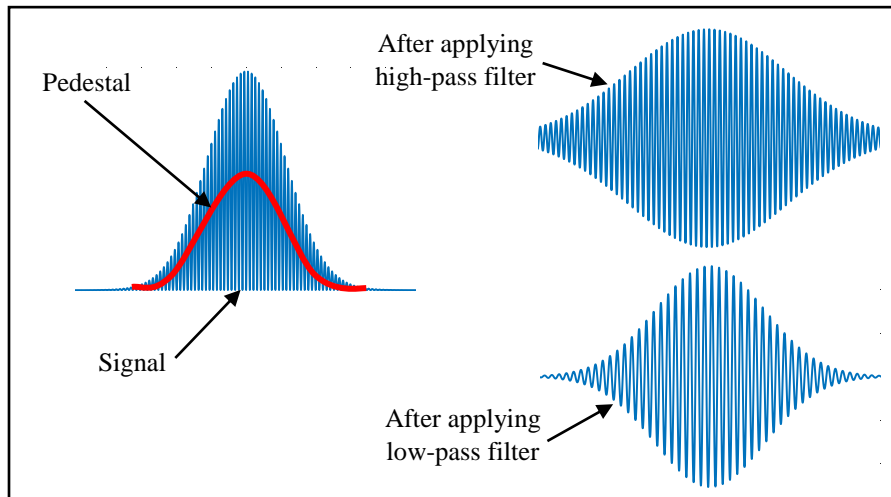


**Fig. B.5.** Typical LDV signal and filtering processes.

**Table B.1.** The selected parameters for the processor control.

<b>PMT voltage (mV)</b>	ranges from 470 to 520 depending on the test case
<b>Burst threshold (mV)</b>	ranges from 35 to 80 depending on the test case
<b>Band pass filter (MHz)</b>	5-30
<b>Downmix frequency (MHz)</b>	20

## Appendix C: Microphone Calibration

Microphone calibration is carried out using a Bruel & Kjaer 4230 sound level calibrator which is designed for calibrating Bruel & Kjaer 0.5-inch microphones (e.g., Bruel & Kjaer 4189). The accuracy of this calibrator is  $\pm 0.3$  dB at  $23^\circ\text{C} \pm 3^\circ\text{C}$ . The calibration is conducted at room temperature (i.e.,  $\sim 23^\circ\text{C}$ ). The effective coupler volume is larger than  $140\text{ cm}^3$  at  $23^\circ\text{C}$ . The calibration pressure is  $94 \pm 0.3$  dB while the calibration frequency is  $1000\text{ Hz} \pm 1.5\%$ . The calibrator consists of Zener stabilized oscillator, Helmholtz resonator, piezoelectric driver element, and metallic diaphragm (see Fig. C.1). The Zener oscillator generates a stabilized 1000 Hz signal that is sent to the piezoelectric driver element. The piezoelectric driver element is connected to the metallic diaphragm that vibrates accordingly to produce the sound pressure. The Helmholtz resonator is added to behind the metallic diaphragm. This results in an independent resonant frequency of ambient pressure, and makes the resonant frequency depends on the volume of the cavity only.

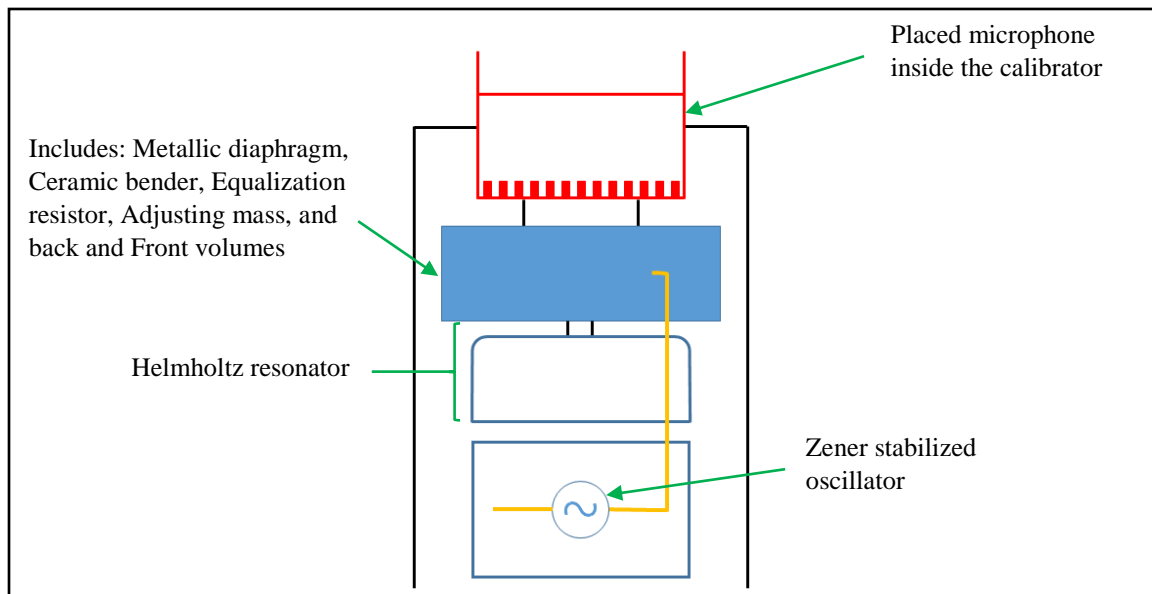


**Fig. C.1.** Schematic of the internal structure of the sound calibrator type 4230 [1].

It is strongly recommended that calibration is carried out before and after each measurement. The microphone is connected to Bruel & Kjaer sound level analyzer type 2260 Investigator. This sound level analyzer is operated by BZ7210 v2.2 software. The Bruel & Kjaer type 4189 microphone (labelled with A in Fig. C.2) is inserted precisely into Bruel & Kjaer 4230 sound level calibrator (labelled with B in Fig. C.2). Using the software, the calibration is made internally first, where the system undergoes internal calibration of its converters and the previous microphone sensitivity is shown. The calibration level is adjusted at 93.9 dB. Once the internal calibration is finished, the software requests to turn on the calibrator and, hence, the microphone is fit into the calibrator. The indicator in the software shows the correct sound pressure level and, finally, the deviation is indicated. The final deviation was -0.03 dB while the sensitivity -25.9 dB. This procedure is repeated after each experiment while the signal is collected and sent to a computer for further analysis.



**Fig. C.2.** Images of the microphone (first row) and the sound level calibrator (second row).

## References

[1]

[http://www.technicalaudio.com/pdf/Bruel&Kjaer/Bruel&Kjaer\\_Calibrator\\_Sound\\_Level\\_4230.pdf](http://www.technicalaudio.com/pdf/Bruel&Kjaer/Bruel&Kjaer_Calibrator_Sound_Level_4230.pdf)